

โครงสร้างและสมบัติของสารประกอบเพอโรฟสไกต์  $\text{Ln}(\text{Pr, La})_2(\text{Co, Ni, Cu})\text{O}_4$

ที่ถูกโคปด้วยไอออนของสทรอนเทียม



สถาบันวิทยบริการ  
จุฬาลงกรณ์มหาวิทยาลัย

วิทยานิพนธ์นี้เป็นส่วนหนึ่งของการศึกษาตามหลักสูตรปริญญาวิทยาศาสตรมหาบัณฑิต

สาขาวิชาปิโตรเคมีและวิทยาศาสตร์พอลิเมอร์

คณะวิทยาศาสตร์ จุฬาลงกรณ์มหาวิทยาลัย

ปีการศึกษา 2550

ลิขสิทธิ์ของจุฬาลงกรณ์มหาวิทยาลัย

STRUCTURES AND PROPERTIES OF STRONTIUM ION DOPED

$\text{Ln}(\text{Pr}, \text{La})_2(\text{Co}, \text{Ni}, \text{Cu})\text{O}_4$  PEROVSKITES



Miss Nuengruetai Supanwanich

สถาบันวิทยบริการ  
จุฬาลงกรณ์มหาวิทยาลัย

A Thesis Submitted in Partial Fulfillment of the Requirements  
for the Degree of Master of Science Program in Petrochemistry and Polymer Science

Faculty of Science

Chulalongkorn University


Academic Year 2007

Copyright of Chulalongkorn University


Thesis Title           STRUCTURES AND PROPERTIES OF STRONTIUM  
                                  ION DOPED  $\text{Ln}(\text{Pr}, \text{La})_2(\text{Co}, \text{Ni}, \text{Cu})\text{O}_4$  PEROVSKITES  
By                         Miss Nuengruetai Supanwanich  
Field of Study         Petrochemistry and Polymer Science  
Thesis Advisor       Assistant Professor Oravan Sanguanruang, Ph.D.

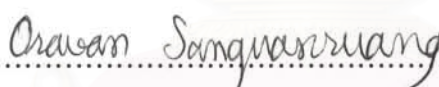
---

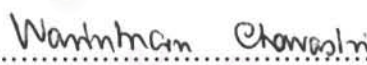
Accepted by the Faculty of Science, Chulalongkorn University in Partial  
Fulfillment of the Requirements for the Master's Degree


  
.....Dean of the Faculty of Science  
(Professor Supot Hannongbua, Ph. D.)

#### THESIS COMMITTEE

  
.....Chairman  
(Associate Professor Sirirat Kokpol, Ph.D.)

  
.....Thesis Advisor  
(Assistant Professor Oravan Sanguanruang, Ph.D.)

  
.....Member  
(Assistant Professor Warinthorn Chavasiri, Ph.D.)

  
.....Member  
(Parichatr Vanalabhpattana, Ph.D.)

หนึ่งฤทัย สุพันธ์วิช : โครงสร้างและสมบัติของสารประกอบเพอโรฟสไกต์  $\text{Ln}(\text{Pr}, \text{La})_2(\text{Co}, \text{Ni}, \text{Cu})\text{O}_4$  ที่ถูกโคปด้วยไอออนของสตรอนเทียม (STRUCTURES AND PROPERTIES OF STRONTIUM ION DOPED  $\text{Ln}(\text{Pr}, \text{La})_2(\text{Co}, \text{Ni}, \text{Cu})\text{O}_4$  PEROVSKITES) อ.ที่ปรึกษา : ผศ.ดร. อรวรรณ สงวนเรือง, 91 หน้า.

ทำการสังเคราะห์สารประกอบเพอโรฟสไกต์ออกไซด์  $\text{Ln}(\text{Pr}, \text{La})_{2-x}\text{Sr}_x\text{MO}_4$  ( $x = 0, 0.4, 0.6, 0.8, 1.0$ ) ( $M = \text{Co}, \text{Ni}, \text{Cu}$ ) ด้วยวิธีสังเคราะห์แบบของแข็ง เพื่อศึกษาถึงผลของการเติมสตรอนเทียมที่ตำแหน่ง A ที่มีต่อโครงสร้างและสมบัติ ตรวจสอบโครงสร้างผลึก และลักษณะของเพอโรฟสไกต์ที่เตรียมได้ด้วยเทคนิค XRD, FT-IR และ SEM ผลจากการตรวจสอบโครงสร้างพบว่า สารตัวอย่างทั้งหมดสามารถเตรียมได้ และให้โครงสร้างแบบ  $\text{K}_2\text{NiF}_4$  แต่  $\text{Ln}(\text{Pr}, \text{La})_{2-x}\text{Sr}_x\text{CoO}_4$  มีความไม่เสถียร เมื่อทำการเติม  $\text{Sr}^{2+}$  ซึ่งมีขนาดรัศมีไอออนใหญ่กว่า  $\text{Pr}^{3+}$  และ  $\text{La}^{3+}$  ลงไป โครงสร้างผลึกจะเปลี่ยนจากโครงสร้างแบบออร์โธโรมบิก ไปเป็นโครงสร้างแบบเตตระโกนัล นอกจากนี้การเติมสตรอนเทียมยังส่งผลให้จุดหลอมเหลวของสารประกอบลดลง ซึ่งทำให้เกรนมีขนาดใหญ่ขึ้นและมีความหนาแน่นเพิ่มขึ้น โดยคอปเปอร์ก็ส่งผลให้จุดหลอมเหลวของสารประกอบลดลงเช่นกัน ผลจากการตรวจสอบค่าการนำไฟฟ้า แสดงถึงการเติมสตรอนเทียมทำให้ค่าการนำไฟฟ้าเพิ่มขึ้น โดยค่าการนำไฟฟ้าของสารประกอบนิกเกิล จะให้ค่าที่มากกว่าของสารประกอบคอปเปอร์  $\text{PrSrNiO}_4$  ให้ค่าการนำไฟฟ้ามากที่สุด คือ 423.5 S/cm ที่อุณหภูมิ 300 °C ซึ่งมีค่ามากกว่า  $\text{Pr}_2\text{NiO}_4$  (107.4 S/cm ที่ 400 °C) ที่ไม่ได้ทำการเติมสตรอนเทียม 4 เท่า และ  $\text{LaSrNiO}_4$  ให้ค่าการนำไฟฟ้า 361.6 S/cm ที่อุณหภูมิ 400 °C ซึ่งให้ค่ามากกว่า  $\text{La}_2\text{NiO}_4$  (80.1 S/cm ที่ 400 °C) 4.5 เท่า ซึ่งค่าการนำไฟฟ้าและการดูดซับของออกซิเจนที่สูงกว่าของ  $\text{PrSrNiO}_4$  แสดงถึงความเหมาะสมในการนำไปใช้ในเซลล์เชื้อเพลิงของแข็ง

สถาบันวิทยบริการ  
จุฬาลงกรณ์มหาวิทยาลัย

สาขาวิชา ..... ปิโตรเคมีและวิทยาศาสตร์พอลิเมอร์ ..... ลายมือชื่อนิสิต ..... หนึ่งฤทัย สุพันธ์วิช  
ปีการศึกษา ..... 2550 ..... ลายมือชื่ออาจารย์ที่ปรึกษา ..... อรวรรณ สงวนเรือง

# # 4872530023: MAJOR PETROCHEMISTRY AND POLYMER SCIENCE

KEY WORD: PEROVSKITE /  $K_2NiF_4$  / SOFC

NUENGRUETAI SUPANWANICH: STRUCTURES AND PROPERTIES  
OF STRONTIUM ION DOPED  $Ln(Pr, La)_2(Co, Ni, Cu)O_4$  PEROVSKITES.  
THESIS ADVISOR: ASST. PROF. ORAVAN SANGUANRUANG, Ph.D.,  
91 pp.

The perovskite-like oxides  $Ln(Pr, La)_{2-x}Sr_xMO_4$  ( $M = Co, Ni, Cu$ ) ( $x = 0.4, 0.6, 0.8, 1$ ) were synthesized by the modified citrate method in order to study the influence of strontium doping at A-site on the structure and property. As the results, characterized by XRD supported by FT-IR and SEM, all specimens can be prepared and showed homogeneous  $K_2NiF_4$ -phase but  $Ln(Pr, La)_{2-x}Sr_xCoO_4$  series had physical instability. The substitution of  $Sr^{2+}$  (larger radius) for  $Pr^{3+}$  or  $La^{3+}$  (smaller radius), caused the transformation of structure from orthorhombic to tetragonal. Moreover, doping with strontium affected on the decreasing of melting points of the materials, resulting in enhanced grain growth according to the density. However, Cu also can affect the decreasing of the melting point of  $Ln(Pr, La)_{2-x}Sr_xCuO_4$ , so the fusion of grain of cuprates more easily occurred than that of nickelates. The electrical conductivity can be improved by addition Sr at A-site. The conductivities of the nickelate were higher than that of cuprate.  $PrSrNiO_4$  showed the highest electrical conductivity (423.5 S/cm at 300 °C) which was about 4 times higher than that of undoped  $Pr_2NiO_4$  (107.4 S/cm at 400 °C) and  $LaSrNiO_4$  showed the electrical conductivity of 361.6 S/cm at 400 °C which was about 4.5 times higher than that of  $La_2NiO_4$  (80.1 S/cm at 400 °C). The higher electrical conductivity of  $PrSrNiO_4$  combined with higher oxygen adsorption indicate that this material could be a good candidate for use in solid oxide fuel cell.

Field of study: Petrochemistry and Polymer science. Student's signature: Nuengruetai Supanwan  
Academic year: 2007. Advisor's signature: Oravan Sanguanruang

## ACKNOWLEDGEMENTS

The success of this thesis can be attributed to the extensive support and assistance from Assistant Professor Dr. Oravan Sanguanruang, my thesis advisor for her valuable advice and guidance in this research.

I would like to gratitude to Associate Professor Dr. Sirirat Kokpol, Assistant Professor Dr. Warinthorn Chavasiri, Associate Professor Wimonrat Trakarnpruk and Dr. Parichatr Vanalabhpattana as the chairman and member of this thesis committee, respectively, for all of their kindness and useful advice in the research.

I would like to gratefully thank Dr. Thanakorn Wasanapiarnpong in Department of Material Science, Faculty of Science, Chulalongkorn University for supporting instrument. Moreover I would like to thank Department of Chemistry and Program of Petrochemistry and Polymer Science, Faculty of Science, Chulalongkorn University for the valuable knowledge and experience. I would like to thank the Graduate School Chulalongkorn University for supporting a research fund. In addition, Thailand Japan Technology Transfer Project supported a loan by Japan Banks for International Cooperation (TJTTP-JBIC) for instrument support. Furthermore, I would like to thank the members of Materials Chemistry and Catalysis Research Unit for consideration and generosity.

For all of my friends, I greatly appreciate their help and encouragement throughout the course of my research and study.

Finally, I would also like to express my deepest gratitude to my family for their great support and enormous encouragement during the entire study.

สถาบันวิทยบริการ  
จุฬาลงกรณ์มหาวิทยาลัย

# CONTENTS

	<b>Page</b>
<b>ABSTRACT IN THAI</b> .....	iv
<b>ABSTRACT IN ENGLISH</b> .....	v
<b>ACKNOWLEDGEMENT</b> .....	vi
<b>CONTENETS</b> .....	vii
<b>LIST OF TABLES</b> .....	xi
<b>LIST OF FIGURES</b> .....	xii
<b>LIST OF ABBREVIATIONS</b> .....	xv
<b>CHAPTER I INTRODUCTION</b> .....	1
1.1 Fuel Cell .....	1
1.2 Solid Oxide Fuel Cell (SOFC) .....	2
1.2.1 Operating Concept of a SOFC .....	3
1.2.2 Materials Selection and Processing .....	5
1.2.2.1 Cathode .....	6
1.2.2.2 Electrolyte .....	7
1.2.2.3 Anode .....	8
1.2.2.4 Interconnect .....	9
1.3 Perovskite .....	9
1.3.1 Structure of Perovskites .....	11
1.3.2 Nonstoichiometry in Perovskites .....	15
1.3.3 Physical Properties of Perovskite Oxide .....	16
1.3.4 Oxygen Adsorption Property .....	18
1.3.5 Perovskite Synthesis .....	19
1.3.5.1 Gas Phase Reaction .....	20
1.3.5.2 Solid–State Reaction .....	20
1.3.5.3 Solution Reactions .....	20
1.3.6 Powder Sizing .....	23
1.3.7 Sintering .....	23
1.4 Literature Reviews .....	24
1.5 The Objectives of the Thesis .....	27

	<b>Page</b>
<b>CHAPTER II EXPERIMENTS</b> .....	28
2.1 Chemicals .....	28
2.2 Preparations of Perovskite Powders by Modified Citrate Method.....	29
2.3 Perovskite Disc Preparation.....	30
2.4 The Sintering of the Perovskite Oxides.....	31
2.5 Characterization Techniques.....	32
2.5.1 X-Ray Diffractometry (XRD) .....	32
2.5.2 Fourier Transform–Infrared Spectroscopy (FT–IR).....	32
2.5.3 Scanning Electron Microscopy (SEM).....	33
2.5.4 Density .....	33
2.5.5 Temperature–Programmed Desorption (TPD).....	33
2.5.6 Electrical Conductivity Measurement.....	34
 <b>CHAPTER III RESULTS AND DISSCUSSIONS</b> .....	 36
3.1 Synthesis of $\text{Ln}_{2-x}\text{Sr}_x\text{MO}_4$ Perovskite Powder by Modified Citrate Method.....	36
3.2 Tolerance Number of Perovskite Compounds.....	38
3.3 Characterization of the Perovskite Compounds .....	39
3.3.1 X-ray Diffraction (XRD) .....	39
3.3.1.1 Phase Formation of $\text{Pr}_{2-x}\text{Sr}_x\text{CoO}_4$ (x = 0, 0.4, 0.6, 0.8 and 1.0).....	40
3.3.1.2 Phase Formation of $\text{La}_{2-x}\text{Sr}_x\text{CoO}_4$ (x = 0, 0.4, 0.6, 0.8 and 1.0).....	41
3.3.1.3 Phase Formation of $\text{Pr}_{2-x}\text{Sr}_x\text{NiO}_4$ (x = 0, 0.4, 0.6, 0.8 and 1.0).....	42
3.3.1.4 Phase Formation of $\text{La}_{2-x}\text{Sr}_x\text{NiO}_4$ (x = 0, 0.4, 0.6, 0.8 and 1.0).....	43
3.3.1.5 Phase Formation of $\text{Pr}_{2-x}\text{Sr}_x\text{CuO}_4$ (x = 0, 0.4, 0.6, 0.8 and 1.0).....	44
3.3.1.6 Phase Formation of $\text{La}_{2-x}\text{Sr}_x\text{CuO}_4$ (x = 0, 0.4, 0.6, 0.8 and 1.0).....	45



	<b>Page</b>
3.3.2 Fourier Transform–Infrared Spectroscopy (FT–IR).....	49
3.3.2.1 Spectroscopic Behaviour of $\text{Pr}_{2-x}\text{Sr}_x\text{NiO}_4$ (x = 0, 0.4, 0.6, 0.8 and 1.0).....	49
3.3.2.2 Spectroscopic Behaviour of $\text{La}_{2-x}\text{Sr}_x\text{NiO}_4$ (x = 0, 0.4, 0.6, 0.8 and 1.0).....	50
3.3.2.3 Spectroscopic Behaviour of $\text{Pr}_{2-x}\text{Sr}_x\text{CuO}_4$ (x = 0, 0.4, 0.6, 0.8 and 1.0).....	50
3.3.2.4 Spectroscopic Behaviour of $\text{La}_{2-x}\text{Sr}_x\text{CuO}_4$ (x = 0, 0.4, 0.6, 0.8 and 1.0).....	51
3.3.3 Scanning Electron Microscopy (SEM).....	52
3.3.3.1 The Surface Morphology of $\text{Pr}_2\text{NiO}_4$ .....	52
3.3.3.2 The Surface Morphology of $\text{Pr}_{2-x}\text{Sr}_x\text{NiO}_4$ (x = 0.4, 0.6, 0.8 and 1.0).....	53
3.3.3.3 The Surface Morphology of $\text{La}_2\text{NiO}_4$ .....	54
3.3.3.4 The Surface Morphology of $\text{La}_{2-x}\text{Sr}_x\text{NiO}_4$ (x = 0.4, 0.6, 0.8 and 1.0).....	55
3.3.3.5 The Surface Morphology of $\text{Pr}_2\text{CuO}_4$ .....	56
3.3.3.6 The Surface Morphology of $\text{Pr}_{2-x}\text{Sr}_x\text{CuO}_4$ (x = 0.4, 0.6, 0.8 and 1.0).....	57
3.3.3.7 The Surface Morphology of $\text{La}_2\text{CuO}_4$ .....	58
3.3.3.8 The Surface Morphology of $\text{La}_{2-x}\text{Sr}_x\text{CuO}_4$ (x = 0.4, 0.6, 0.8 and 1.0).....	59
3.3.4 Temperature–Program Desorption of Oxygen ( $\text{O}_2$ –TPD) ..	60
3.3.4.1 The Oxygen Desorption of $\text{Pr}_{2-x}\text{Sr}_x\text{NiO}_4$ (x = 0.4, 0.6, 0.8 and 1.0).....	61
3.3.4.2 The Oxygen Desorption of $\text{La}_{2-x}\text{Sr}_x\text{NiO}_4$ (x = 0.4, 0.6, 0.8 and 1.0).....	63
3.3.4.3 The Oxygen Desorption of $\text{Pr}_{2-x}\text{Sr}_x\text{CuO}_4$ (x = 0.4, 0.6, 0.8 and 1.0).....	64
3.3.4.4 The Oxygen Desorption of $\text{La}_{2-x}\text{Sr}_x\text{CuO}_4$ (x = 0.4, 0.6, 0.8 and 1.0).....	65
3.3.5 Electrical Conductivity Measurement.....	66

	<b>Page</b>
3.3.5.1 The Electrical Conductivity of $\text{Pr}_{2-x}\text{Sr}_x\text{NiO}_4$ ( $x = 0.4, 0.6, 0.8$ and $1.0$ ).....	67
3.3.5.2 The Electrical Conductivity of $\text{La}_{2-x}\text{Sr}_x\text{NiO}_4$ ( $x = 0.4, 0.6, 0.8$ and $1.0$ ).....	69
3.3.5.3 The Electrical Conductivity of $\text{Pr}_{2-x}\text{Sr}_x\text{CuO}_4$ ( $x = 0.4, 0.6, 0.8$ and $1.0$ ).....	71
3.3.5.4 The Electrical Conductivity of $\text{Pr}_{2-x}\text{Sr}_x\text{CuO}_4$ ( $x = 0.4, 0.6, 0.8$ and $1.0$ ).....	74
<b>CHAPTER IV CONCLUSION</b> .....	77
<b>REFERENCES</b> .....	79
<b>APPENDICES</b> .....	85
<b>VITAE</b> .....	91

สถาบันวิทยบริการ  
จุฬาลงกรณ์มหาวิทยาลัย

## LIST OF TABLES

<b>Table</b>	<b>Page</b>
<b>1.1</b> Types of fuel cells.....	2
<b>2.1</b> Chemical and reagents for synthesis of perovskite.....	28
<b>2.2</b> Composition and abbreviation of $\text{Ln}_{2-x}\text{Sr}_x\text{MO}_4$ .....	29
<b>3.1</b> List of the features of the $\text{Ln}(\text{Pr}, \text{La})_{2-x}\text{Sr}_x\text{MO}_4$ ( $\text{M} = \text{Co}, \text{Ni}, \text{Cu}$ ) ( $x = 0, 0.4, 0.6, 0.8, 1.0$ ) perovskite compounds during preparation.....	37
<b>3.2</b> The tolerance numbers of all the prepared perovskites.....	38
<b>3.3</b> Summary of the XRD analysis of prepared membrane samples.....	47
<b>3.4</b> Grain Sizes and Densities of $\text{Pr}_{2-x}\text{Sr}_x\text{NiO}_4$ ( $x = 0, 0.4, 0.6, 0.8$ and $1.0$ ) Membranes.....	54
<b>3.5</b> Grain Sizes and Densities of $\text{La}_{2-x}\text{Sr}_x\text{NiO}_4$ ( $x = 0, 0.4, 0.6, 0.8$ and $1.0$ ) Membranes.....	56
<b>3.6</b> Grain Sizes and Densities of $\text{Pr}_{2-x}\text{Sr}_x\text{CuO}_4$ ( $x = 0, 0.4, 0.6, 0.8$ and $1.0$ ) Membranes.....	58
<b>3.7</b> Grain Sizes and Densities of $\text{La}_{2-x}\text{Sr}_x\text{CuO}_4$ ( $x = 0, 0.4, 0.6, 0.8$ and $1.0$ ) Membranes.....	60
<b>3.8</b> Amount of oxygen desorbed for $\text{Pr}_{2-x}\text{Sr}_x\text{NiO}_4$ ( $x = 0, 0.4, 0.6, 0.8, 1.0$ ).....	62
<b>3.9</b> Amount of oxygen desorbed for $\text{La}_{2-x}\text{Sr}_x\text{NiO}_4$ ( $x = 0, 0.4, 0.6, 0.8, 1.0$ ).....	64
<b>3.10</b> Amount of oxygen desorbed for $\text{Pr}_{2-x}\text{Sr}_x\text{CuO}_4$ ( $x = 0, 0.4, 0.6, 0.8, 1.0$ ).....	65
<b>3.11</b> Amount of oxygen desorbed for $\text{La}_{2-x}\text{Sr}_x\text{CuO}_4$ ( $x = 0, 0.4, 0.6, 0.8, 1.0$ ).....	66
<b>3.12</b> The specific conductivity of $\text{Pr}_{2-x}\text{Sr}_x\text{NiO}_4$ ( $x = 0, 0.4, 0.6, 0.8$ and $1.0$ ).....	67
<b>3.13</b> Activation energy of $\text{Pr}_{2-x}\text{Sr}_x\text{NiO}_4$ ( $x = 0, 0.4, 0.6, 0.8$ and $1.0$ ).....	69
<b>3.14</b> The specific conductivity of $\text{La}_{2-x}\text{Sr}_x\text{NiO}_4$ ( $x = 0, 0.4, 0.6, 0.8$ and $1.0$ ).....	70
<b>3.15</b> Activation energy of $\text{La}_{2-x}\text{Sr}_x\text{NiO}_4$ ( $x = 0, 0.4, 0.6, 0.8$ and $1.0$ ).....	71
<b>3.16</b> The specific conductivity of $\text{Pr}_{2-x}\text{Sr}_x\text{CuO}_4$ ( $x = 0, 0.4, 0.6, 0.8$ and $1.0$ ).....	72
<b>3.17</b> Activation energy of $\text{Pr}_{2-x}\text{Sr}_x\text{CuO}_4$ ( $x = 0, 0.4, 0.6, 0.8$ and $1.0$ ).....	73
<b>3.18</b> The specific conductivity of $\text{La}_{2-x}\text{Sr}_x\text{CuO}_4$ ( $x = 0, 0.4, 0.6, 0.8$ and $1.0$ ).....	75
<b>3.19</b> Activation energy of $\text{La}_{2-x}\text{Sr}_x\text{CuO}_4$ ( $x = 0, 0.4, 0.6, 0.8$ and $1.0$ ).....	76

## LIST OF FIGURES

<b>Figure</b>	<b>Page</b>
1.1 Scheme of operating concept of a SOFC.....	3
1.2 Configuration for a planar design SOFC.....	4
1.3 Configuration for a tubular design SOFC.....	4
1.4 (a) An ideal cubic perovskite and (b) A distorted perovskite with orthorhombic symmetry.....	11
1.5 ABO <sub>3</sub> ideal perovskite structure showing oxygen octahedron containing the B ion linked through corners to form a three-dimensional cubic lattice.....	12
1.6 Crystal structure of K <sub>2</sub> NiF <sub>4</sub> -type oxide.....	13
1.7 Crystal structure of A <sub>2</sub> BO <sub>4</sub> compounds with different phases (T', T and T*); (○) Oxygen; (●) B-site cations; (⊗) A-site cations.....	14
1.8 The relationship between symmetry and ionic radii in the perovskite.....	15
1.9 Mechanism of sintering.....	24
2.1 The calcination condition of perovskite oxide powder.....	30
2.2 The sintering conditions of Ln(La, Pr) <sub>2-x</sub> Sr <sub>x</sub> MO <sub>4</sub> (a) M = Co (b) M = Ni and (c) M = Cu.....	32
2.3 DC four-probe method.....	34
3.1 The XRD patterns of Pr <sub>2-x</sub> Sr <sub>x</sub> CoO <sub>4</sub> (x = 0, 0.4, 0.6, 0.8 and 1.0) after sintered at 1300°C for 6 hours.....	40
3.2 The XRD patterns of La <sub>2-x</sub> Sr <sub>x</sub> CoO <sub>4</sub> (x = 0, 0.4, 0.6, 0.8 and 1.0) after sintered at 1300°C for 6 hours.....	41
3.3 The XRD patterns of Pr <sub>2-x</sub> Sr <sub>x</sub> NiO <sub>4</sub> (x = 0, 0.4, 0.6, 0.8 and 1.0) after sintered at 1400°C for 6 hours.....	42
3.4 The XRD patterns of La <sub>2-x</sub> Sr <sub>x</sub> NiO <sub>4</sub> (x = 0, 0.4, 0.6, 0.8 and 1.0) after sintered at 1400°C for 6 hours.....	43
3.5 The XRD patterns of Pr <sub>2-x</sub> Sr <sub>x</sub> CuO <sub>4</sub> (x = 0, 0.4, 0.6, 0.8 and 1.0) after sintered at 1150°C for 6 hours.....	44
3.6 The XRD patterns of La <sub>2-x</sub> Sr <sub>x</sub> CuO <sub>4</sub> (x = 0, 0.4, 0.6, 0.8 and 1.0) after sintered at 1150°C for 6 hours.....	45

<b>Figure</b>	<b>Page</b>
<b>3.7</b> Partial XRD patterns of perovskite membranes (a) $\text{Pr}_{2-x}\text{Sr}_x\text{CoO}_4$ , (b) $\text{La}_{2-x}\text{Sr}_x\text{CoO}_4$ , (c) $\text{Pr}_{2-x}\text{Sr}_x\text{NiO}_4$ , (d) $\text{La}_{2-x}\text{Sr}_x\text{NiO}_4$ , (e) $\text{Pr}_{2-x}\text{Sr}_x\text{CuO}_4$ and (f) $\text{La}_{2-x}\text{Sr}_x\text{CuO}_4$ with various Sr contents.....	46
<b>3.8</b> The examples of prepared instability perovskite membranes after sintered for 3 days.....	48
<b>3.9</b> FT–IR spectra of $\text{Pr}_{2-x}\text{Sr}_x\text{NiO}_4$ ( $x = 0, 0.4, 0.6, 0.8$ and $1.0$ ).....	49
<b>3.10</b> FT–IR spectra of $\text{La}_{2-x}\text{Sr}_x\text{NiO}_4$ ( $x = 0, 0.4, 0.6, 0.8$ and $1.0$ ).....	50
<b>3.11</b> FT–IR spectra of $\text{Pr}_{2-x}\text{Sr}_x\text{CuO}_4$ ( $x = 0, 0.4, 0.6, 0.8$ and $1.0$ ).....	50
<b>3.12</b> FT–IR spectra of $\text{Pr}_{2-x}\text{Sr}_x\text{CuO}_4$ ( $x = 0, 0.4, 0.6, 0.8$ and $1.0$ ).....	51
<b>3.13</b> SEM picture of the $\text{Pr}_2\text{NiO}_4$ membrane sintered at $1400^\circ\text{C}$ for 6 hours.....	52
<b>3.14</b> SEM pictures of the $\text{Pr}_{2-x}\text{Sr}_x\text{NiO}_4$ ( $x = 0.4, 0.6, 0.8$ and $1.0$ ) membrane sintered at $1400^\circ\text{C}$ for 6 hours.....	53
<b>3.15</b> SEM picture of the $\text{La}_2\text{NiO}_4$ membrane sintered at $1400^\circ\text{C}$ for 6 hours.....	54
<b>3.16</b> SEM pictures of the $\text{La}_{2-x}\text{Sr}_x\text{NiO}_4$ ( $x = 0.4, 0.6, 0.8$ and $1.0$ ) membrane sintered at $1400^\circ\text{C}$ for 6 hours.....	55
<b>3.17</b> SEM picture of the $\text{Pr}_2\text{CuO}_4$ membrane sintered at $1150^\circ\text{C}$ for 6 hours.....	56
<b>3.18</b> SEM pictures of the $\text{Pr}_{2-x}\text{Sr}_x\text{CuO}_4$ ( $x = 0.4, 0.6, 0.8$ and $1.0$ ) membrane sintered at $1150^\circ\text{C}$ for 6 hours.....	57
<b>3.19</b> SEM picture of the $\text{La}_2\text{CuO}_4$ membrane sintered at $1150^\circ\text{C}$ for 6 hours.....	58
<b>3.20</b> SEM pictures of the $\text{La}_{2-x}\text{Sr}_x\text{CuO}_4$ ( $x = 0.4, 0.6, 0.8$ and $1.0$ ) membrane sintered at $1150^\circ\text{C}$ for 6 hours.....	59
<b>3.21</b> $\text{O}_2$ –TPD profiles of the $\text{Pr}_{2-x}\text{Sr}_x\text{NiO}_4$ ( $x = 0, 0.4, 0.6, 0.8$ and $1.0$ ).....	61
<b>3.22</b> $\text{O}_2$ –TPD profiles of the $\text{La}_{2-x}\text{Sr}_x\text{NiO}_4$ ( $x = 0, 0.4, 0.6, 0.8$ and $1.0$ ).....	63
<b>3.23</b> $\text{O}_2$ –TPD profiles of the $\text{Pr}_{2-x}\text{Sr}_x\text{CuO}_4$ ( $x = 0, 0.4, 0.6, 0.8$ and $1.0$ ).....	64
<b>3.24</b> $\text{O}_2$ –TPD profiles of the $\text{La}_{2-x}\text{Sr}_x\text{CuO}_4$ ( $x = 0, 0.4, 0.6, 0.8$ and $1.0$ ).....	65
<b>3.25</b> Electrical conductivity ( $\sigma$ ) of $\text{Pr}_{2-x}\text{Sr}_x\text{NiO}_4$ ( $x = 0, 0.4, 0.6, 0.8$ and $1.0$ ) as a function of measuring temperature.....	67
<b>3.26</b> Arrhenius plots of $\text{Pr}_{2-x}\text{Sr}_x\text{NiO}_4$ ( $x = 0, 0.4, 0.6, 0.8$ and $1.0$ ).....	68
<b>3.27</b> Electrical conductivity ( $\sigma$ ) of $\text{La}_{2-x}\text{Sr}_x\text{NiO}_4$ ( $x = 0, 0.4, 0.6, 0.8$ and $1.0$ ) as a function of measuring temperature.....	69
<b>3.28</b> Arrhenius plots of $\text{La}_{2-x}\text{Sr}_x\text{NiO}_4$ ( $x = 0, 0.4, 0.6, 0.8$ and $1.0$ ).....	70

<b>Figure</b>	<b>Page</b>
<b>3.29</b> Electrical conductivity ( $\sigma$ ) of $\text{Pr}_{2-x}\text{Sr}_x\text{CuO}_4$ ( $x = 0, 0.4, 0.6, 0.8$ and $1.0$ ) as a function of measuring temperature.....	71
<b>3.30</b> Arrhenius plots of $\text{La}_{2-x}\text{Sr}_x\text{NiO}_4$ ( $x = 0, 0.4, 0.6, 0.8$ and $1.0$ ).....	73
<b>3.31</b> Electrical conductivity ( $\sigma$ ) of $\text{La}_{2-x}\text{Sr}_x\text{CuO}_4$ ( $x = 0, 0.4, 0.6, 0.8$ and $1.0$ ) as a function of measuring temperature.....	74
<b>3.32</b> Arrhenius plots of $\text{La}_{2-x}\text{Sr}_x\text{CuO}_4$ ( $x = 0, 0.4, 0.6, 0.8$ and $1.0$ ).....	75



สถาบันวิทยบริการ  
จุฬาลงกรณ์มหาวิทยาลัย

## LIST OF ABBREVIATIONS

PSN 1604	$\text{Pr}_{1.6}\text{Sr}_{0.4}\text{NiO}_4$
PSN 1406	$\text{Pr}_{1.4}\text{Sr}_{0.6}\text{NiO}_4$
PSN 1208	$\text{Pr}_{1.2}\text{Sr}_{0.8}\text{NiO}_4$
PSN 1010	$\text{PrSrNiO}_4$
LSN 1604	$\text{La}_{1.6}\text{Sr}_{0.4}\text{CuO}_4$
LSN 1406	$\text{La}_{1.4}\text{Sr}_{0.6}\text{CuO}_4$
LSN 1208	$\text{La}_{1.2}\text{Sr}_{0.8}\text{CuO}_4$
LSN 1010	$\text{LaSrCuO}_4$
PSCu 1604	$\text{Pr}_{1.6}\text{Sr}_{0.4}\text{CuO}_4$
PSCu 1406	$\text{Pr}_{1.4}\text{Sr}_{0.6}\text{CuO}_4$
PSCu 1208	$\text{Pr}_{1.2}\text{Sr}_{0.8}\text{CuO}_4$
PSCu 1010	$\text{PrSrCuO}_4$
LSCu 1604	$\text{La}_{1.6}\text{Sr}_{0.4}\text{CuO}_4$
LSCu 1406	$\text{La}_{1.4}\text{Sr}_{0.6}\text{CuO}_4$
LSCu 1208	$\text{La}_{1.2}\text{Sr}_{0.8}\text{CuO}_4$
LSCu 1010	$\text{LaSrCuO}_4$
SOFCs	Solid oxide fuel cells
HC	Hydrocarbon
YSZ	Yttrium stabilized zirconia
MIEC	Mixed ionic–electronic conducting
XRD	X-ray diffractometer
SEM	Scanning electron microscopy
TPD	Temperature–programmed desorption
$\delta, \lambda$	Oxygen non–stoichiometry
Å	Angstrom
O	Orthorhombic
T	Tetragonal
t	Tolerance factor
r	Ionic radius
°C	Degree Celsius
K	Absolute temperature

$\sigma$	Specific conductivity
R	Electrical resistance
$\rho$	Specific resistance
L	Length
A	Area
I	Electrical current



สถาบันวิทยบริการ  
จุฬาลงกรณ์มหาวิทยาลัย



# CHAPTER I

## INTRODUCTION

Petroleum, the worlds most fuel, is becoming more scarce and its burning produces emissions of air pollution. Contributions also come from deforestation, carbon dioxide from the burning of coal, and methane release. In order to reverse the trend of destroying the environment, a change to a more ecologically resource or method of producing energy such as hydrodynamic, wind, geothermal and solar is desirable. These methods are presently employed in a somewhat small scale, but require specific environments in order to work effectively. Fuel cell need no particular environment to work well and is highly efficient both electrically and physically.

### 1.1 Fuel Cell

A fuel cell is an electrochemical device that converts the chemical energy in fuels (such as hydrogen, methane, butane or even gasoline and diesel) into electrical energy by exploiting the natural tendency of oxygen and hydrogen to react. Fuel cells are simple devices, containing no moving parts and only four functional component elements: cathode, electrolyte, anode and interconnect. Fuel cells can be divided into five major categories named after the electrolyte used in each; alkaline, solid polymer, phosphoric acid, molten carbonate and solid oxide as shown in Table 1.1. The five types resulted from the knowledge that heat accelerates chemical reaction rates and thus the electrical current. The materials used for electrolytes have their best conductance only within certain temperature ranges and thus other materials must be used in order to take advantage of the temperature increase.

**Table 1.1** Types of fuel cells

Type	Alkaline fuel cell (AFC)	Proton Exchange Membrane fuel cell (PEMFC)	Phosphoric Acid fuel cell (PAFC)	Molten Carbonate fuel cell (MCFC)	Solid Oxide fuel cell (SOFC)
Electrolyte	Alkaline solution	Polymer	Phosphoric acid	Molten Carbonate	Oxide
Charge Carrier	$\text{OH}^-$	$\text{H}^+$	$\text{H}^+$	$\text{CO}_3^-$	$\text{O}^{2-}$
Operating Temp. ( $^{\circ}\text{C}$ )	<100	80–100	150–200	600–700	<1000
Fuel	$\text{H}_2$	$\text{H}_2$	$\text{H}_2$	$\text{H}_2$ , CO	Hydrocarbon, $\text{H}_2$ , CO
Efficiency (%)	30	30–40	40	45–60	<b>50–60</b>
Application	Mobile Space Ship	Mobile Vehicle	Stationary	Stationary	Stationary Mobile

Solid oxide fuel cells (SOFCs) are now being considered for large power plants and for industrial applications because of its electrolytic resistance to poisoning which allows internal reforming of many carbon compounds into hydrogen to create power.

## 1.2 Solid Oxide Fuel Cell (SOFC)

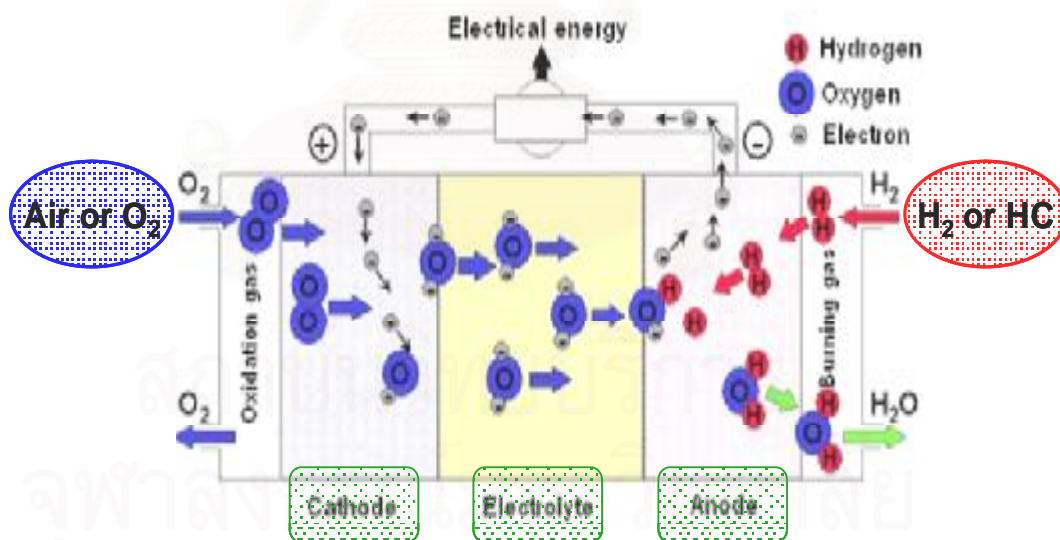
Solid oxide fuel cell (SOFC) is an electrochemical conversion device that produces electricity directly from fuel. Fuel cells are characterized by their electrolyte material and, as the name implies, the SOFC has a solid oxide, or ceramic, electrolyte.

The primary drawback to this type of fuel cell is the cost of the containment which requires exotic ceramics which must have similar expansion rates. SOFC are now being considered for large power plants and for industrial applications because of its electrolytic resistance to poisoning which allows internal reforming

of many carbon compounds into hydrogen to create power. This means that SOFC do not get poisoned by carbon monoxide and this makes them highly fuel-flexible.

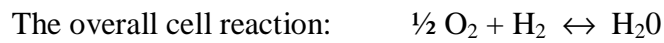
### 1.2.1 Operating Concept of a SOFC

Figure 1.1 shows schematically operation of SOFC. The cell is constructed with two porous electrodes which sandwich an electrolyte. Air flows along the cathode (which is therefore also called the “air electrode”). When an oxygen molecule contacts the cathode/electrolyte interface, it catalytically acquires electrons from the cathode. The oxygen ions diffuse into the electrolyte material and migrate to the other side of the cell where they encounter the anode (also called the “fuel electrode”). The oxygen ions encounter the fuel at the anode/electrolyte interface and react catalytically, giving off water, carbon dioxide, heat, and most importantly electrons. The electrons transport through the anode to the external circuit and back to the cathode, providing a source of useful electrical energy in an external circuit [1].



**Figure 1.1** Scheme of operating concept of a SOFC

The electrochemical reactions occurring within the cell are:



Two possible design configurations for SOFCs have emerged: a planar design (Figure 1.2) and a tubular design (Figure 1.3). In the planar design, the components are assembled in flat stacks, with air and fuel flowing through channels built into the cathode and anode. In the tubular design, components are assembled in the form of a hollow tube, with the cell constructed in layers around a tubular cathode; air flows through the inside of the tube and fuel flows around the exterior [2].

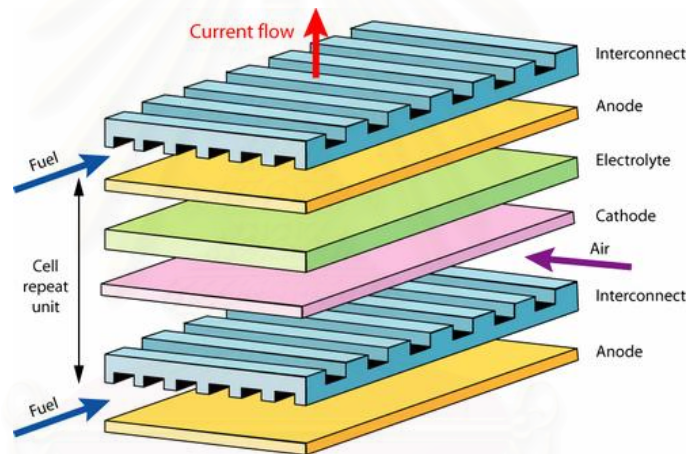


**Figure 1.2** Configuration for a planar design SOFC

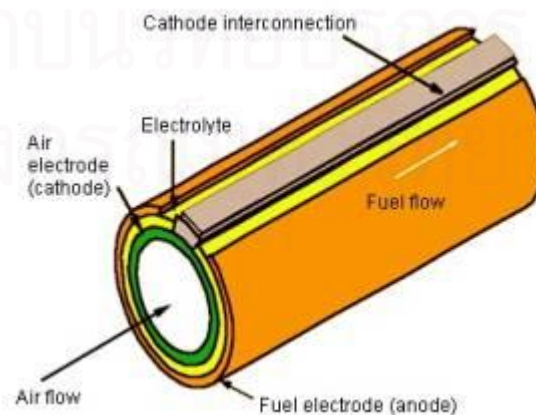


**Figure 1.3** Configuration for a tubular design SOFC

SOFCs which operate at the high temperature (750–1100 °C) are not the most reactive because of the low conductivity of its ionic conducting electrolyte. Many advances have been made in SOFCs research to increase the chemical to electrical efficiency to 50%, but because of the conductivity and the heat, it has been used mainly in large power plants which can use the cogeneration of steam for additional power. Because of the high temperature, the cell requires no expensive catalysts, or additional humidification and fuel treatment equipment which exclude the cost of these items. The primary drawback to this type of fuel cell is the cost of the containment which requires exotic ceramics which must have similar expansion rates [3]. SOFCs use a ceramic electrolyte that results in a solid state unit, an important aspect. The conduction mechanism is solid state conduction of oxygen ions ( $O^{2-}$ ). The reaction is completed by the reaction of oxygen ions and hydrogen to form water. As indicated by their name, SOFCs use solid oxide ceramics, typically perovskites, as the electrolyte. Nernst realized in the 1890s that certain perovskites, stabilized zirconias, conducted ions in a certain temperature range. Currently, yttrium stabilized zirconias (YSZ) is the most commonly used electrolyte for SOFC. YSZ provides high conductivity at temperatures above 700 °C, while exhibiting negligible electronic conductivity at these temperatures. The composition of the electrode, particle sizes of the powders and the manufacturing method are key to achieve high electrical conductivity, adequate ionic conductivity, and high activity for electrochemical reactions.

### **1.2.2 Materials Selection and Processing**

Although the operating concept of SOFCs is rather simple, the selection of materials for the individual components presents enormous challenges. Each material must have the electrical properties required to perform its function in the cell. There must be enough chemical and structural stability to endure fabrication and operation at high temperatures. The fuel cell needs to run at high temperatures in order to achieve sufficiently high current densities and power output; operation at up to 1000 °C is possible using the most common electrolyte material, yttria-stabilized zirconia (YSZ). Reactivity and interdiffusion between the components must be as low as possible. The thermal expansion coefficients of the components

must be as close to one another as possible in order to minimize thermal stresses which could lead to cracking and mechanical failure. The air side of the cell (cathode) must operate in an oxidizing atmosphere and the fuel side (anode) must operate in a reducing atmosphere. The temperature and atmosphere requirements drive the materials selection for all the other components.

In order for SOFCs to reach their commercial potential, the materials and processing must also be cost-effective. The first successful SOFC used platinum as both the cathode and anode, but fortunately less expensive alternatives are available today [4].

SOFCs is made up of four layers, consisting cathode, electrolyte, anode and interconnect, three of which are ceramics. A single cell consisting of these four layers stacked together is typically only a few millimeters thick. Hundreds of these cells are then connected in series to form what most people refer to as an “SOFC stack”. The ceramics used in SOFCs do not become electrically and ionically active until they reach very high temperature and as a consequence the stacks have to run at temperatures ranging from 700 to 1,200 °C.

### 1.2.2.1 Cathode

The cathode must meet all the above requirements and be porous in order to allow oxygen molecules to reach the electrode/electrolyte interface. In some designs (e.g. tubular) the cathode contributes over 90% of the cell's weight and therefore provides structural support for the cell [5].

Today the most commonly used cathode material is lanthanum manganite ( $\text{LaMnO}_3$ ), a p-type perovskite. Typically, it is doped with rare earth elements (eg. Sr, Ce, Pr) to enhance its conductivity. Most often it is doped with strontium and referred to as LSM ( $\text{La}_{1-x}\text{Sr}_x\text{MnO}_3$ ). The conductivity of these perovskites is all electronic (no ionic conductivity), a desirable feature since the electrons from the open circuit flow back through the cell *via* the cathode to reduce the oxygen molecules, forcing the oxygen ions through the electrolyte. In addition to being compatible with YSZ electrolytes, it has the further advantage of having adequate functionality at intermediate fuel cell temperatures (about 700 °C), allowing it to be used with alternative electrolyte compositions. Any reduction in operating

temperature reduces operating costs and expands the materials selection, creating an opportunity for additional cost savings.

### 1.2.2.2 Electrolyte

Once the molecular oxygen has been converted to oxygen ions it must migrate through the electrolyte to the anode. In order for such migration to occur, the electrolyte must possess a high ionic conductivity and no electrical conductivity. It must be fully dense to prevent short circuiting of reacting gases through it and it should also be as thin as possible to minimize resistive losses in the cell. As with the other materials, it must be chemically, thermally, and structurally stable across a wide temperature range.

There are several candidate materials: YSZ, doped cerium oxide, and doped bismuth oxide. Of these, the first two are the most promising. Bismuth oxide-based materials have a high oxygen ion conductivity and lower operating temperature (less than 800 °C), but do not offer enough crystalline stability at high temperature to be broadly useful. YSZ has emerged as the most suitable electrolyte material. Yttria serves the dual purpose of stabilizing zirconia into the cubic structure at high temperatures and also providing oxygen vacancies at the rate of one vacancy per mole of dopant. A typical dopant level is 10 mol% yttria [6].

A thin, dense film of electrolyte (approximately 40 microns thick) needs to be applied to the cathode substrate. A reliable way to apply the electrolyte is known as electrochemical vapor deposition which offers high purity and a high level of process control. Alternative electrolyte deposition methods that show promise are spray coating and dip coating followed by sintering. Colloidal suspensions of YSZ are applied in thin layers of at least 20 microns, using nanosize (5–10 nm) particles in order to meet the critical requirement of low porosity. Through careful engineering of the particle size distribution and dispersions, these deposition methods are likely to replace electrochemical deposition [7].

### 1.2.2.3 Anode

The anode must meet most of the same requirements as the cathode for electrical conductivity, thermal expansion compatibility and porosity, and must function in a reducing atmosphere. The reducing conditions combined with electrical conductivity requirements make metals attractive candidate materials.

Most development has focused on nickel owing to its abundance and affordability. However, its thermal expansion ( $13.3 \times 10^{-6}/^{\circ}\text{C}$  compared with  $10 \times 10^{-6}/^{\circ}\text{C}$  for YSZ) is too high to pair it in pure form with YSZ; moreover, it tends to sinter and close off its porosity at operation temperatures. These problems have been solved by making the anode out of a Ni–YSZ composite. The YSZ provides structural support for separated Ni particles, preventing them from sintering together while matching the thermal expansions. Adhesion of the anode to the electrolyte is also improved [6].

Anodes are applied to the fuel cell through powder technology processes. Either a slurry of Ni is applied over the cell and then YSZ is deposited by electrochemical vapor deposition, or a Ni–YSZ slurry is applied and sintered. More recently NiO–YSZ slurries have been used, the NiO being reduced to particulate Ni in the firing process. In order to maintain porosity, pore formers such as starch, carbon, or thermosetting resins are added. These burn out during firing and leave pores behind.

Other choices of material are under investigation as well. Although Ni–YSZ is currently the anode material of choice and the freeze–drying process solves most of the associated problems, nickel still has a disadvantage: it catalyzes the formation of graphite from hydrocarbons. The deposition of graphite residues on the interior surfaces of the anode reduces its usefulness by destroying one of the main advantages of SOFCs, namely their ability to use unreformed fuel sources.

Cu–cerium oxide anodes are being studied as a possible alternative. Copper is an excellent electrical conductor but a poor catalyst of hydrocarbons; cerium oxide is used as the matrix in part because of its high activity of hydrocarbon oxidation. A composite of the two thus has the advantage of being compatible with cerium oxide electrolyte fuel cells. Initial results using a wide range of hydrocarbon fuels are promising [8].



#### 1.2.2.4 Interconnect

Just as an internal combustion engine relies on several cylinders to provide enough power to be useful, so fuel cells must be used in combination in order to generate enough voltage and current. This means that the cells need to be connected together and a mechanism for collection of electrical current needs to be provided, hence the need for interconnects. The interconnect functions as the electrical contact to the cathode while protecting it from the reducing atmosphere of the anode.

The high operating temperature of the cells combined with the severe environments means that interconnects must meet the most stringent requirements of all the cell components: 100% electrical conductivity, no porosity (to avoid mixing of fuel and oxygen), thermal expansion compatibility, and inertness with respect to the other fuel cell components. It will be exposed simultaneously to the reducing environment of the anode and the oxidizing atmosphere of the cathode.

For a YSZ SOFC operating at about 1000 °C, the material of choice is LaCrO<sub>3</sub> doped with a rare earth element (Ca, Mg, Sr, etc.) to improve its conductivity. Ca-doped yttrium chromite is also being considered because it has better thermal expansion compatibility, especially in reducing atmospheres [9]. Interconnects are applied to the anode by plasma spraying and then the entire cell is co-fired. Any reduction in component costs (either raw materials or processing) directly translates into improved energy affordability. The strong economic incentive to use traditional metals for the interconnect is driving the development of intermediate and low temperature SOFCs. At operating temperatures in the 900–1000 °C range, interconnects made of such nickel base alloys as Inconel 600 are possible [10]. At or below 800 °C, ferritic steels can be used. At even lower temperatures (below 700 °C), it becomes possible to use stainless steels, which are comparatively inexpensive and readily available [11].

### 1.3 Perovskite

Mixed ionic–electronic conducting (MIEC) perovskites exhibiting both electronic and ionic conductivities have drawn considerable research interest

because of their potential in various technological applications, such as oxygen separation membranes, membrane reactors for syngas production, catalysts for oxidation of hydrocarbons and intermediate temperature (600–800 °C) SOFC [12–15]. With the increase in global energy consumption, however, it is MIECs used as electrodes in SOFC that are attracting greatest attention from the scientific community. The main area of study is the development of new materials that would allow the operation of SOFC below 700 °C. This would have several benefits including an increase in the thermodynamic efficiency, longer device operating life and reduction in production costs. Some perovskite oxides ( $ABO_3$ ) are found to be good mixed-conducting materials. In the past decade, much work on the cathode materials for intermediate temperature SOFCs focused on oxygen-deficient perovskite-type oxides such as  $La_{1-x}Sr_xFe_{1-y}Co_yO_{3-\delta}$  (LSFC). However, the LSFC materials suffer from excessively high thermal expansion coefficients, making it difficult in matching with other components of intermediate temperature SOFCs. Recently, oxygen hyperstoichiometric  $La_2NiO_{4+\delta}$  based compounds ( $A_2BO_{4+\delta}$ ) with a  $K_2NiF_4$  structure have attracted growing attention as a novel mixed conductor [16–19]. These materials exhibit high oxygen diffusion and surface exchange coefficients at intermediate temperatures together with moderate thermal expansion coefficients around  $13.0 \times 10^{-6} \text{ K}^{-1}$  [20–22]. These desired properties make them promising candidate materials as cathodes for intermediate temperature SOFC. For the recent anode materials, most developers today use a cermet of nickel, and cathode materials are lanthanum based perovskite materials.

Perovskites are a large family of crystalline ceramics that derive their name from a specific mineral known as perovskite. They are the most abundant minerals on earth and have been of continuing interest to geologists for the clues they hold to the planet's history. The parent material, perovskite, was first described in the 1830's by the geologist Gustav Rose, who named it after the famous Russian mineralogist Count Lev Aleksevich von Perovski [23]. They are immensely used as electrode materials for SOFC, gas separation membranes, catalysts for oxidations of hydrocarbons and humidity sensors. This study is focused on the use of mixed conducting perovskites as SOFC materials.

### 1.3.1 Structure of Perovskites

The mineral perovskite typically exhibits a crystal lattice that appears cubic, though it is actually orthorhombic in symmetry due to a slight distortion of the structures are presented in Figure 1.4.

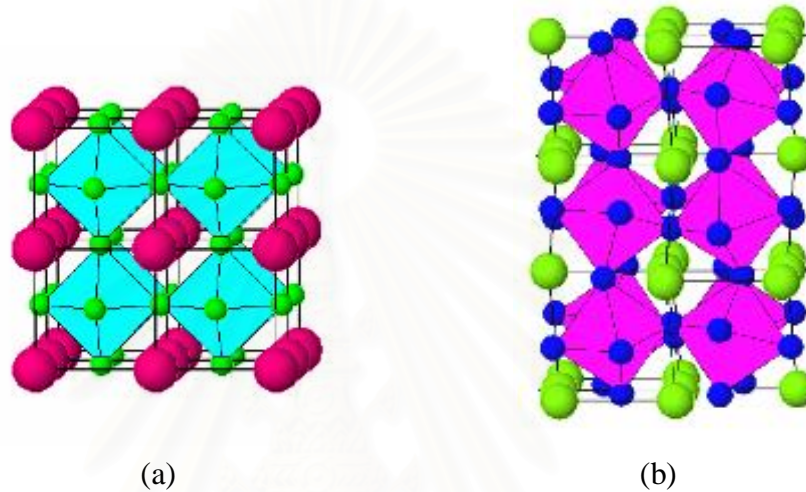


**Figure 1.4** (a) An ideal cubic perovskite and (b) A distorted perovskite with orthorhombic symmetry.

The characteristic chemical formula of a perovskite ceramic is  $ABO_3$ , where A is the larger twelve coordinated cation (rare earth or alkaline earth metal) and B is the smaller six coordinated cation (transition metal). The oxidation number of the A cation ranges from +1 to +3, and the oxidation number of the B cation from +3 to +6. Whereas the ideal structure is cubic, the actual structure is often disturbed. Alternatively, this structure can be viewed with the B cation placed in the center of the octahedron, the A cation is in the center of the cube and O ion is featured on the faces of that cube, as shown in Figure 1.5.

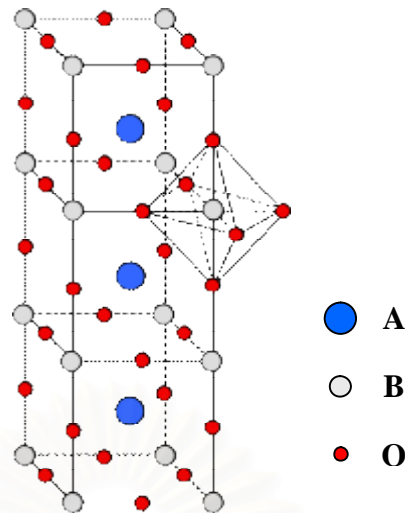


**Figure 1.5**  $ABO_3$  ideal perovskite structure showing oxygen octahedron containing the B ion linked through corners to form a three-dimensional cubic lattice.

Recently, Rare-earth transition-metal mixed oxides crystallizing with the perovskite and  $K_2NiF_4$ -type structures have received attention in recent years in view of the discovery of important physical properties such as high temperature superconductivity and colossal magnetoresistance. Both of these structures can be regarded as end members of a large family of so-called Ruddlesden-Popper phases (RP phases),  $(AO)(ABO_3)_n$ . In this formulation, the perovskites and the  $K_2NiF_4$ -type oxides correspond to  $n = \infty$  and  $n = 1$ , respectively. Unlike in the perovskite structure, where the corner-sharing  $BO_6$  octahedra form an infinite three dimensional (3D) network, in the  $K_2NiF_4$ -type structure as shown in Figure 1.6, the  $BO_6$  octahedra share corners in two dimensions (2D) and are sandwiched between the rock-salt-like AO layers, in which the B ions are in a usually distorted octahedral environment while the A cations are 9-coordinated. The electronic correlations of the  $BO_6$  network, therefore, are restricted to 2D, leading to interesting physical properties [24].

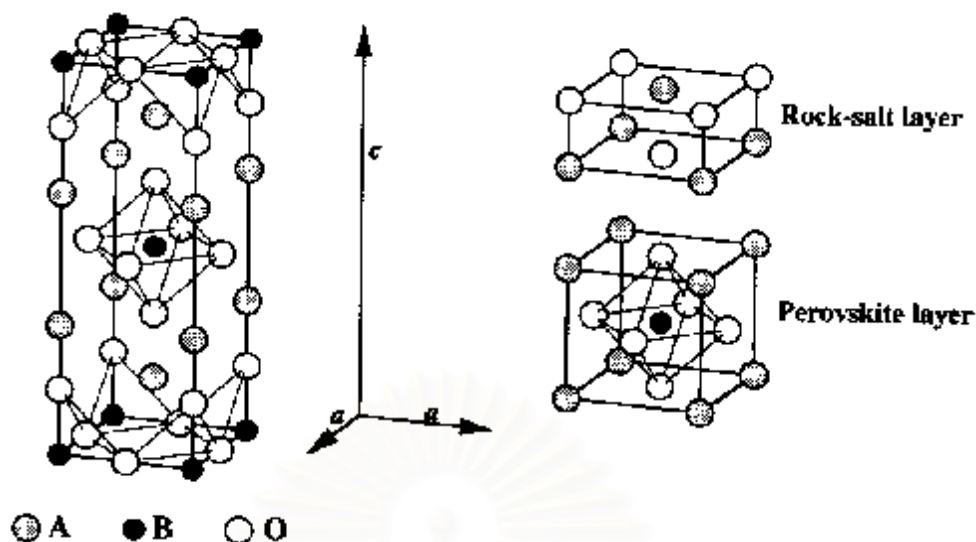


**Figure 1.6** Crystal structure of  $K_2NiF_4$ -type oxide.

While the RP phases of some transition metals, such as copper, nickel and manganese, have been thoroughly studied, there are series of other elements, such as those of cobalt, that have been relatively much less investigated, and that could also show interesting properties.

Compounds with formula  $A_2BO_4$  generally have the tetragonal  $K_2NiF_4$  structure when the radius of the A cation is  $1.0 < r_A < 1.9 \text{ \AA}$ , the radius of the B cation is  $0.5 < r_B < 1.2 \text{ \AA}$ . The larger A cation has nine-fold coordination and the smaller B cation has octahedral coordination. This structure can be described as containing alternate layering of perovskite ( $ABO_3$ ) and rock-salt (AO) units with the nine coordinate A cation having a surrounding that is the average of what it would be in perovskite and rock salt. Naturally, these perovskite-like compounds have three existent forms, described as T' (with B–O square), T (with B–O octahedral) and T\* (with B–O pyramids) phase, as shown in Figure 1.7, depending on the coordination number of oxygen for B cation. Different phase exhibits different properties [25].

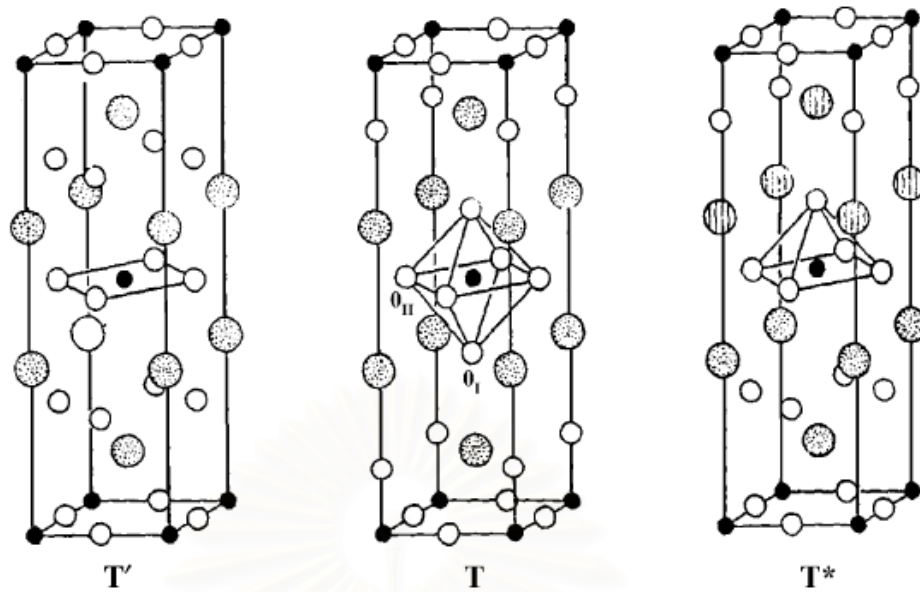


**Figure 1.7** Crystal structure of  $A_2BO_4$  compounds with different phases ( $T'$ ,  $T$  and  $T^*$ ). ( $\circ$ ) Oxygen; ( $\bullet$ ) B-site cations; ( $\odot$ ) A-site cations.

In the ideal structure, where the atoms are touching one another, the B–O distance is equal to  $a/2$  ( $a$  is the cubic unit cell parameter) while the A–O distance is  $(a/\sqrt{2})$  and the following relationship between the ionic radii holds:  $r_A + r_O = \sqrt{2}(r_B + r_O)$ . However, it was found that the cubic structure was still retained in  $ABO_3$  compounds, even though this equation is not exactly obeyed. As a measure of the deviation from the ideal situation, Goldschmidt introduced a tolerance factor ( $t$ ), defined by the equation:

$$t = \frac{(r_A + r_O)}{\sqrt{2}(r_B + r_O)} \quad (1.1)$$

Where  $r_A$  and  $r_B$  are the mean ionic radii for A and B site cation taking into account the coordination numbers, respectively, and  $r_O$  is the radii of oxide ion. This can be illustrated for the perovskite structure by deriving a relationship between the radii of the various ions. Figure 1.8 shows the relationship between ionic radii in the perovskite structure.

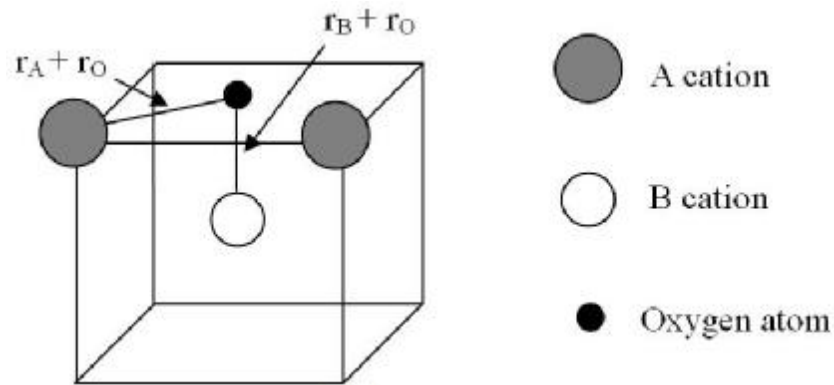


**Figure 1.8** The relationship between symmetry and ionic radii in the perovskite.

An ideal matching between the A cation and one layer of linked  $\text{BO}_6$  octahedra occurs for  $t \approx 1$  and the structure formed is tetragonal described in the space group  $I4/mmm$ . Even in the range of  $t = 0.8\text{--}0.9$  which is the most favourable value for perovskites. The distorted structure may show orthorhombic, rhombohedral, tetragonal, monoclinic and triclinic symmetry at room temperature but it transforms to the cubic structure at ambient temperature. Ganguly and Rao [26] proposed that  $\text{A}_2\text{BO}_4$  compounds with the  $t$ -value near the lower limit  $t \approx 0.85$  exhibit superlattice reflection lines in their diffraction patterns associated with a rotation of  $\text{BO}_6$  octahedra around the  $c$ -axis or a tilting of  $\text{BO}_6$  octahedra in the  $1\ 0\ 0$  or  $1\ 1\ 0$  direction [27].

### 1.3.2 Nonstoichiometry in Perovskites

Besides the ionic radii requirements, another condition to be fulfilled is electroneutrality, i.e., the sum of charges of A and B equals the total charge of oxygen anions. This is attained by means of appropriate charge distribution of the form  $\text{A}^{1+}\text{B}^{5+}\text{O}_3$ ,  $\text{A}^{2+}\text{B}^{4+}\text{O}_3$ , or  $\text{A}^{3+}\text{B}^{3+}\text{O}_3$ . In addition to this, partial substitution of A and B ions is allowed, thus yielding a plethora of compounds while preserving the perovskite structure. However, deficiencies of cations at the A- or B-sites or of oxygen anions are frequent, which results in defective perovskites.

Nonstoichiometry in perovskites can arise from cation deficiency (in the A or B site), anion deficiency, or anion excess. For the cation deficiency, A-site cations can be missing without collapse of the perovskite network because of the stability of the  $\text{BO}_3$  group [28]. On the contrary, B-site vacancies are not energetically favored because of the large formal charge and the small size of the B cations in perovskites. Nevertheless, an oxygen vacancy in perovskites is more common than a cation deficiency.

Many oxygen-deficient perovskites can be described on the basis of complex perovskite-related super-structures of general formula  $\text{A}_n\text{B}_n\text{O}_{3n-1}$ , in which the stacking manner depends on the size, electronic configurations, and coordination numbers of A and B cations. Oxygen vacancies are accomplished by substituting ions of similar size but different valence. For example, some of the  $\text{La}^{3+}$  ions in  $\text{La}_2\text{BO}_4$  are replaced by  $\text{Sr}^{2+}$  to form  $\text{La}_{2-x}\text{Sr}_x\text{BO}_{4-\delta}$ , and therefore, oxygen vacancies are formed in the structure.

### 1.3.3 Physical Properties of Perovskite Oxide

The perovskite structure class is one of the most commonly occurring and important in all of materials science. Physical properties of interest among perovskites include superconductivity, colossal magnetoresistance, ionic conductivity, and a multitude of dielectric properties, which are of great importance in microelectronics and telecommunication. Because of the great flexibility inherent in the perovskite structure there are many different types of distortions which can occur from the ideal structure. These include tilting of the octahedra, displacements of the cations out of the centers of their coordination polyhedra, and distortions of the octahedra driven by electronic factors (i.e. Jahn-Teller distortions). Many of the physical properties of perovskites depend crucially on the details of these distortions, particularly the electronic, magnetic and dielectric properties which are so important for many of the applications of perovskite materials.

In the ideal cubic perovskite structure, each atom of oxygen is shared by two  $\text{B}^{3+}$  ions, forming a B–O–B angle of  $180^\circ$ . Such a configuration is favorable for super exchange interactions between magnetic  $\text{B}^{3+}$  cations. This exchange usually results in anti-parallel coupling of nearest-neighbor magnetic moments.



When the  $B^{3+}$  ions are in two sub lattices ( $A_2BB'O_6$ ) the other spin arrangements are possible. If  $B'$  is a diamagnetic ion, the  $B^{3+}$  ions are aligned anti-ferromagnetic, and the most important exchange mechanism is believed to be a longer range super exchange interaction through two oxygens of the type  $B-O-B'-O-B$ . The  $B-B$  separation is now considerably longer than the 0.4 nm separation found in the ideal perovskite. The  $LnFeO_3$  ( $Ln =$  lanthanide) perovskites are those that have attracted the most attention because of their possible applications as technological magnetic materials [29]. These compounds show a weak spontaneous magnetic moment, which is attributed to a slight canting of the iron moments, which are otherwise anti-ferromagnetic aligned. Similarly,  $LnMnO_3$  shows very interesting magnetic properties. These manganites containing mostly  $Mn^{3+}$  or  $Mn^{4+}$  ions show anti-ferromagnetic behavior.

Perovskite oxide exhibits both ionic and electronic conductivity. It may show both high oxygen ion conductivity due to the high oxygen vacancy concentration, and a high electronic conductivity due to the mixed-valence state. [30], the  $B$  ions can take a mixed-valence state, charge neutrality is maintained by both the formations of oxygen vacancies and a change in the valence state of the  $B$  ions. The  $B$ -site ion substitution can increase the concentration of oxygen vacancies, such as  $Cu$  and  $Ni$  ions, which naturally take the divalent oxidation state [31]. If the valence state of the  $B$  ions is fixed, neutrality is maintained only by the formation of oxygen vacancies. The oxides may be predominantly ionic conductors, in this case.

In all materials that there are in principle nonzero electronic and ionic conductivity, the overall electrical conductivity  $\sigma_{tot}$  is the sum of electronic conductivity  $\sigma_e$  and ionic conductivity  $\sigma_i$ , as Equation (1.2),

$$\sigma_{tot} = \sum \sigma_{ij} + \sigma_e \quad (1.2)$$

where  $\sigma_{ij}$  is the partial conductivity (in  $\Omega^{-1}cm^{-1}$ ) of the  $j$ th-type ionic charge carriers presenting in the solid. Ionic charge carriers can be either atomic in nature or normally defects of either the anionic or cationic sublattice. Ionic conductivity occurs normally *via* interstitial sites or by hopping into a vacant site (vacancy motion) or a more complex combination based on interstitial and vacant sites.

Electronic (electron/hole) conductivity occurs *via* delocalized states in the conduction–valence band or *via* localized states by athermally assisted hopping mechanism. The presence of electronic conduction in perovskites proceeds *via* B.

Lattice cations through overlapping B–O–B bonds *via* a mechanism known as the Zerner double exchange process is shown in Equation (1.3) [32]:



This process is facilitated by strong overlap of the B site cation and  $O^{2-}$  orbital which is maximized for B–O–B angles at  $180^\circ$  as cubic structure. In the orthorhombic structure, the tilting of  $BO_6$  give rise to a decrease in the B–O–B overlap and thus would be expected to provide a larger barrier to electronic conduction. In the above double exchange mechanism, electronic conduction requires the presence of B site cations with multiple valences. Furthermore, the electronic conduction can be n–type or p–type, depending on the material properties and ambient oxygen partial pressure. The energy level shifts from the center of the energy gap toward the empty zone for an n–type semiconductor or the filled band for a p–type semiconductor. An n–type conductor is an electron conductor while a p–type conductor is an electron hole conductor. It was noticed that perovskites with high p–type electronic conductivity tended to be active for deep methane oxidation reactions while those with high n–type electronic conductivity, ionic conductors, and insulators were all found to be more selective to  $C_2$  compounds [33].

For characterization of the perovskite materials, it is more often to measure their electronic and ionic conductivity instead of concentrations of electrons (holes) and mobile ions (vacancy). The calculated ionic and electronic conductivity, which were separately measured by using 4–probe ionic direct current and ordinary 4–probe direct current techniques, respectively.

### 1.3.4 Oxygen Adsorption Property

Oxygen desorption properties from perovskite oxides have been studied as a function of the nature and concentration of dopant atoms introduced into both the

A- and B-sites. Previous work examining oxygen desorption using TPD from perovskite oxides has shown that two types of oxygen can become desorbed [34]. Oxygen desorbed at lower temperatures, termed  $\alpha$  oxygen, corresponds to adsorbed surface oxygen, and that desorbed at higher temperatures, designated  $\beta$  oxygen, is desorbed from lattice sites within the perovskite.

Yamazoe et al. [35] reported the oxygen TPD results from  $\text{La}_{1-x}\text{Sr}_x\text{CoO}_3$  perovskites. They concluded that the amount of desorbed oxygen from  $\text{La}_{1-x}\text{Sr}_x\text{CoO}_3$  increased with increasing  $x$ -substitution. Since A-site substitution with a divalent ion is known to induce the formation of oxygen vacancies.

In 2005, Junjiang Zhu, et al. [36] studied the  $\text{La}_{2-x}\text{Sr}_x\text{CuO}_4$  ( $x = 0.0, 0.5, 1.0$ ) catalysts for NO+CO reaction. In  $\text{O}_2$ -TPD experiment, the desorption area of  $\beta$  oxygen, which was contributed by the oxygen adsorbed on the oxygen vacancy, increased with the increase of Sr content and was in the same order as the activity. It is indicated that the activity depended largely on the oxygen vacancy resulted by Sr addition.

### 1.3.5 Perovskite Synthesis

Preparation of perovskite type membranes consists of three consecutive steps: powder synthesis, shaping and sintering. Firstly, powder synthesis which plays an important role in determining the particle size of the powder, and consequently has an influence on the microstructure of the membrane. There are several methods to synthesize powders, such as a conventional solid-state reaction method and a wet chemical process including thermal decomposition of cyanide, metal-EDTA, chemical co-precipitation and the sol-gel process. Cui and Liu [37] stated that powders synthesized by different methods caused different temperatures of crystal transformation. However, the formation of the crystal structure can be improved by a supercritical method to dry the surface defect of powders.

The synthesis of perovskite powder has been achieved by many methods, including a conventional solid-state reaction method and a solution reaction that includes thermal decomposition of cyanide, metal-EDTA, chemical co-precipitation and the sol-gel process etc.

### 1.3.5.1 Gas Phase Reaction

The deposition of perovskite films with a specific thickness and composition generally requires gas phase reaction or transport. Many physical techniques have been developed for gas phase deposition such as laser ablation, molecular beam epitaxy, dc sputtering, magnetron sputtering, electron beam evaporation and thermal evaporation. In general, they can be divided into two categories based on the target they use. The first type uses separate targets where a different speed of deposition for each element has to be determined. The second method uses the performed perovskite material itself as target and the stoichiometric phase is transported to the substrate by sputtering or ablation techniques.

### 1.3.5.2 Solid-State Reaction

The solid state reaction is very convenient but the impurities are introduced from raw materials, milling media, and the calcination container. Because the high temperature is required for the complete reaction. Conventional processing of the perovskite-related materials uses solid-state reactions between metal-carbonates, hydroxides, and oxides. LSCF represents a typical case. Raw materials  $\text{La}_2\text{O}_3$ ,  $\text{SrCO}_3$ ,  $\text{CoO}_3$ , and  $\text{Fe}_2\text{O}_3$  were mixed and ball-milled. After drying, then the mixed powders were calcined at  $1,000^\circ\text{C}$  to remove impurities and to achieve single-phase perovskite powder.

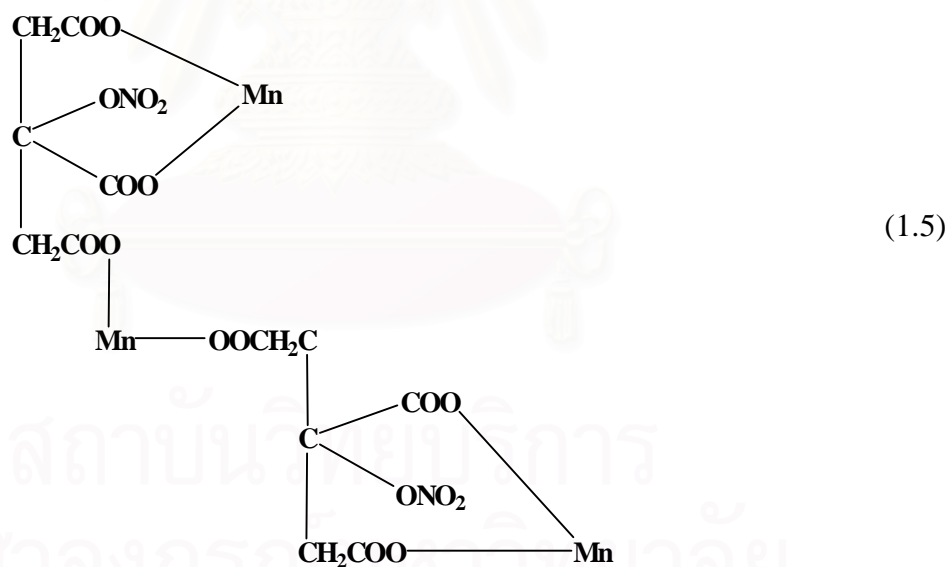
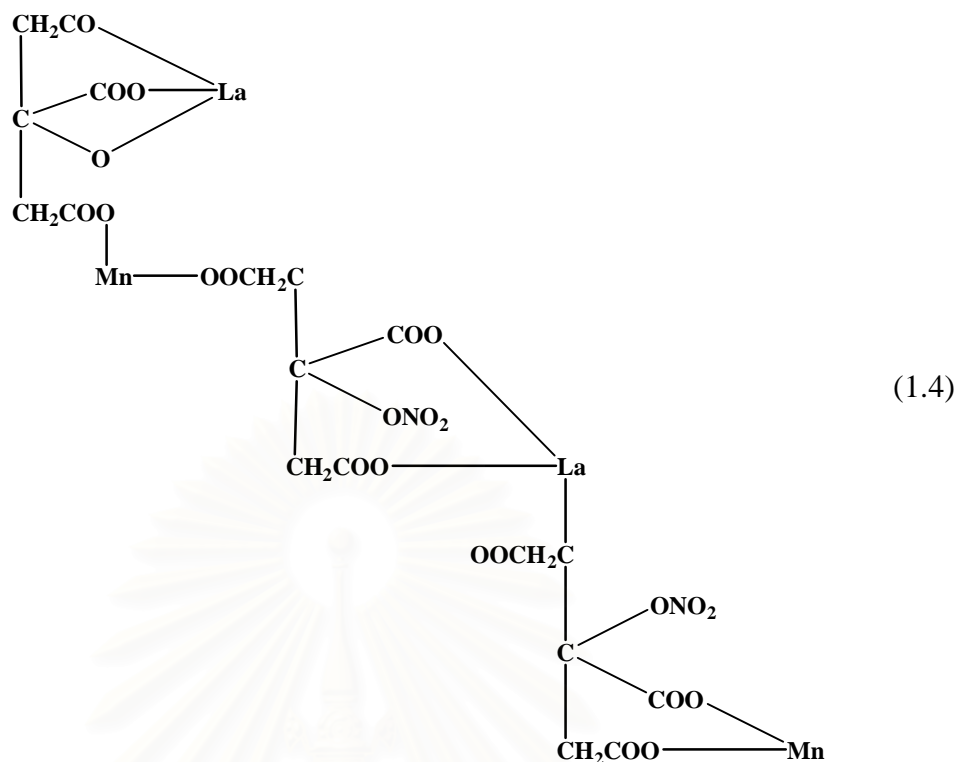
### 1.3.5.3 Solution Reactions

Solution reactions have been developed from solid-state synthesis to produce the required properties of raw perovskite powders, such as spray-pyrolysis, freeze drying, precipitation, sol-gel and liquid mix process, etc. Because of the conventional solid-state synthesis promotes the crystal growth and resulting in a hard agglomeration. The perovskite powders made from solution chemical methods are very fine, and can not be agglomerate, which facilitates the densification process. This method using sintering temperature which can be lower than those made from conventional solid-state synthesis methods.

The initial process was pioneered by Pechini and is referred to either as Pechini process. This method includes first dissolving hydrous oxides or alkoxides of the elements in a polyhydroxy alcohol such as ethylene glycol, with a chelating agent, such as citric acid. Then polyhydroxy alcohol such as ethylene glycol is added and the liquid is heated to 150 to 250°C to allow the chelates to undergo polyesterification. Heating is continued to remove excess water, resulting in solid polymeric resin. The temperature is increased to about 400°C to char or decompose the resin. The temperature is further increased to 500 to 900°C to form crystallites of the mixed oxide composition. The crystallites are typically 20 to 50 nm and clustered into agglomerates. An advantage of the Pechini method is that the viscosity and polymer molecular weight of the solution can be tailored by varying the citric acid/ethylene glycol ratio and the solution synthesis temperature.

The modifications of Pichini process have been developed. One was called amorphous citrate process that involves producing precursor from citric acid and metal nitrate before thermal decomposition. Baythoun and Sale investigate the production of Sr-substituted  $\text{LaMnO}_3$  perovskite powder by the amorphous citrate process, the manganese citrate-nitrate precursor may be revealed as in Equation 1.4 [38]. In the complex the lanthanum is triply charged and replaces in one case the hydrogen of three  $-\text{COOH}$  groups (as in normal citrate formation) and in another case it replaces the hydrogen of one  $-\text{OH}$  group and two  $-\text{COOH}$  groups. Manganese in the divalent state replaces the hydrogen in two  $-\text{COOH}$  groups while  $\text{NO}_2$  replaces the hydrogen of one  $-\text{OH}$  group.

The amounts of metal and citric acid should not be less than equimolar. In all cases the minimum amount of citric acid used was that necessary to bond the metals if all the  $\text{NO}_3^-$  ions were replaced. If the high amount of citric acid was used,  $\text{Mn}_2\text{O}_3$  was presented from the complex as shown in Equation 1.5:



In this case, structure would allow some citric acid, water, and nitrate ions to be lost during the preparation of gel. Every three molecules of citric originally present one remains uncombined and may be removed from the mixture by either evaporation or decomposition to yield acetone, carbon dioxide and water during the precursor preparation in the vacuum oven.

### 1.3.6 Powder Sizing

Powder particles are influenced on compacting and sintering. In most cases the objective of the pressing step is to achieve maximum particle packing and uniformity, so that minimum shrinkage and retained porosity will result during densification. A single particle size does not produce good packing. Optimum packing for particles all the same size results in over 30% void space. Adding particles of a size equivalent to the largest voids reduces the void pore volume to 23%. Therefore, to achieve maximum particle packing, a range of particle sizes is required.

Hard and dense agglomerates in ceramic powders usually result in large interagglomerate pores after sintering. Therefore small particle size is important because it facilitates the high strength of green disc and the sintering process. The primary driving force for densification of a compacted powder at high temperature is the change in surface free energy. Very small particles have high surface areas. The high surface free energy and very strong thermodynamic drive force decrease their surface by bonding them together. The particle with approximate sizes of 1  $\mu\text{m}$  or less can be compacted into a porous shape and sintered at a high temperature to near-theoretical density [39]. Typically, long times of the sintering temperature was a result of the increasing in grain growth which causes lower strength.

### 1.3.7 Sintering

Definitions of the sintering process can be described in term of the permanent chemical and physical change accompanied by the reduced porosity, the mechanism of grain growth, and grain bonding. This process can be accomplished by solid-state reaction or alternatively in the presence of a liquid phase. When a powdered aggregate is sintered, appeared necks form between the particles, and the aggregate may increase in density. The grain growth to the neck form is due to the transport of matter or of the counter-flow of vacancies between the particles and the pores. In crystalline powder, its transport occur by diffusion (bulk diffusion, surface diffusion, or grain boundary diffusion), whereas in amorphous materials, it occurs by viscous flow. It is shown in Figure 1.8. Therefore, the growth of grains

hinders the attainment of theoretical density, and the pore's growth is also enhanced. It is essential, to retard grain growth so that densification of the compact can continue to the theoretical limit. The sintering process can be defined by three stages to happen. The initial stages during which the necks form at points of particle contact and the particles usually center approach each other. At this stage the individual particles are still distinguishable. The intermediate stage during that the necks become large, resulting in the formation of an interconnected pore structure. The final stage during, the pores become isolated. Elimination of the interconnectivity of pores eliminates surface and vapor transport.

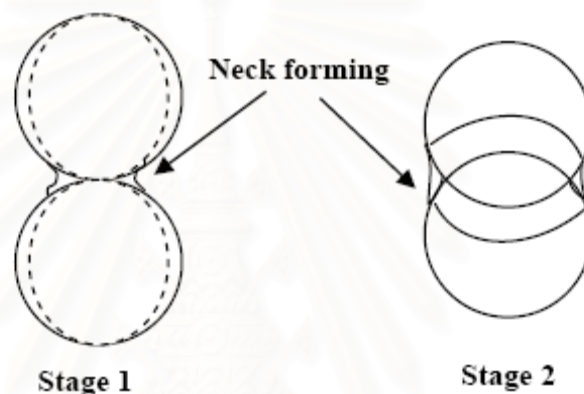


**Figure 1.9** Mechanism of sintering.

#### 1.4 Literature Review

$A_2MO_4$  oxides with the  $K_2NiF_4$ -type structure, represented by a combination of the  $AMO_3$  perovskite and AO rock-salt layers which are arranged one upon the other, have a higher thermochemical stability compared with the  $AMO_3$ -type. In 2003, Daroukh et al. [40] investigated the structural and chemical stabilities, electrical conductivity, and thermal expansion of  $A_{2-x}A'_xMO_4$  oxides ( $A = La$ ,  $A' = Sr$ ,  $M = Mn, Fe, Ni$  and  $Co$ ) and compared with the characteristics of perovskite-type oxides  $AMO_{3-x}$  containing the same cations. The  $K_2NiF_4$ -type manganites, ferrites, cobaltites and nickelates are assumed to be reduction products of the corresponding perovskite-type oxides. The thermodynamic stabilities, in terms of reversible oxygen desorption, were higher than those of the corresponding perovskite-type oxides. The comparison of the oxidation states of  $M$  in  $AMO_{3-x}$  and  $(AMO_{3-x}) \cdot AO$  gives evidence on the stabilizing influence of the AO interlayer



on the perovskite layer. The electrical conductivity of the  $A_2MO_4$  oxides are of p-type and reached values close to  $100 \text{ S cm}^{-1}$  at high oxygen partial pressures and  $800 \text{ }^\circ\text{C}$  for nickelates and cobaltites. At lower oxygen partial pressures the conductivities decrease for the less stable Co- and Ni-based oxides, but less rapidly than for comparable perovskite oxides. The thermal expansion of  $K_2NiF_4$ -type oxides is generally lower than that of the comparable perovskite-type oxides of comparable cationic compositions.

Riza and Ftikos [41] studied the influence of A- and B-site doping on the properties of the system  $La_2CoO_{4\pm\delta}$ . The compounds  $LaSrCo_{0.5}M_{0.5}O_{4\pm\delta}$  ( $M = \text{Co, Fe, Mn, Ni}$ ) and  $La_{1.4}Sr_{0.6}Co_{0.5}M_{0.5}O_{4\pm\delta}$  ( $M = \text{Co, Ni}$ ) were prepared and characterised in order to elucidate the influence of strontium doping on A-site as well as doping with transition metals on B-site of the mixed conductor  $La_2CoO_{4\pm\delta}$ . They reported the doping of B-site improved greatly the electrical conductivity of the mixed conductor  $La_2CoO_{4\pm\delta}$  and slightly increased the linear thermal expansion coefficient. Generally the doped oxides of the  $La_2CoO_{4\pm\delta}$  system exhibited better properties than the equivalent perovskites, with the exception of  $LaSrCoO_{4\pm\delta}$ .

In 2006, Munnings et al. [42] reported structure, stability and electrical properties of the  $La_{2-x}Sr_xMnO_{4\pm\delta}$  solid solution series. Single phase materials with tetragonal structure of the  $La_{2-x}Sr_xMnO_{4\pm\delta}$  ( $0.6 \leq x \leq 2.0$ ) solid solution series show good stability over a wide range of oxygen partial pressures and temperatures. An expansion in lattice volume was observed on increasing lanthanum content. The electrical conductivity of each phase was also determined over a similar temperature range with a maximum value of  $\sim 6 \text{ Scm}^{-1}$  at  $900 \text{ }^\circ\text{C}$  for the  $x = 1.8$  phase.

Recently, Yu and Fung [43] showed effect of the strontium addition on the phase transition of lanthanum copper oxide from  $K_2NiF_4$  to perovskite structure. The substitution of divalent strontium cations ( $Sr^{2+}$ ) for the trivalent lanthanum ions plays an important role on the phase transition of lanthanum copper oxide. Without Sr addition, the sintered  $La_2O_3$  and CuO powder mixture in a mole ratio of 1:2 formed  $K_2NiF_4$ -structured  $La_2CuO_4$  with excess CuO. When 15% of strontium was added,  $La_2CuO_4$  transformed into the single perovskite  $La_{1-x}Sr_xCuO_{2.5-\delta}$  phase with orthorhombic structure. As the strontium addition increased to 20%, the perovskite lattice changed from orthorhombic to tetragonal. These phase transitions may be attributed to the enhanced oxidation of the divalent copper ions

( $\text{Cu}^{2+}$ ) to trivalent ones ( $\text{Cu}^{3+}$ ) by the strontium addition. Based on the electroneutrality in an  $\text{ABO}_3$  perovskite lattice, a divalent cation is unstable in the B-site cation sub-lattice when the A-site is occupied by a trivalent cation such as  $\text{La}^{3+}$ . As strontium was added into the A-site cation sub-lattice, the oxidation of  $\text{Cu}^{2+}$  ion into trivalent  $\text{Cu}^{3+}$  ion was enhanced. The increase of  $\text{Cu}^{3+}$  concentration strengthened the electrostatic bonding (ESB) of copper ions with their neighboring anions. Consequently, the symmetrical tetragonal Sr-doped lanthanum copper oxide was obtained.

In 2004, Yang et al. [44], studied the structure of  $\text{La}_{2-x}\text{Sr}_x\text{CoO}_{4\pm\lambda}$  ( $x = 0.0-1.0$ ) and their catalytic properties in the oxidation of CO and  $\text{C}_3\text{H}_8$ . They prepared  $\text{La}_{2-x}\text{Sr}_x\text{CoO}_{4\pm\lambda}$  ( $x = 0.0-1.0$ ) mixed oxides of  $\text{K}_2\text{NiF}_4$  structure by the polyglycol gel method and used successfully for CO and  $\text{C}_3\text{H}_8$  oxidation. When  $x = 0$ ,  $\text{La}_2\text{CoO}_4$  has orthorhombic  $\text{K}_2\text{NiF}_4$  structure; when  $\text{La}^{3+}$  is substituted by  $\text{Sr}^{2+}$ , whose ionic radius ( $r_{\text{Sr}^{2+}} = 0.1310$  nm) is larger than that of  $\text{La}^{3+}$  ( $r_{\text{La}^{3+}} = 0.1216$  nm), the structure factor increases, and this leads to the structure change from orthorhombic (O) system to tetragonal (T) system. These catalysts possess different catalytic activities towards the oxidation of CO and  $\text{C}_3\text{H}_8$ , and the catalytic activity of  $\text{LaSrCoO}_4$  is better than that of other samples in oxidation reaction. This is explained in terms of their structure: mobile lattice oxygen, content of  $\text{Co}^{3+}$ , particle sizes and BET surface areas.

Jennings and Skinner [45] studied the thermal stability and conduction properties of the  $\text{La}_x\text{Sr}_{2-x}\text{FeO}_{4+\delta}$  system. The thermal stability is excellent and excess oxygen present in the system seems to be crucial for good electronic properties. The composition can be used to tailor the conduction properties.

Vashook et al. [46] studied the transport properties of the  $\text{Pr}_{2-x}\text{Sr}_x\text{NiO}_{4+\delta}$  compositions with  $x = 0.3$  and  $0.6$  and their electrical conductivity for use as SOFC cathode materials. They found that Sr-doping allows partially to stabilize the  $\text{Pr}_2\text{NiO}_{4+\delta}$  structure, but some phase transitions were observed in spite of that. The electrical conductivity and transport properties of the  $\text{Pr}_{2-x}\text{Sr}_x\text{NiO}_{4-\delta}$  compounds are higher than  $\text{La}_{2-x}\text{Sr}_x\text{NiO}_4$ .

In 2006, The perovskite-related oxides  $\text{A}_{2-\alpha}\text{Sr}_\alpha\text{BO}_{4-\delta}$  ( $\text{A} = \text{Pr}, \text{Sm}, \text{B} = \text{Fe}, \text{Co}$ ) were studied to evaluate their potential as cathode materials for IT-SOFCs. Wang et al. [47] showed that the single phase compounds  $\text{A}_{2-\alpha}\text{Sr}_\alpha\text{BO}_{4-\delta}$  ( $\text{A} = \text{Pr}, \text{Sm}, \text{B} = \text{Fe}, \text{Co}, \alpha = 0.8, 1.0, 1.2, 1.5$ ) could be obtained with the  $\text{K}_2\text{NiF}_4$  structure

by solid reaction method. Thermal expansion coefficients (TECs) of the specimens increased with the content of  $\text{Sr}^{2+}$ , and TECs of cobaltites are much higher than that of ferrites. The electrical conductivity increased with the Sr-doping content at lower temperature range for both ferrites and cobaltites. The electrical conductivity increased with temperature in the entire examined temperature range for the compositions with  $\alpha = 0.8, 1.0$ , while it increased up to a maximum value and then decreased for  $\alpha = 1.2, 1.5$ . The conductivity of cobaltites near  $800\text{ }^\circ\text{C}$  is much higher than that of ferrites, and is in the order of  $10^2\text{ S cm}^{-1}$ , which is acceptable for the cathode of IT-SOFCs.  $\text{Sm}_{0.5}\text{Sr}_{1.5}\text{CoO}_{4-\delta}$  exhibits the lowest cathodic overpotential at  $700\text{--}900\text{ }^\circ\text{C}$  ( $72\text{ mV}$  at  $500\text{ mA/cm}^2$  at  $800\text{ }^\circ\text{C}$ ), being a high potential candidate of cathode material for IT-SOFCs.

At the same time, Wen et al. [48] investigated the preparation, thermal expansion, chemical compatibility, electrical conductivity and polarization of  $\text{A}_{2-\alpha}\text{A}'_{\alpha}\text{MO}_4$  ( $\text{A} = \text{Pr, Sm}$ ;  $\text{A}' = \text{Sr}$ ;  $\text{M} = \text{Mn, Ni}$ ;  $\alpha = 0.3, 0.6$ ) as a new cathode for SOFC. The results showed that  $\text{A}_{2-\alpha}\text{A}'_{\alpha}\text{MO}_4$  exhibited a low reactivity with yttria stabilized zirconia (YSZ) electrolyte. The thermal expansion coefficient (TEC) values were changed with the ionic radius of A. The specific conductivities of the nickelates, which were about  $10^2\text{ S cm}^{-1}$  at  $800\text{ }^\circ\text{C}$ , are about one order of magnitude higher than those of manganite. Accordingly, the polarization overpotential of nickelate was lower than that of manganite. Therefore, nickelate  $\text{A}_{2-\alpha}\text{A}'_{\alpha}\text{MO}_4$  exhibited a higher potential to be used as cathode for SOFC after optimizing the composition.

The purpose of this study is to investigate the structure and electrical conductivity of materials from the  $\text{Ln}(\text{Pr, La})_{2-x}\text{Sr}_x\text{MO}_4$  ( $\text{M} = \text{Co, Ni, Cu}$ ) ( $x = 0.4, 0.6, 0.8, 1$ ) for application as electrode materials for SOFC.

## 1.5 The Objectives of the Thesis

1. To synthesize fine particles of the single-phase  $\text{Ln}_{2-x}\text{Sr}_x\text{MO}_4$  ( $\text{Ln} = \text{Pr, La}$ ) ( $\text{M} = \text{Co, Ni, Cu}$ ) ( $x = 0.4, 0.6, 0.8, 1$ ), by using the modified citrate methods and characterize the structure by XRD, IR and SEM.
2. To study the effect of A-site doping on the structures of  $\text{Ln}_{2-x}\text{Sr}_x\text{MO}_4$ .
3. To study oxygen adsorption-desorption property of  $\text{Ln}_{2-x}\text{Sr}_x\text{MO}_4$  by using  $\text{O}_2$ -TPD
4. To study the electrical conductivity of  $\text{Ln}_{2-x}\text{Sr}_x\text{MO}_4$ .

## CHAPTER II

### EXPERIMENTAL

The apparatus and experimental procedures including processing of perovskite powders synthesis, perovskite disc preparation and characterization of materials, are described as below:

#### 2.1 Chemicals

The chemicals listed in Table 2.1, were used without further purification.

**Table 2.1** Chemical and reagents for synthesis of perovskite

Reagents	Formula Weight	Purity%	Company
$\text{La}(\text{NO}_3)_3 \cdot 6\text{H}_2\text{O}$	433.02	$\geq 99$	Fluka
$\text{Pr}(\text{NO}_3)_3 \cdot 6\text{H}_2\text{O}$	435.01	$\geq 99.9$	Misuwa
	435.01	99.9	Aldrich
$\text{Sr}(\text{NO}_3)_2$	211.63	$\geq 99$	Fluka
$\text{Co}(\text{NO}_3)_2 \cdot 6\text{H}_2\text{O}$	291.03	$\geq 98$	Fluka
$\text{Ni}(\text{NO}_3)_2 \cdot 6\text{H}_2\text{O}$	290.79	$\geq 98$	Wako
$\text{Cu}(\text{NO}_3)_2 \cdot 3\text{H}_2\text{O}$	241.6	99–104	Fluka
Citric Acid	192.13	99.5–100.5	Sigma
	192.43	$\geq 99.5$	Fluka
$\text{HNO}_3$	63.01	65	Merck
$\text{NH}_3 \cdot \text{H}_2\text{O}$	35.05	25	Merck
$\text{C}_2\text{H}_5\text{OH}$	46.07	$\geq 99.9$	Merck

## 2.2 Preparations of Perovskite Powders by Modified Citrate Method

All compositions, listed in Table 2.2 were synthesized in basic solution.

**Table 2.2** Composition and abbreviation of  $\text{Ln}_{2-x}\text{Sr}_x\text{MO}_4$

composition	Abbreviation	composition	Abbreviation
$\text{Pr}_2\text{CoO}_4$	-	$\text{La}_2\text{CoO}_4$	-
$\text{Pr}_{1.6}\text{Sr}_{0.4}\text{CoO}_4$	PSCo 1604	$\text{La}_{1.6}\text{Sr}_{0.4}\text{CoO}_4$	LSCo 1604
$\text{Pr}_{1.4}\text{Sr}_{0.6}\text{CoO}_4$	PSCo 1406	$\text{La}_{1.4}\text{Sr}_{0.6}\text{CoO}_4$	LSCo 1406
$\text{Pr}_{1.2}\text{Sr}_{0.8}\text{CoO}_4$	PSCo 1208	$\text{La}_{1.2}\text{Sr}_{0.8}\text{CoO}_4$	LSCo 1208
$\text{PrSrCoO}_4$	PSCo 1010	$\text{LaSrCoO}_4$	LSCo 1010
$\text{Pr}_2\text{NiO}_4$	-	$\text{La}_2\text{NiO}_4$	-
$\text{Pr}_{1.6}\text{Sr}_{0.4}\text{NiO}_4$	PSN 1604	$\text{La}_{1.6}\text{Sr}_{0.4}\text{NiO}_4$	LSN 1604
$\text{Pr}_{1.4}\text{Sr}_{0.6}\text{NiO}_4$	PSN 1406	$\text{La}_{1.4}\text{Sr}_{0.6}\text{NiO}_4$	LSN 1406
$\text{Pr}_{1.2}\text{Sr}_{0.8}\text{NiO}_4$	PSN 1208	$\text{La}_{1.2}\text{Sr}_{0.8}\text{NiO}_4$	LSN 1208
$\text{PrSrNiO}_4$	PSN 1010	$\text{LaSrNiO}_4$	LSN 1010
$\text{Pr}_2\text{CuO}_4$	-	$\text{La}_2\text{CuO}_4$	-
$\text{Pr}_{1.6}\text{Sr}_{0.4}\text{CuO}_4$	PSCu 1604	$\text{La}_{1.6}\text{Sr}_{0.4}\text{CuO}_4$	LSCu 1604
$\text{Pr}_{1.4}\text{Sr}_{0.6}\text{CuO}_4$	PSCu 1406	$\text{La}_{1.4}\text{Sr}_{0.6}\text{CuO}_4$	LSCu 1406
$\text{Pr}_{1.2}\text{Sr}_{0.8}\text{CuO}_4$	PSCu 1208	$\text{La}_{1.2}\text{Sr}_{0.8}\text{CuO}_4$	LSCu 1208
$\text{PrSrCuO}_4$	PSCu 1010	$\text{LaSrCuO}_4$	LSCu 1010

The perovskite powders as shown in Table 2.2 were synthesized by using the modified citrate pyrolysis method. Stoichiometric amounts of corresponding high purity metal nitrates in each composition were partially dissolved into 10 ml ultra pure nitric acid (65 %). Then citric acid was added at a ratio of citric acid to metal ions is 2:1. The mixture solution was stirred at room temperature for 15 hours, and then titrated with conc.  $\text{NH}_3$  at the controlled rate of 2–3 ml/min. The

pH of the solution was adjusted to ~9 and then stirred at room temperature for 5 hours.

The combustion of the homogeneous solution was carried out on a hot plate and the solution was dried at around 100–200 °C by slowly heating temperature in a large size beaker covered with a fine sieve to prevent the loss of fine particle of powders. During combustion process, the homogeneous solution was agitated all the way. The water was evaporated until a sticky gel was obtained. Then it became a large swelling viscous mass and finally self ignited by  $\text{NH}_4\text{NO}_3$  to obtain perovskite oxide powder. The resulting powder was ground by mortar and pestle, subsequently the synthesized perovskite oxide powder was calcined at 1,000 °C for 6 hours in a muffle furnace to achieve phase purity and eliminate the residual organic compound. The condition used for the calcination of the perovskite oxide powders was set as follows:

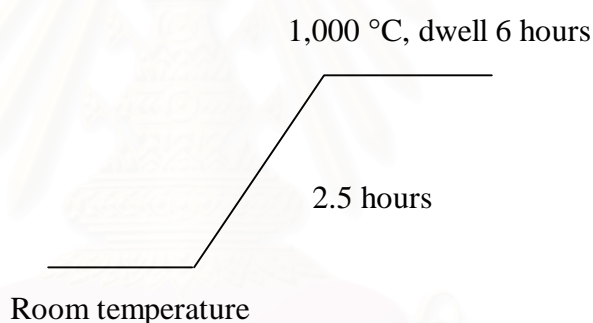


**Figure 2.1** The calcination condition of perovskite oxide powder.

The particle was ground completely well by mortar before characterization.

### 2.3 Perovskite Disc Preparation

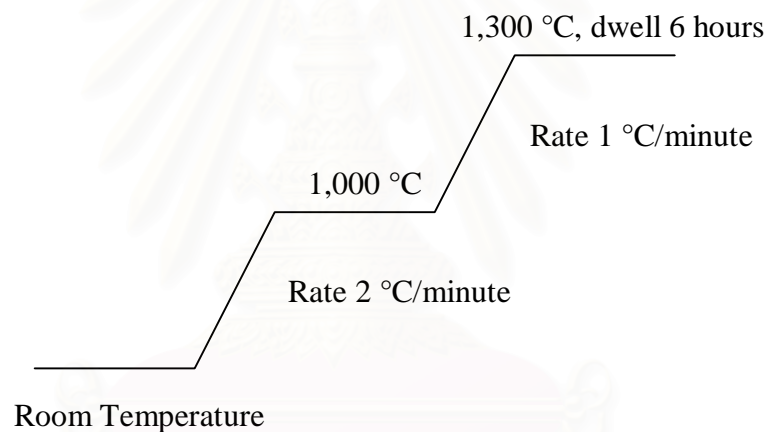
The disc shape of perovskites was formed by KBr die. The KBr die includes loading, pressing and ejecting. The very fine perovskite powder was loaded into the cavity, the plunger was brought to the surface of the powder gently for final leveling and then rotates for smooth surface. About 2 tons was applied on the plunger by the uniaxial pressing machine. At the beginning of pressing, the pressure was slowly applied to 2 tons for 20 minutes. The pressure was released

and then the die was removed from the press. Then the assembly was held while the press until the pellet ejected.

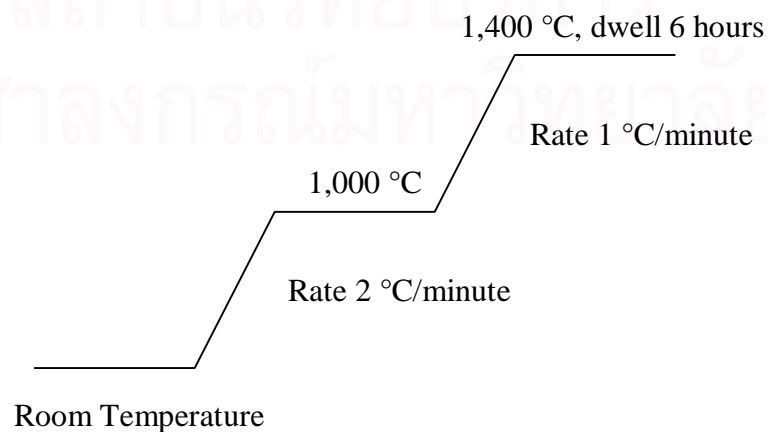
The disc is around 1 mm thick, 13 mm diameter from 1,700–1,800 mg of powder. Then the discs were generally sintered in air at 1,150–1,300°C for 6–10 hours, depending on the composition. Finally the sample was cooled to room temperature.

## 2.4 The Sintering of the Perovskite Oxides

The perovskite membranes were generally sintered in air under different conditions, depending on the composition. The conditions used for the sintering of disc were set as follow:



(a)



(b)

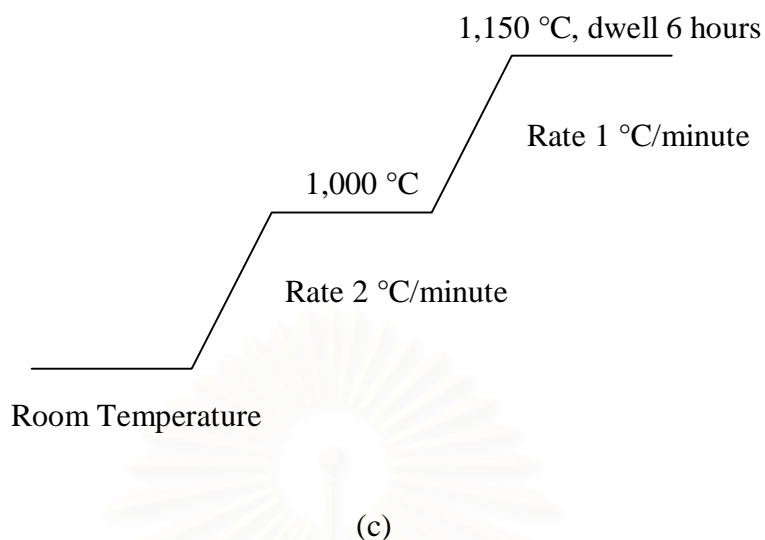


**Figure 2.2** The sintering conditions of  $\text{Ln}(\text{La}, \text{Pr})_{2-x}\text{Sr}_x\text{MO}_4$  (a)  $\text{M} = \text{Co}$  (b)  $\text{M} = \text{Ni}$  and (c)  $\text{M} = \text{Cu}$ .

## 2.5 Characterization Techniques

### 2.5.1 X-Ray Diffractometry (XRD)

The phase formations of perovskite oxide were characterized after calcination and sintering by X-ray powder diffraction (XRD). The XRD patterns, for both powder and disc, were taken by using Rigaku, DMAX 2002 Ultima Plus X-Ray powder diffractometer equipped with a monochromator and a Cu-target X-ray tube (40 kV, 30 mA) and angles of  $2\theta$  ranged from 20–70 degree (step time 0.5 sec., scan step 0.020 degree) at Department of Chemistry, Faculty of Science, Chulalongkorn University.

### 2.5.2 Fourier Transform–Infrared Spectroscopy (FT–IR)

Fourier transform–infrared spectra were recorded on Nicolet FT–IR Impact 410 Spectrophotometer at Department of Chemistry, Chulalongkorn University. The samples were produced in the form of KBr pellets. Infrared spectra were recorded between  $1000\text{--}400\text{ cm}^{-1}$  in transmittance mode.



### 2.5.3 Scanning Electron Microscopy (SEM)

The morphology of the sintered discs was carried out using a JEOL JSM–5800LV scanning electron microscopy, Oxford Instrument (Link ISIS series 300) at the Scientific and Technological Research Equipment Center (STREC), Chulalongkorn University. This instrument uses X-rays or electrons scattered back from the surface “illuminated” by a restored electron beam to generate an image with remarkable three–dimensional qualities.

### 2.5.4 Density

Density of perovskite disc was determined by the Archimedes immersion method using water as a medium, Precisa Gravimetrics AG (model R 2055M–DR), at Department of Chemistry, Faculty of Science, Chulalongkorn University.

### 2.5.5 Temperature–Programmed Desorption (TPD)

The perovskite capabilities of adsorbing O<sub>2</sub> were measured using oxygen temperature–programmed desorption (O<sub>2</sub>–TPD), BEL JAP INC, at Department of Chemistry, Faculty of Science, Chulalongkorn University. The sintered perovskite powder was first pretreated in He atmosphere (30 ml/min) at 500°C for 0.5 hours, then cooled to 100 °C, after which adsorption of gas was performed in a flow of O<sub>2</sub> (5.29% balanced by He) for 40 minutes. About 200 mg of sample was loaded in a U–shape quartz tube. Helium was used as the carrier gas with a flow rate of 40 ml/min. The perovskite powder was first pretreated at 900 °C in He flow for 100 min, after which adsorption of gas was performed in a flow of 99.99% O<sub>2</sub> for 120 minutes, then cooled to 100 °C for 100 minutes. The powder was maintained at 100 °C in He flow for another 30 minutes to eliminate physically adsorbed O<sub>2</sub>. The temperature increased from 100 °C to 900 °C at a rate of 10 °C/min. TCD was used on line with a computer data acquisition system. The values obtained corresponded to the desorb amount of oxygen from the sample.

### 2.5.6 Electrical Conductivity Measurement

The electrical conductivity in air of the specimens was measured by a conventional DC 4-probes method using Pt as an electrode. The sintered disc was cut into a rectangular shape and four electrodes were fabricated with Pt paste. After firing at 950 °C, measurements were performed in the temperature range of room temperature to 800 °C at a rate of 5 °C/min.

In this method a wire is contacted at four locations (pin 1, 2, 3, 4) as shown in Figure 2.3.

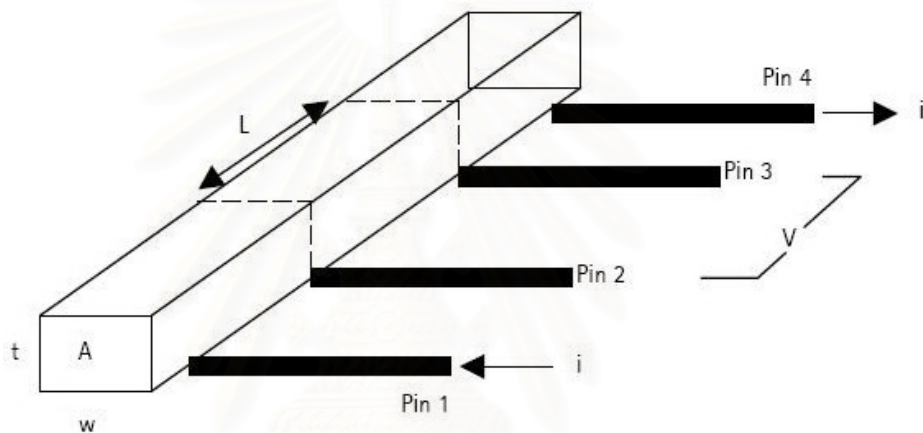


**Figure 2.3** DC four-probe method

The measurement method then includes a forced current  $I$  through the outer pins 1 and 4 and a measurement of the voltage drop over pin 2 and 3, using a very high Ohmic measurement device, so that the current flowing through pin 2 and 3 is nearly zero. In that case the individual, additional contact resistance does not play a role as it cancels out of the equation. To study the behavior of the structure an  $I/V$  curve is generated, typically in the  $\mu\text{A}$  to the  $\text{mA}$  range. If the graph shows a straight line, the structure behaves as an Ohmic resistor [49]. If assume that the resistance of a structure to be  $R$  then the following applies:

$$R = \frac{rL}{A} \quad (2.1)$$

With  $L$  = the length of the structure (m)

$A$  = the area (width x thickness) of the cross section ( $m^2$ )

$\rho$  = the specific resistivity ( $\Omega.m$  of the practical unit  $\mu\Omega.cm$ )



สถาบันวิทยบริการ  
จุฬาลงกรณ์มหาวิทยาลัย

## CHAPTER III

### RESULTS AND DISCUSSIONS

#### 3.1 Synthesis of $\text{Ln}_{2-x}\text{Sr}_x\text{MO}_4$ Perovskite Powder by Modified Citrate Method

The perovskite-like  $\text{Ln}_{2-x}\text{Sr}_x\text{MO}_4$  ( $\text{Ln} = \text{Pr}, \text{La}$ ) ( $\text{M} = \text{Co}, \text{Ni}, \text{Cu}$ ) ( $x = 0.4, 0.6, 0.8, 1$ ) were prepared by the modified citrate method.

The metal nitrates with the corresponding stoichiometric amount were dissolved in 70% nitric acid, which then reacted with citric acid to form metal-citrate-nitrate complexes. These metal-citrate complexes can undergo polymerization when liquid ammonia was added. Meanwhile  $\text{NH}_3\cdot\text{H}_2\text{O}$  was added, the white fume of  $\text{NH}_3\cdot\text{H}_2\text{O}$  was suddenly observed, which came from the free  $\text{NO}_3^-$  reacting with  $\text{NH}_3\cdot\text{H}_2\text{O}$  and generating the heat.

The excess solvent was firstly evaporated until a sticky gel was obtained. Finally, at around  $200^\circ\text{C}$  the spontaneous combustion occurred and the mixture was converted to oxide powder [50].

The features of the samples during preparation were shown in Table 3.1.

สถาบันวิทยบริการ  
จุฬาลงกรณ์มหาวิทยาลัย

**Table 3.1** List of the features of the Ln(Pr, La)<sub>2-x</sub>Sr<sub>x</sub>MO<sub>4</sub> (M = Co, Ni, Cu) (x = 0, 0.4, 0.6, 0.8, 1.0) perovskite compounds during preparation.

Compounds	Solution color	Color changing during adjust pH to ~9	Color and appearance changed after heated at 100-200 °C for 1.5 hours	Material feature
Pr <sub>2</sub> CoO <sub>4</sub>	red	red to dark brown solution	dark brown to purple gel	black powder
Pr <sub>2-x</sub> Sr <sub>x</sub> CoO <sub>4</sub>	red	red to dark brown solution	dark brown to purple gel	black powder
La <sub>2</sub> CoO <sub>4</sub>	red	red to dark brown solution	dark brown to red-purple gel	black powder
La <sub>2-x</sub> Sr <sub>x</sub> CoO <sub>4</sub>	red	red to dark brown solution	dark brown to red-purple gel	black powder
Pr <sub>2</sub> NiO <sub>4</sub>	green	green to dark blue solution	dark blue to green gel	black powder
Pr <sub>2-x</sub> Sr <sub>x</sub> NiO <sub>4</sub>	green	green to dark blue solution	dark blue to green gel	black powder
La <sub>2</sub> NiO <sub>4</sub>	green	green to blue solution	blue solution to blue gel	black powder
La <sub>2-x</sub> Sr <sub>x</sub> NiO <sub>4</sub>	green	green to blue solution	blue solution to blue gel	black powder
Pr <sub>2</sub> CuO <sub>4</sub>	green	green to dark blue solution	dark blue to dark blue gel	black powder
Pr <sub>2-x</sub> Sr <sub>x</sub> CuO <sub>4</sub>	green	green to dark blue solution	dark blue to dark blue gel	dark brown powder
La <sub>2</sub> CuO <sub>4</sub>	blue	blue to dark blue solution	dark blue to blue gel	black powder
La <sub>2-x</sub> Sr <sub>x</sub> CuO <sub>4</sub>	blue	blue to dark blue solution	dark blue to blue gel	dark brown powder

### 3.2 Tolerance Number of Perovskite Compounds

The stability of the compounds was determined by using tolerance numbers calculated from the below equation:

$$t = \frac{(r_A + r_O)}{\sqrt{2}(r_B + r_O)} \quad (3.1)$$

Apparent  $t$  values were calculated based on the following chemical formula without the formation of oxide ion vacancy and equations for the calculation of average ionic radius.

The tolerance numbers of all the prepared oxides are presented in Table 3.2.

**Table 3.2** The tolerance numbers of all the prepared perovskites

Compounds	Tolerance No.	Compounds	Tolerance No.
Pr <sub>2</sub> CoO <sub>4</sub>	0.8502	La <sub>2</sub> CoO <sub>4</sub>	0.8624
Pr <sub>1.6</sub> Sr <sub>0.4</sub> CoO <sub>4</sub>	0.8588	La <sub>1.6</sub> Sr <sub>0.4</sub> CoO <sub>4</sub>	0.8686
Pr <sub>1.4</sub> Sr <sub>0.6</sub> CoO <sub>4</sub>	0.8631	La <sub>1.4</sub> Sr <sub>0.6</sub> CoO <sub>4</sub>	0.8717
Pr <sub>1.2</sub> Sr <sub>0.8</sub> CoO <sub>4</sub>	0.8675	La <sub>1.2</sub> Sr <sub>0.8</sub> CoO <sub>4</sub>	0.8748
PrSrCoO <sub>4</sub>	0.8718	LaSrCoO <sub>4</sub>	0.8779
Pr <sub>2</sub> NiO <sub>4</sub>	0.8725	La <sub>2</sub> NiO <sub>4</sub>	0.8851
Pr <sub>1.6</sub> Sr <sub>0.4</sub> NiO <sub>4</sub>	0.8814	La <sub>1.6</sub> Sr <sub>0.4</sub> NiO <sub>4</sub>	0.8914
Pr <sub>1.4</sub> Sr <sub>0.6</sub> NiO <sub>4</sub>	0.8858	La <sub>1.4</sub> Sr <sub>0.6</sub> NiO <sub>4</sub>	0.8946
Pr <sub>1.2</sub> Sr <sub>0.8</sub> NiO <sub>4</sub>	0.8903	La <sub>1.2</sub> Sr <sub>0.8</sub> NiO <sub>4</sub>	0.8978
PrSrNiO <sub>4</sub>	0.8947	LaSrNiO <sub>4</sub>	0.9010
Pr <sub>2</sub> CuO <sub>4</sub>	0.8562	La <sub>2</sub> CuO <sub>4</sub>	0.8684
Pr <sub>1.6</sub> Sr <sub>0.4</sub> CuO <sub>4</sub>	0.8649	La <sub>1.6</sub> Sr <sub>0.4</sub> CuO <sub>4</sub>	0.8747
Pr <sub>1.4</sub> Sr <sub>0.6</sub> CuO <sub>4</sub>	0.8692	La <sub>1.4</sub> Sr <sub>0.6</sub> CuO <sub>4</sub>	0.8778
Pr <sub>1.2</sub> Sr <sub>0.8</sub> CuO <sub>4</sub>	0.8736	La <sub>1.2</sub> Sr <sub>0.8</sub> CuO <sub>4</sub>	0.8809
PrSrCuO <sub>4</sub>	0.8779	LaSrCuO <sub>4</sub>	0.8840

The tolerance numbers of all the prepared oxides were calculated by using Shannon's ionic radii.  $\text{Pr}_2\text{CoO}_4$ ,  $\text{La}_2\text{CoO}_4$  and  $\text{Pr}_2\text{CuO}_4$ , in which no Sr was involved, the tolerance number calculated was 0.85, which was near to the threshold of compounds with tetragonal  $\text{K}_2\text{NiF}_4$  structure ( $0.85 < t < 1.02$ ) [51]. Hence, it was in orthorhombic (O) structure. After  $\text{Pr}^{3+}$  and  $\text{La}^{3+}$  is substituted by  $\text{Sr}^{2+}$ , whose ionic radius ( $r_{\text{Sr}^{2+}} = 0.1310$  nm) is larger than that of  $\text{Pr}^{3+}$  ( $r_{\text{Pr}^{3+}} = 0.1179$  nm) and  $\text{La}^{3+}$  ( $r_{\text{La}^{3+}} = 0.1216$  nm), the tolerance number increased and the symmetry of structure improved, resulting in the transformation of structure from orthorhombic to tetragonal.

### 3.3 Characterization of the Perovskite Compounds

For the synthesis study, the calcinations and sintering process are concerned. The effect of calcination process is in general favorable, predictable and related to the improvement of crystalline structure of as-synthesized powders. This process also removed residual water and other impurities. In case of sintering process, the effect of heat treatment is related to the substantial changes in all powder microstructures.

The structures of synthesized perovskite compounds were characterized by XRD, IR and the surface morphology of the sintered disc was examined by SEM.

#### 3.3.1 X-ray Diffraction (XRD)

XRD was used to indicate the formation of the perovskite-type phase with either a  $\text{K}_2\text{NiF}_4$  or distorted  $\text{K}_2\text{NiF}_4$  structure. The phase formations of perovskites were characterized after calcinations and sintering. The diffraction peaks of perovskites were observed within  $2\theta$  in the range of  $20^\circ$  to  $70^\circ$ .

In this study, the effects of the dopant Sr at A-site on the structure of  $\text{Pr}_2\text{MO}_4$  and  $\text{La}_2\text{MO}_4$  ( $M = \text{Co}, \text{Ni}$  and  $\text{Cu}$ ) were investigated.

### 3.3.1.1 Phase Formation of $\text{Pr}_{2-x}\text{Sr}_x\text{CoO}_4$ ( $x = 0, 0.4, 0.6, 0.8$ and $1.0$ )

XRD patterns of  $\text{Pr}_{2-x}\text{Sr}_x\text{CoO}_4$  ( $x = 0, 0.4, 0.6, 0.8$  and  $1.0$ ) discs were presented in Figure 3.1.

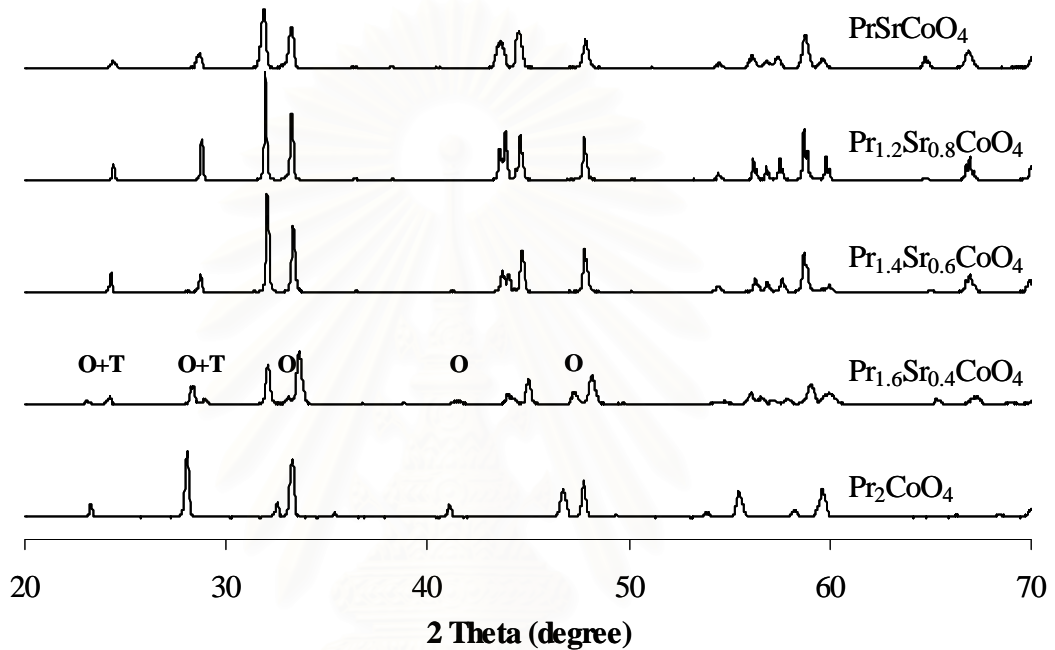


**Figure 3.1** The XRD patterns of  $\text{Pr}_{2-x}\text{Sr}_x\text{CoO}_4$  ( $x = 0, 0.4, 0.6, 0.8$  and  $1.0$ ) after sintered at  $1300^\circ\text{C}$  for 6 hours

The XRD patterns of the  $\text{Pr}_{2-x}\text{Sr}_x\text{CoO}_4$  showed that all the diffraction peaks belong to the  $\text{K}_2\text{NiF}_4$  phase. Moreover, their structures change with the change of  $x$ . When  $x = 0$ , the obtained sample  $\text{Pr}_2\text{CoO}_4$  has orthorhombic  $\text{K}_2\text{NiF}_4$  structure. When  $\text{Pr}^{3+}$  is substituted by  $\text{Sr}^{2+}$ , whose ionic radius ( $r_{\text{Sr}^{2+}} = 0.1310$  nm) is larger than that of  $\text{Pr}^{3+}$  ( $r_{\text{Pr}^{3+}} = 0.1179$  nm), leads to the structure change from orthorhombic (O) system to tetragonal (T) system. In the composition of  $x = 0.4$ , the mixed oxides have mixed orthorhombic and tetragonal  $\text{K}_2\text{NiF}_4$  structure, when in the range of  $0.6 \leq x \leq 1.0$ , the mixed oxides have pure tetragonal  $\text{K}_2\text{NiF}_4$  structure.



### 3.3.1.2 Phase Formation of $\text{La}_{2-x}\text{Sr}_x\text{CoO}_4$ ( $x = 0, 0.4, 0.6, 0.8$ and 1.0)

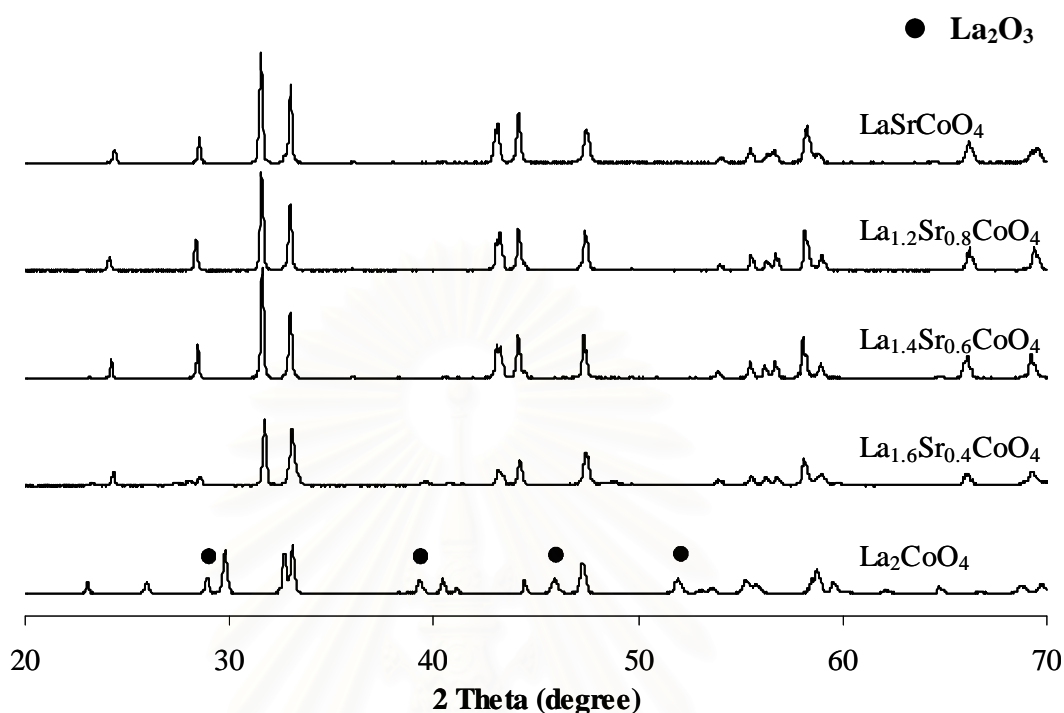


**Figure 3.2** The XRD patterns of  $\text{La}_{2-x}\text{Sr}_x\text{CoO}_4$  ( $x = 0, 0.4, 0.6, 0.8$  and 1.0) after sintered at  $1300^\circ\text{C}$  for 6 hours

Figure 3.2 shows the XRD patterns of  $\text{La}_{2-x}\text{Sr}_x\text{CoO}_4$  ( $x = 0, 0.4, 0.6, 0.8$  and 1.0) with  $\text{K}_2\text{NiF}_4$ -type structure. The diffraction pattern of undoped  $\text{La}_2\text{CoO}_4$  exhibited the orthorhombic structure. The formation of  $\text{La}_2\text{O}_3$  (PDF 83-1344), marked with ●, was also observed. When  $\text{La}^{3+}$  is substituted by  $\text{Sr}^{2+}$  ( $x = 0.4-1.0$ ), the XRD pattern displays pure tetragonal  $\text{K}_2\text{NiF}_4$ -type structure. In order to maintain the charge neutrality, the oxidation state of  $\text{Co}^{2+}$  changed to  $\text{Co}^{3+}$ . According to smaller size of  $\text{Co}^{3+}$  ( $r_{\text{Co}^{3+}} = 0.0630 \text{ nm}$ ), the bond of  $\text{Co-O}$  in  $\text{Co-O}$  plane becomes strength and the bond distance becomes shorter. Then the crystal structure of doped  $\text{La}_2\text{CoO}_4$  changed from orthorhombic to tetragonal.

The slightly shift of characteristic peak was observed when the amount of  $\text{Sr}^{2+}$  doping increased, which is the result of lattice expansion.

### 3.3.1.3 Phase Formation of $\text{Pr}_{2-x}\text{Sr}_x\text{NiO}_4$ ( $x = 0, 0.4, 0.6, 0.8$ and 1.0)

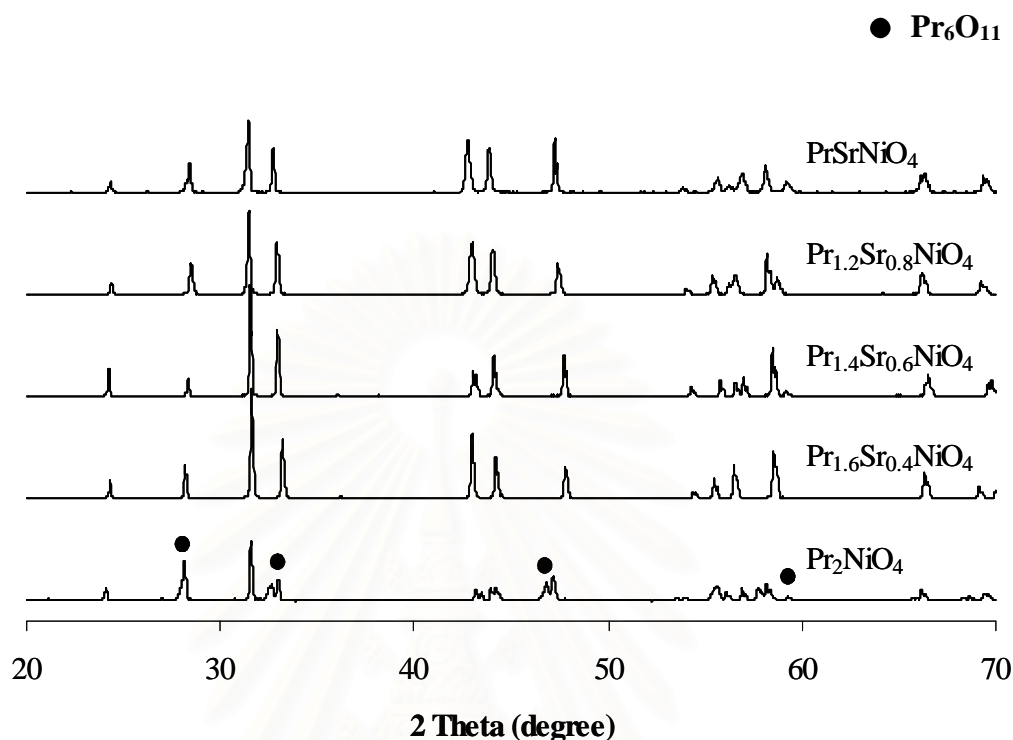


**Figure 3.3** The XRD patterns of  $\text{Pr}_{2-x}\text{Sr}_x\text{NiO}_4$  ( $x = 0, 0.4, 0.6, 0.8$  and 1.0) after sintered at  $1400^\circ\text{C}$  for 6 hours

Figure 3.3 exhibits the  $\text{K}_2\text{NiF}_4$  diffraction peaks. For  $\text{Pr}_2\text{NiO}_4$  showed the orthorhombic phase and the appearance of the small peaks (marked with ●) at  $2\theta = 28^\circ, 32^\circ, 46^\circ$  and  $58^\circ$  indicated the existence of secondary phase of  $\text{Pr}_6\text{O}_{11}$  (PDF 42–1121). The prepared  $\text{Pr}_{2-x}\text{Sr}_x\text{NiO}_4$  compositions with  $x = 0.4–1.0$  were found as tetragonal single phase. Doping Sr at Pr-site of  $\text{Pr}_2\text{NiO}_4$  caused the structure change from orthorhombic to tetragonal.

### 3.3.1.4 Phase Formation of $\text{La}_{2-x}\text{Sr}_x\text{NiO}_4$ ( $x = 0, 0.4, 0.6, 0.8$ and 1.0)

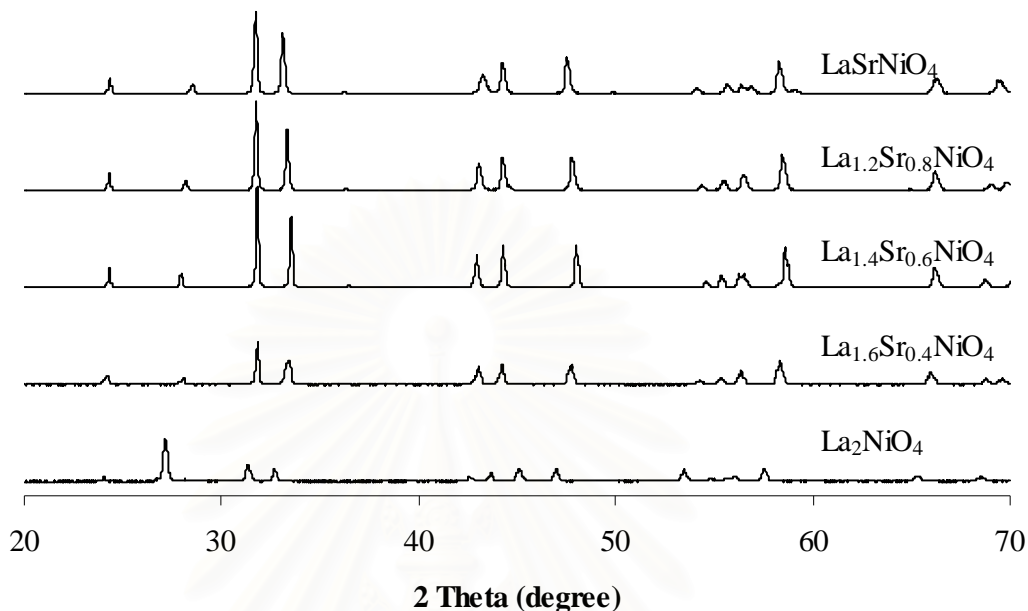


**Figure 3.4** The XRD patterns of  $\text{La}_{2-x}\text{Sr}_x\text{NiO}_4$  ( $x = 0, 0.4, 0.6, 0.8$  and 1.0) after sintered at  $1400^\circ\text{C}$  for 6 hours

Figure 3.4 shows the XRD patterns of the sintered discs. All of them were single  $\text{K}_2\text{NiF}_4$ -type with orthorhombic or tetragonal structure. At  $x = 0$ , the compound had orthorhombic structure. After the substitution of  $\text{Sr}^{2+}$  (larger radius) for  $\text{La}^{3+}$  (smaller radius), the tolerance factor increased. Hence, improved, resulting in the transformation of structure from orthorhombic to tetragonal.

The XRD results showed that  $\text{La}_{2-x}\text{Sr}_x\text{NiO}_4$  exhibited a similar structure to the  $\text{Pr}_{2-x}\text{Sr}_x\text{NiO}_4$ . It may be due to the fact that Pr belongs to the La on the periodic table of element and their ionic radii are 0.1179 nm and 0.1216 nm, respectively. In addition, Pr and La have the same electronic shell of  $5d^0 6s^2$  apart from different inner shell electrons [52]. Hence it could be expected that  $\text{Pr}_{2-x}\text{Sr}_x\text{NiO}_4$  and  $\text{La}_{2-x}\text{Sr}_x\text{NiO}_4$  would possess resembling chemical properties and structural type.

### 3.3.1.5 Phase Formation of $\text{Pr}_{2-x}\text{Sr}_x\text{CuO}_4$ ( $x = 0, 0.4, 0.6, 0.8$ and 1.0)

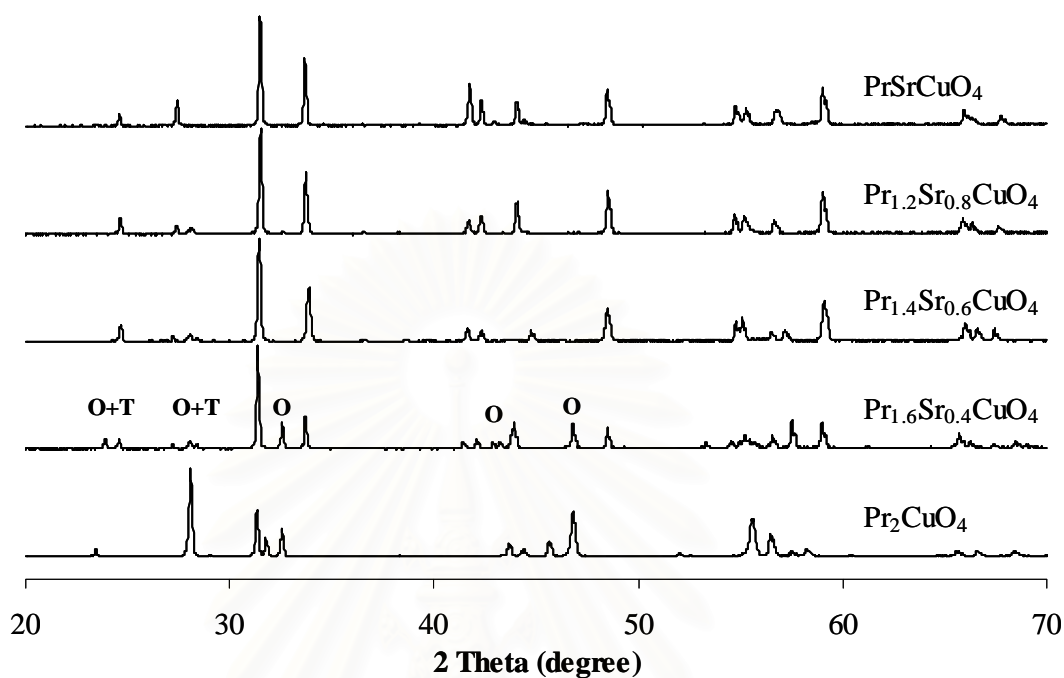


**Figure 3.5** The XRD patterns of  $\text{Pr}_{2-x}\text{Sr}_x\text{CuO}_4$  ( $x = 0, 0.4, 0.6, 0.8$  and 1.0) after sintered at  $1150^\circ\text{C}$  for 6 hours

Figure 3.5 illustrates the prepared  $\text{Pr}_2\text{CuO}_4$  as single orthorhombic phase. The formation of the  $\text{Pr}_{2-x}\text{Sr}_x\text{CuO}_4$  ( $x = 0.4, 0.6, 0.8$  and 1.0) with tetragonal crystal structure analogous to the corresponding  $\text{Pr}_{2-x}\text{Sr}_x\text{CoO}_4$  was presented in Figure 3.1. The XRD patterns of  $\text{Pr}_{2-x}\text{Sr}_x\text{CuO}_4$  when the Sr content was higher than 0.4 showed the single tetragonal phase when the Sr content was 0.4 the mixed phase of orthorhombic and tetragonal appeared.

### 3.3.1.6 Phase Formation of $\text{La}_{2-x}\text{Sr}_x\text{CuO}_4$ ( $x = 0, 0.4, 0.6, 0.8$ and 1.0)

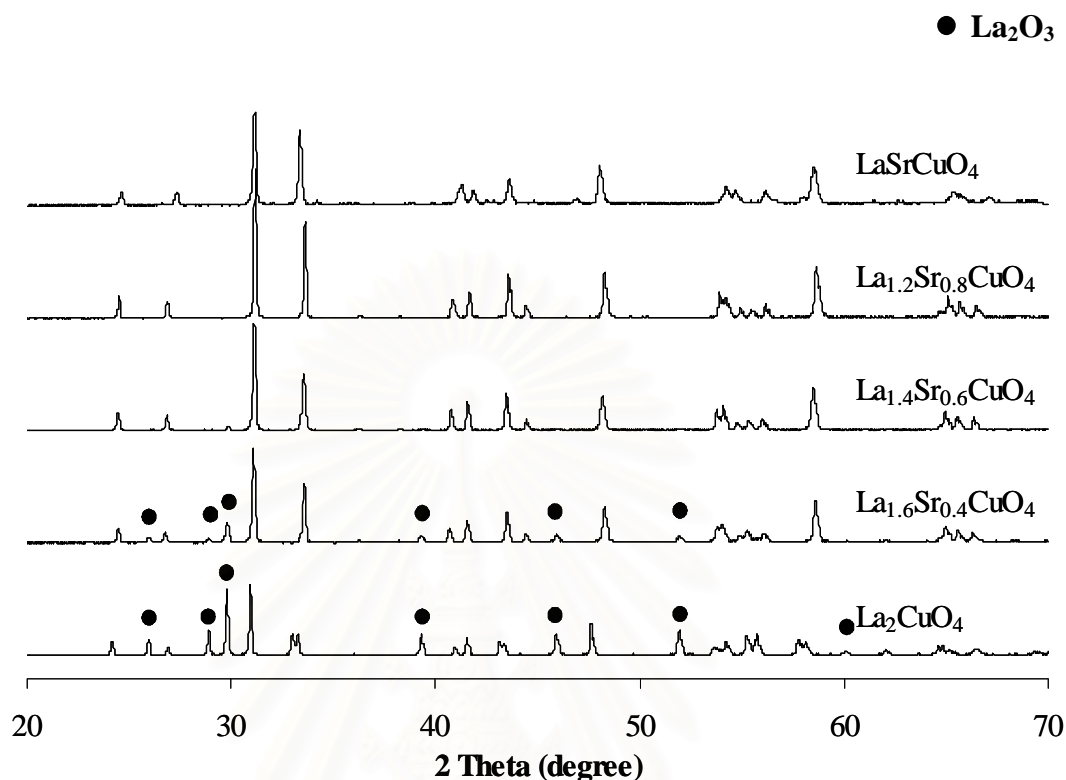


**Figure 3.6** The XRD patterns of  $\text{La}_{2-x}\text{Sr}_x\text{CuO}_4$  ( $x = 0, 0.4, 0.6, 0.8$  and 1.0) after sintered at  $1150^\circ\text{C}$  for 6 hours

The XRD patterns of  $\text{La}_{2-x}\text{Sr}_x\text{CuO}_4$  showed the similar result with  $\text{Pr}_{2-x}\text{Sr}_x\text{CuO}_4$ . The patterns of  $\text{La}_2\text{CuO}_4$  reveal the orthorhombic structure, while the composition with  $x = 0.4, 0.6, 0.8$  and 1.0 have tetragonal structure. The formation of  $\text{La}_2\text{O}_3$  (PDF 83–1344) was observed in compositions with  $x = 0$  and 0.4, which is recognized from the main peak at  $2\theta = 30^\circ$ , when A-site cations  $\text{La}^{3+}$  were substituted by low valence cations  $\text{Sr}^{2+}$ , the average oxidation number of B-site cations will increase, caused the changed in crystal structure from orthorhombic to tetragonal structure.

For XRD patterns of cobaltate and nickelate series, it was observed that the peaks of doped  $\text{Sr}^{2+}$  specimens are slightly shifted to the lower angle when increasing of  $\text{Sr}^{2+}$  (For  $x = 0.4$ –1.0). See XRD partial patterns in Figure 3.7 (a), (b), (c) and (d).

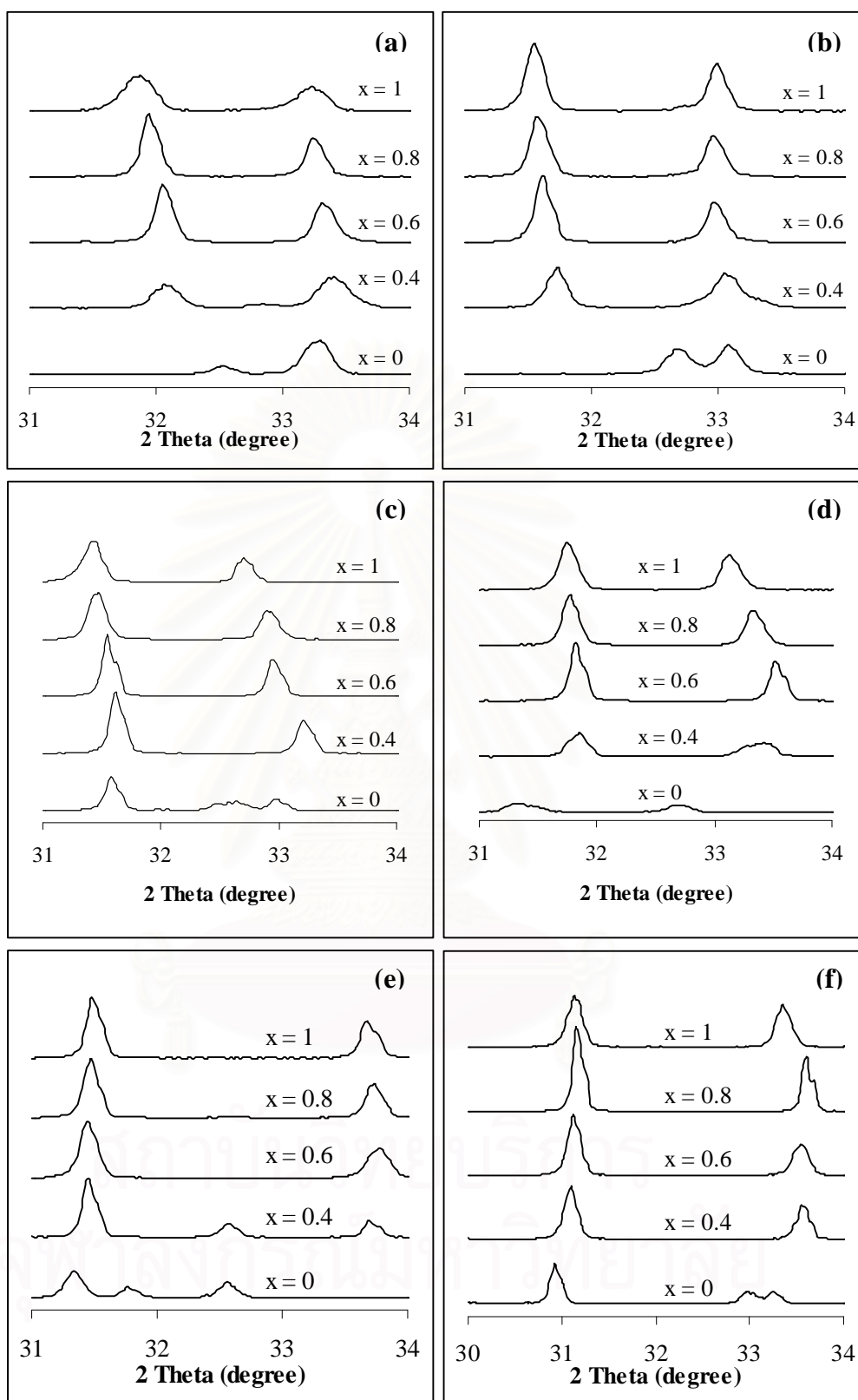


**Figure 3.7** Partial XRD patterns of perovskite discs (a)  $\text{Pr}_{2-x}\text{Sr}_x\text{CoO}_4$ , (b)  $\text{La}_{2-x}\text{Sr}_x\text{CoO}_4$ , (c)  $\text{Pr}_{2-x}\text{Sr}_x\text{NiO}_4$ , (d)  $\text{La}_{2-x}\text{Sr}_x\text{NiO}_4$ , (e)  $\text{Pr}_{2-x}\text{Sr}_x\text{CuO}_4$  and (f)  $\text{La}_{2-x}\text{Sr}_x\text{CuO}_4$  with various Sr contents.

This shift is considered to be the result from the expansion of crystal lattice caused by substitution of  $\text{Pr}^{3+}$  or  $\text{La}^{3+}$  (smaller ionic radius) with  $\text{Sr}^{2+}$  (larger ionic radius), that which follow to the Bragg's law as shown in equation 3.2:

$$2d \sin \theta = n\lambda \quad (3.2)$$

In the case of cuprate series, as shown in Figure 3.7 (e) and (f), the shift of XRD peaks seems to be different. This might be ascribed to the increase of the average oxidation number of Cu ion resulted by the addition of low valence of  $\text{Sr}^{2+}$ .

From XRD analysis, the results of crystalline phase analysis of prepared samples are summarized in Table 3.3. All compositions were prepared by the modified citrate method showed the existence of  $\text{K}_2\text{NiF}_4$  phase having orthorhombic and tetragonal structure.

**Table 3.3** Summary of the XRD analysis of prepared disc samples

Composition	Crystal system	Phase(s)
$\text{Pr}_2\text{CoO}_4$	orthorhombic	$\text{K}_2\text{NiF}_4$
PSCo1604	orthorhombic + tetragonal	$\text{K}_2\text{NiF}_4$
PSCo1406	tetragonal	$\text{K}_2\text{NiF}_4$
PSCo1208	tetragonal	$\text{K}_2\text{NiF}_4$
PSCo1010	tetragonal	$\text{K}_2\text{NiF}_4$
$\text{La}_2\text{CoO}_4$	orthorhombic	$\text{K}_2\text{NiF}_4 + \text{La}_2\text{O}_3$
LSCo1604	tetragonal	$\text{K}_2\text{NiF}_4$
LSCo1406	tetragonal	$\text{K}_2\text{NiF}_4$
LSCo1208	tetragonal	$\text{K}_2\text{NiF}_4$
LSCo1010	tetragonal	$\text{K}_2\text{NiF}_4$
$\text{Pr}_2\text{NiO}_4$	orthorhombic	$\text{K}_2\text{NiF}_4 + \text{Pr}_6\text{O}_{11}$
PSN1604	tetragonal	$\text{K}_2\text{NiF}_4$
PSN1406	tetragonal	$\text{K}_2\text{NiF}_4$
PSN1208	tetragonal	$\text{K}_2\text{NiF}_4$
PSN1010	tetragonal	$\text{K}_2\text{NiF}_4$
$\text{La}_2\text{NiO}_4$	orthorhombic	$\text{K}_2\text{NiF}_4$
LSN1604	tetragonal	$\text{K}_2\text{NiF}_4$
LSN1406	tetragonal	$\text{K}_2\text{NiF}_4$
LSN1208	tetragonal	$\text{K}_2\text{NiF}_4$
LSN1010	tetragonal	$\text{K}_2\text{NiF}_4$

**Table 3.3** Summary of the XRD analysis of prepared disc samples (cont.)

Composition	Crystal system	Phase(s)
Pr <sub>2</sub> CuO <sub>4</sub>	orthorhombic	K <sub>2</sub> NiF <sub>4</sub>
PSCu1604	orthorhombic + tetragonal	K <sub>2</sub> NiF <sub>4</sub>
PSCu1406	tetragonal	K <sub>2</sub> NiF <sub>4</sub>
PSCu1208	tetragonal	K <sub>2</sub> NiF <sub>4</sub>
PSCu1010	tetragonal	K <sub>2</sub> NiF <sub>4</sub>
La <sub>2</sub> CuO <sub>4</sub>	orthorhombic	K <sub>2</sub> NiF <sub>4</sub> + La <sub>2</sub> O <sub>3</sub>
LSCu1604	tetragonal	K <sub>2</sub> NiF <sub>4</sub> + La <sub>2</sub> O <sub>3</sub>
LSCu1406	tetragonal	K <sub>2</sub> NiF <sub>4</sub>
LSCu1208	tetragonal	K <sub>2</sub> NiF <sub>4</sub>
LSCu1010	tetragonal	K <sub>2</sub> NiF <sub>4</sub>

Although, all of the above perovskite oxides can be prepared but the synthesized Pr<sub>2-x</sub>Sr<sub>x</sub>CoO<sub>4</sub> and La<sub>2-x</sub>Sr<sub>x</sub>CoO<sub>4</sub> series had physical instability after sintering as presented in Figure 3.8. Therefore we cannot do the further investigations on the morphology and the properties of these oxides.

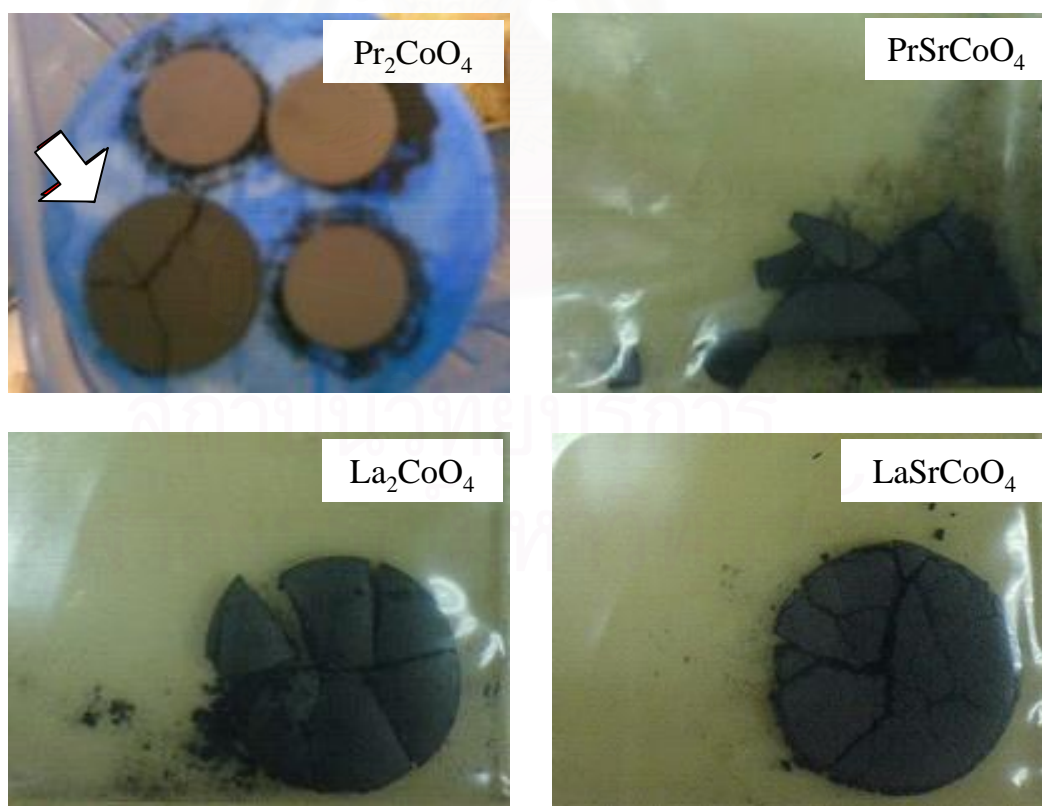


**Figure 3.8** The examples of prepared instability perovskite discs after sintered for 3 days.



### 3.3.2 Fourier Transform–Infrared Spectroscopy (FT–IR)

Infrared spectra (IR) in the range 1000–400  $\text{cm}^{-1}$  were recorded. Results obtained from IR spectra supported the above results were analyzed from XRD patterns.

#### 3.3.2.1 Spectroscopic Behaviour of $\text{Pr}_{2-x}\text{Sr}_x\text{NiO}_4$ ( $x = 0, 0.4, 0.6, 0.8$ and $1.0$ )

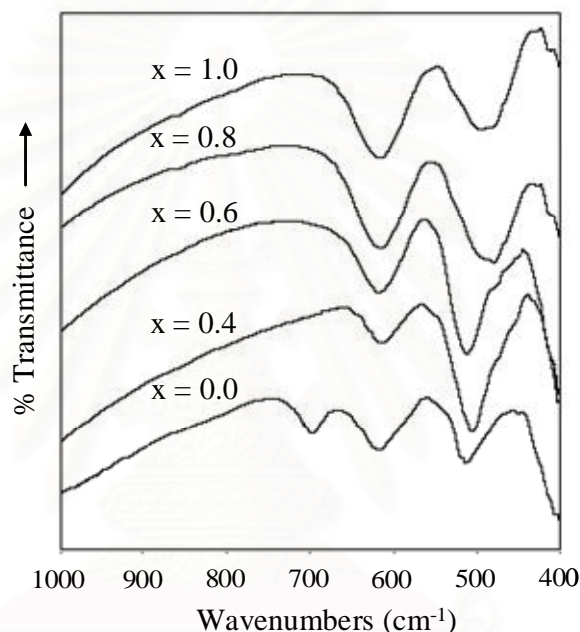


**Figure 3.9** FT–IR spectra of  $\text{Pr}_{2-x}\text{Sr}_x\text{NiO}_4$  ( $x = 0, 0.4, 0.6, 0.8$  and  $1.0$ )

From Figure 3.9, all the samples had the vibrational absorption band in the regions 680–600 and around 520–500  $\text{cm}^{-1}$ . It is proved that these samples have  $\text{K}_2\text{NiF}_4$ -type  $\text{A}_2\text{BO}_4$  structure [50, 52] according to the absorption band around 520–500  $\text{cm}^{-1}$  attributed to the stretching vibration of A–O–B of the  $\text{A}_2\text{BO}_4$  [53]. The absorption band at 680  $\text{cm}^{-1}$  of  $\text{Pr}_2\text{NiO}_4$  indicated that it has in orthorhombic structure. For doped- $\text{Pr}_2\text{NiO}_4$  oxides, the absorption band at 680  $\text{cm}^{-1}$  disappeared. It might be that the crystal structure was transformed from orthorhombic to tetragonal when  $\text{Pr}_2\text{NiO}_4$  was doped with  $\text{Sr}^{2+}$ .

### 3.3.2.2 Spectroscopic Behaviour of $\text{La}_{2-x}\text{Sr}_x\text{NiO}_4$ ( $x = 0, 0.4, 0.6, 0.8$ and $1.0$ )

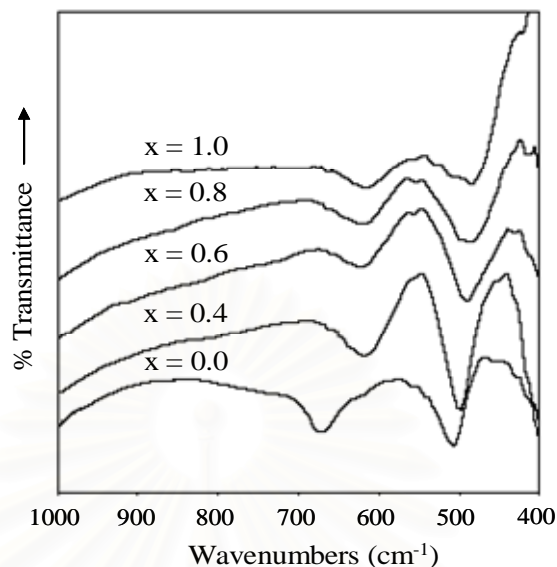


**Figure 3.10** FT-IR spectra of  $\text{La}_{2-x}\text{Sr}_x\text{NiO}_4$  ( $x = 0, 0.4, 0.6, 0.8$  and  $1.0$ )

The prepared perovskite oxides  $\text{La}_{2-x}\text{Sr}_x\text{NiO}_4$  ( $x = 0, 0.4, 0.6, 0.8$  and  $1.0$ ) shows IR absorption band, displayed in Figure 3.10, at about approximately  $520\text{--}500\text{ cm}^{-1}$ , which could be attributed to the characteristic absorption band of  $\text{K}_2\text{NiF}_4$ -type structure as well.  $\text{La}_2\text{NiO}_4$  had a vibration band around  $680\text{ cm}^{-1}$ , but the other had not, which was due to their differences in crystal structures.

### 3.3.2.3 Spectroscopic Behaviour of $\text{Pr}_{2-x}\text{Sr}_x\text{CuO}_4$ ( $x = 0, 0.4, 0.6, 0.8$ and $1.0$ )

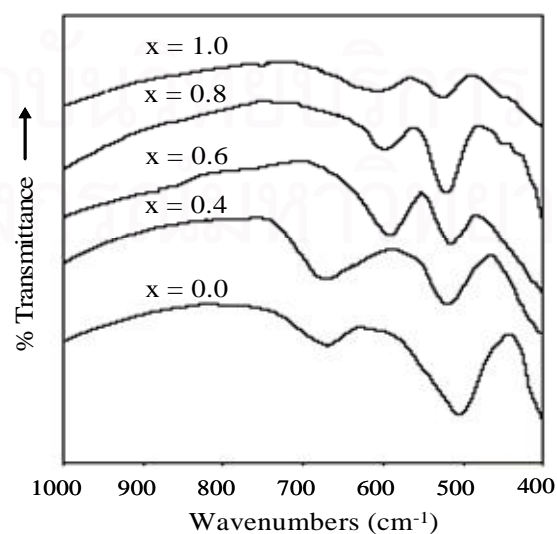


**Figure 3.11** FT-IR spectra of  $\text{Pr}_{2-x}\text{Sr}_x\text{CuO}_4$  ( $x = 0, 0.4, 0.6, 0.8$  and  $1.0$ )

IR spectroscopic results support the structure analysis by XRD. Figure 3.11 depicts the observed IR spectra of  $\text{Pr}_{2-x}\text{Sr}_x\text{CuO}_4$  ( $x = 0, 0.4, 0.6, 0.8$  and  $1.0$ ). All sample had the vibrational absorption band at around  $520\text{--}500\text{ cm}^{-1}$ , which is the characteristic band of compounds with  $\text{K}_2\text{NiF}_4$  structure. In addition,  $\text{Pr}_2\text{CuO}_4$  and  $\text{Pr}_{1.6}\text{Sr}_{0.4}\text{CuO}_4$  had an absorption band at  $680\text{ cm}^{-1}$ , indicated that it was in orthorhombic structure whereas the other was in tetragonal structure which is consistent with XRD results.

### 3.3.2.4 Spectroscopic Behaviour of $\text{La}_{2-x}\text{Sr}_x\text{CuO}_4$ ( $x = 0, 0.4, 0.6, 0.8$ and $1.0$ )

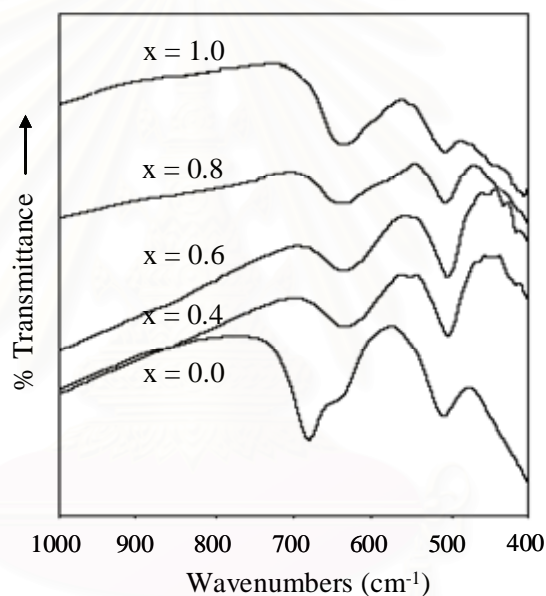


**Figure 3.12** FT-IR spectra of  $\text{La}_{2-x}\text{Sr}_x\text{CuO}_4$  ( $x = 0, 0.4, 0.6, 0.8$  and  $1.0$ )

From IR result in Figure 3.12, all samples had an absorption band at around  $520\text{--}500\text{ cm}^{-1}$ , which related to the  $\text{K}_2\text{NiF}_4$  structure. For the samples of  $\text{La}_2\text{CuO}_4$ , absorption band appeared at  $680\text{ cm}^{-1}$ . This should be confirmed to the composition with orthorhombic structure.

### 3.3.3 Scanning Electron Microscopy (SEM)

The surface morphologies of perovskite discs were examined by SEM technique. The effect of doping Sr to A-site in  $\text{Pr}_2\text{NiO}_4$ ,  $\text{La}_2\text{NiO}_4$ ,  $\text{Pr}_2\text{CuO}_4$  and  $\text{La}_2\text{CuO}_4$  was compared in the meaning of grain size, impurity and porosity. Because of the grain growth phenomenon was supported by the density result therefore density of samples were concerned by the Archimedes immersion method using water as a medium.

#### 3.3.3.1 The Surface Morphology of $\text{Pr}_2\text{NiO}_4$

The SEM micrograph of  $\text{Pr}_2\text{NiO}_4$  disc after sintered at  $1400^\circ\text{C}$  for 6 hours was shown in Figure 3.13.

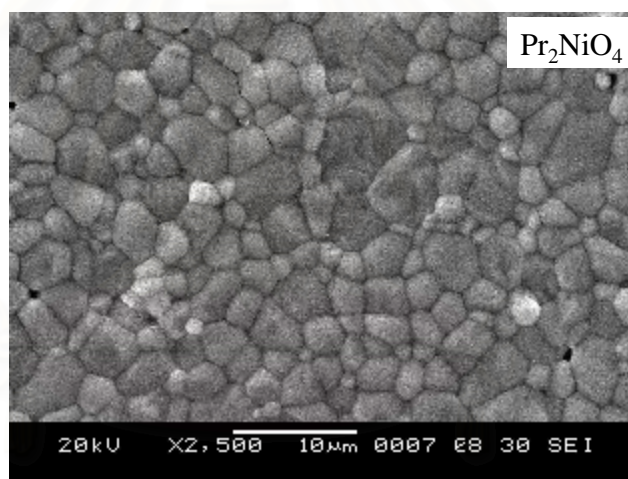


**Figure 3.13** SEM picture of  $\text{Pr}_2\text{NiO}_4$  disc sintered at  $1400^\circ\text{C}$  for 6 hours.

Figure 3.13 shows morphology of  $\text{Pr}_2\text{NiO}_4$  disc exhibited high dense disc, no impurities and homogenous phase. The  $\text{Pr}_2\text{NiO}_4$  disc had grain size around  $4\ \mu\text{m}$  and density was  $7.184\ \text{g}\cdot\text{cm}^3$  with an estimated density corresponding to 97.9 % of theoretical density calculated from XRD result.

### 3.3.3.2 The Surface Morphology of $\text{Pr}_{2-x}\text{Sr}_x\text{NiO}_4$ ( $x = 0.4, 0.6, 0.8$ and $1.0$ )

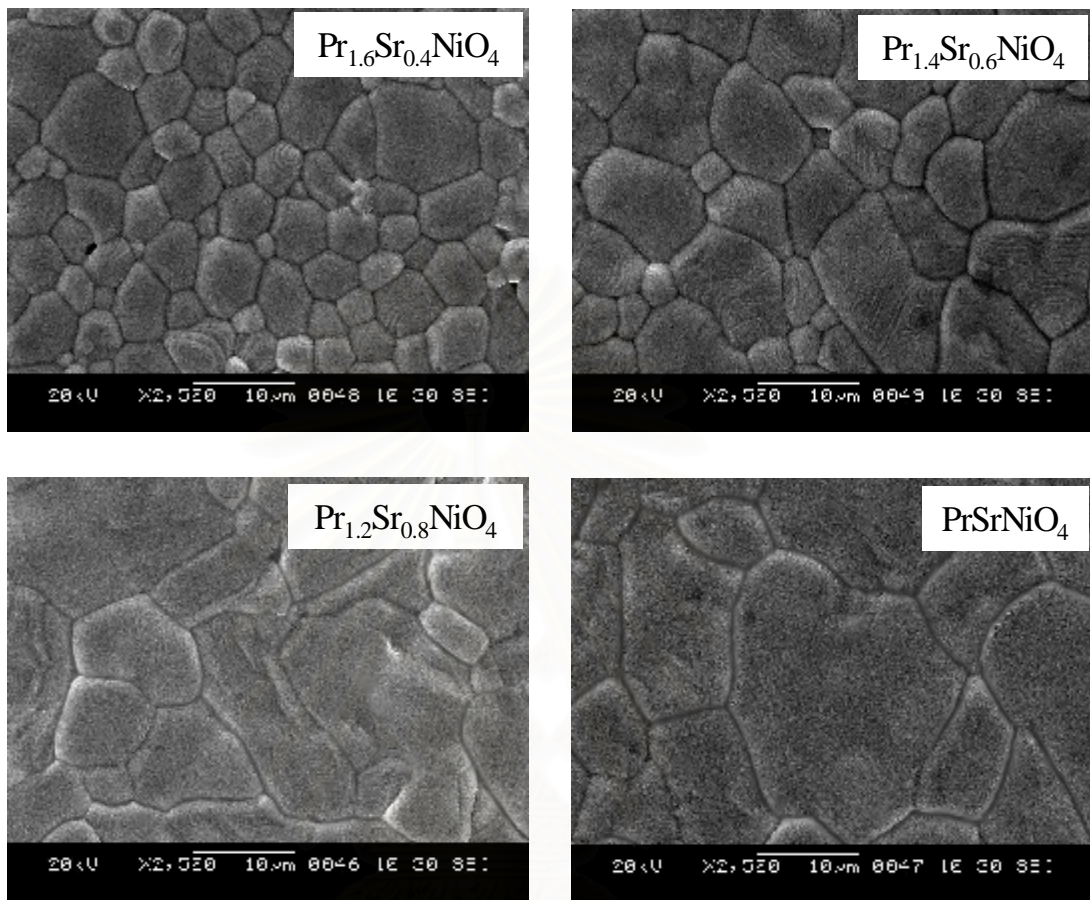


**Figure 3.14** SEM pictures of  $\text{Pr}_{2-x}\text{Sr}_x\text{NiO}_4$  ( $x = 0.4, 0.6, 0.8$  and  $1.0$ ) discs sintered at  $1400\text{ }^\circ\text{C}$  for 6 hours.

SEM micrographs shows microstructures typical for  $\text{Pr}_{2-x}\text{Sr}_x\text{NiO}_4$  ( $x = 0.4, 0.6, 0.8$  and  $1.0$ ) discs sintered at  $1400\text{ }^\circ\text{C}$  for 6 hours are presented in Figure 3.14. The average grain size was found to increase with increasing strontium content, varying in the range from approximately  $6$  to  $16\text{ }\mu\text{m}$  as summarized in Table 3.4. The partial cation substitution with Sr results in traces of a liquid phase formation at the grain boundaries of discs [54]. Doping with strontium decreases the melting points of the material, resulting in a liquid phase–assisted sintering and an enhanced grain growth according to the density.

**Table 3.4** Grain Sizes and Densities of  $\text{Pr}_{2-x}\text{Sr}_x\text{NiO}_4$  ( $x = 0, 0.4, 0.6, 0.8$  and  $1.0$ ) Discs

Composition	Grain size ( $\mu\text{m}$ )	Density ( $\text{g}\cdot\text{cm}^3$ )
$\text{Pr}_2\text{NiO}_4$	4	7.184
$\text{Pr}_{1.6}\text{Sr}_{0.4}\text{NiO}_4$	6	7.219
$\text{Pr}_{1.4}\text{Sr}_{0.6}\text{NiO}_4$	8	7.228
$\text{Pr}_{1.2}\text{Sr}_{0.8}\text{NiO}_4$	12	7.282
$\text{PrSrNiO}_4$	16	7.301

### 3.3.3.3 The Surface Morphology of $\text{La}_2\text{NiO}_4$

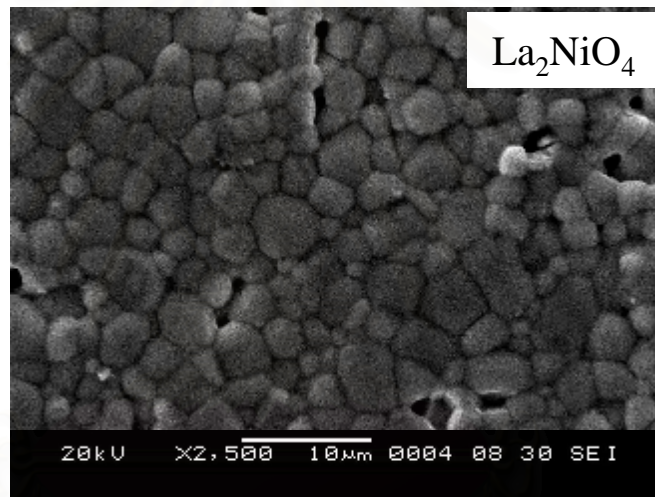


**Figure 3.15** SEM picture of  $\text{La}_2\text{NiO}_4$  disc sintered at  $1400^\circ\text{C}$  for 6 hours.

The microstructure of  $\text{La}_2\text{NiO}_4$  disc was homogeneous as shown in Figure 3.15, where some pores were observed. Moreover, the some grains size in the sintered body had growth to around  $4\ \mu\text{m}$  and density was  $6.983\ \text{g}\cdot\text{cm}^3$ .

### 3.3.3.4 The Surface Morphology of $\text{La}_{2-x}\text{Sr}_x\text{NiO}_4$ ( $x = 0.4, 0.6, 0.8$ and $1.0$ )

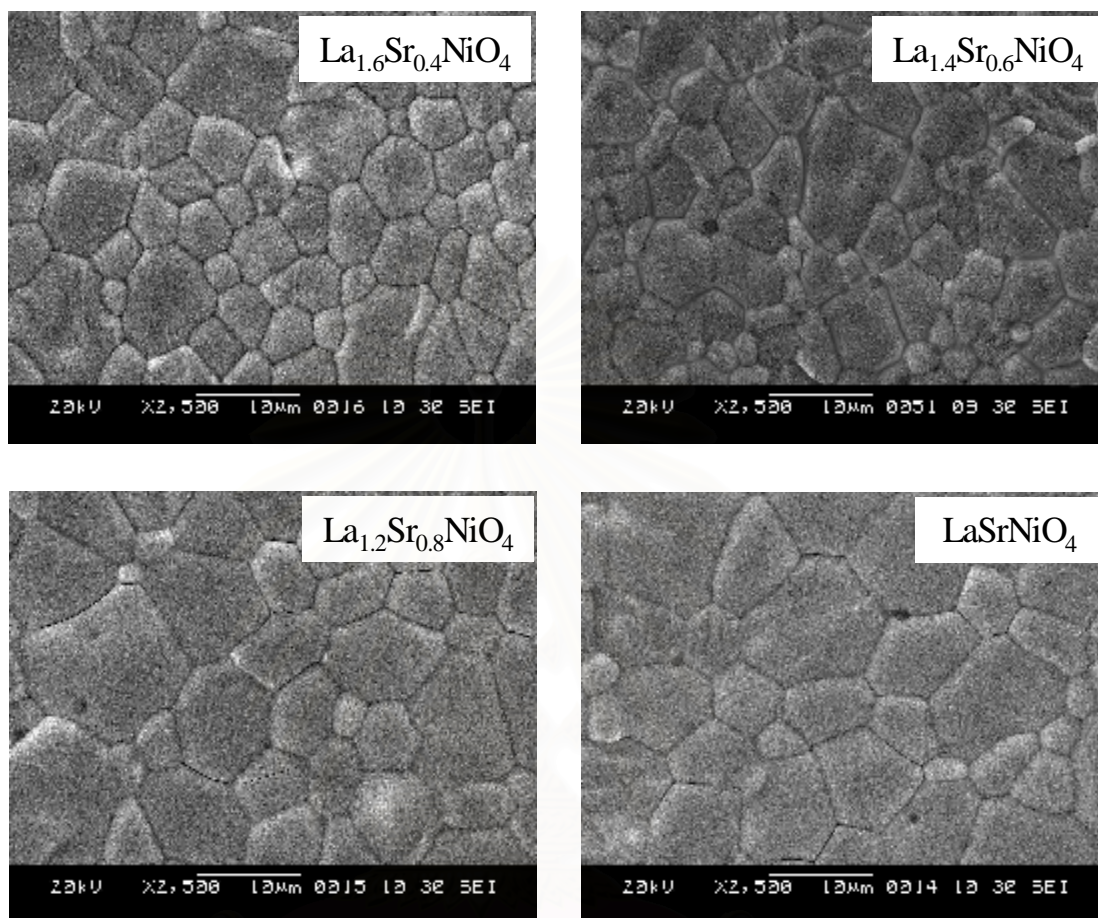


**Figure 3.16** SEM pictures of  $\text{La}_{2-x}\text{Sr}_x\text{NiO}_4$  ( $x = 0.4, 0.6, 0.8$  and  $1.0$ ) discs sintered at  $1400\text{ }^\circ\text{C}$  for 6 hours.

From Figure 3.16, SEM micrographs of  $\text{La}_{2-x}\text{Sr}_x\text{NiO}_4$  ( $x = 0.4, 0.6, 0.8$  and  $1.0$ ) discs at the same sintering temperature clearly showed that the grain size slightly increased with an increasing of Sr content. Therefore the Sr content affected on morphology of the  $\text{La}_{2-x}\text{Sr}_x\text{NiO}_4$  disc, which is similar to the  $\text{Pr}_{2-x}\text{Sr}_x\text{NiO}_4$  series. The average grain size for the  $\text{La}_{1.6}\text{Sr}_{0.4}\text{NiO}_4$ ,  $\text{La}_{1.4}\text{Sr}_{0.6}\text{NiO}_4$ ,  $\text{La}_{1.2}\text{Sr}_{0.8}\text{NiO}_4$  and  $\text{LaSrNiO}_4$  disc are about 7, 7, 8 and 9  $\mu\text{m}$ , respectively.

**Table 3.5** Grain Sizes and Densities of  $\text{La}_{2-x}\text{Sr}_x\text{NiO}_4$  ( $x = 0, 0.4, 0.6, 0.8$  and  $1.0$ ) Discs

Composition	Grain size ( $\mu\text{m}$ )	Density ( $\text{g}\cdot\text{cm}^3$ )
$\text{La}_2\text{NiO}_4$	4	6.983
$\text{La}_{1.6}\text{Sr}_{0.4}\text{NiO}_4$	7	7.152
$\text{La}_{1.4}\text{Sr}_{0.6}\text{NiO}_4$	7	7.168
$\text{La}_{1.2}\text{Sr}_{0.8}\text{NiO}_4$	8	7.257
$\text{LaSrNiO}_4$	9	7.269

The grain sizes and densities of  $\text{La}_{2-x}\text{Sr}_x\text{NiO}_4$  ( $x = 0, 0.4, 0.6, 0.8$  and  $1.0$ ) disc with various amount of Sr were listed in Table 3.5. In this series, the grain size slightly increased in the range from 7 to 9  $\mu\text{m}$ .

### 3.3.3.5 The Surface Morphology of $\text{Pr}_2\text{CuO}_4$

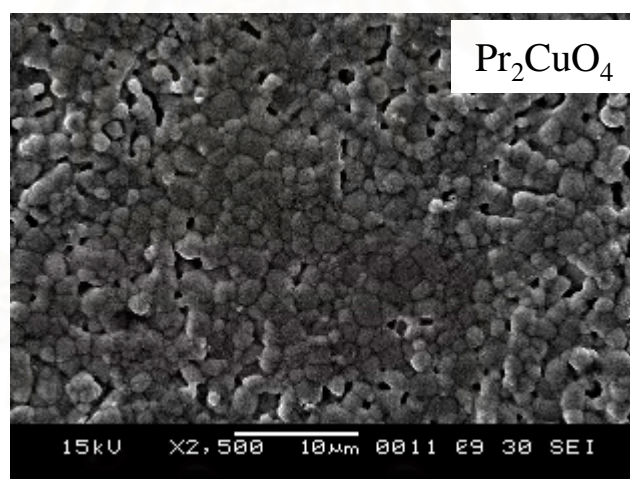


**Figure 3.17** SEM picture of  $\text{Pr}_2\text{CuO}_4$  disc sintered at  $1150^\circ\text{C}$  for 6 hours.

Figure 3.17 shows the morphology of  $\text{Pr}_2\text{CuO}_4$  disc sintered at  $1150^\circ\text{C}$  for 6 hours. The results show that the samples were fine and homogeneous. It had average grain size about 2  $\mu\text{m}$  and density was  $6.965 \text{ g}\cdot\text{cm}^3$ .



### 3.3.3.6 The Surface Morphology of $\text{Pr}_{2-x}\text{Sr}_x\text{CuO}_4$ ( $x = 0.4, 0.6, 0.8$ and $1.0$ )

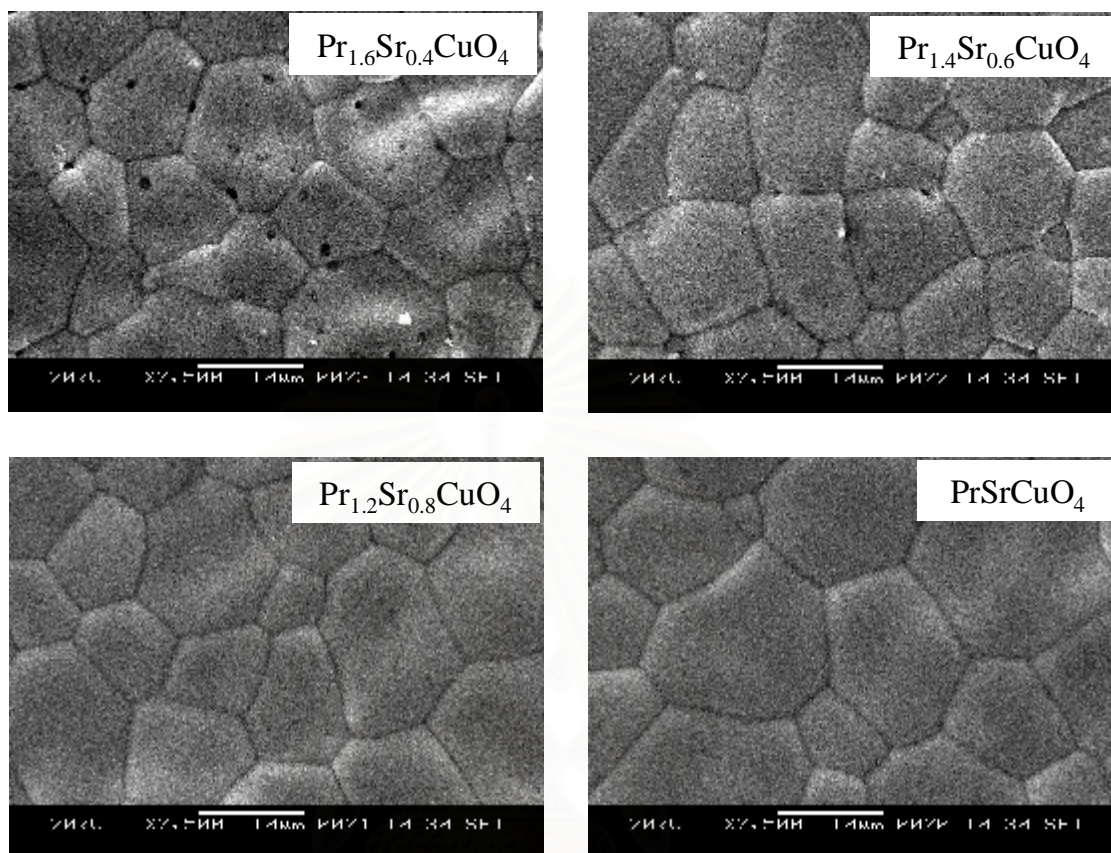


**Figure 3.18** SEM pictures of  $\text{Pr}_{2-x}\text{Sr}_x\text{CuO}_4$  ( $x = 0.4, 0.6, 0.8$  and  $1.0$ ) discs sintered at  $1150\text{ }^\circ\text{C}$  for 6 hours.

Surface micrographs of various Sr-doped  $\text{Pr}_{2-x}\text{Sr}_x\text{CuO}_4$  ( $x = 0.4, 0.6, 0.8$  and  $1.0$ ) with sintering temperatures of  $1150\text{ }^\circ\text{C}$  for 6 hours were shown in Figure 3.18. The sintered temperature to obtain dense  $\text{Pr}_{2-x}\text{Sr}_x\text{CuO}_4$  is lower than that of  $\text{Pr}_{2-x}\text{Sr}_x\text{NiO}_4$ . It was noticed that the grain sizes and densities of cuprates increased with the increasing of  $\text{Sr}^{2+}$  content, as summarized in Table 3.6. The morphology of the compounds were dense and similar to that of nickelates while the sintering temperature was lower. It is possible that oxide with Cu can affect the decreasing of the melting point of  $\text{Pr}_{2-x}\text{Sr}_x\text{CuO}_4$ , so the fusion of grain easily occurred. A few of small black particles were observed on the surface of  $\text{Pr}_{1.6}\text{Sr}_{0.4}\text{CuO}_4$  and  $\text{Pr}_{1.4}\text{Sr}_{0.6}\text{CuO}_4$  and disappeared when the amount of Sr doping increased. The unidentified impurity was not detected in the XRD patterns.

**Table 3.6** Grain Sizes and Densities of  $\text{Pr}_{2-x}\text{Sr}_x\text{CuO}_4$  ( $x = 0, 0.4, 0.6, 0.8$  and  $1.0$ ) Discs

Composition	Grain size ( $\mu\text{m}$ )	Density ( $\text{g}\cdot\text{cm}^3$ )
$\text{Pr}_2\text{CuO}_4$	2	6.965
$\text{Pr}_{1.6}\text{Sr}_{0.4}\text{CuO}_4$	10	7.09
$\text{Pr}_{1.4}\text{Sr}_{0.6}\text{CuO}_4$	11	7.125
$\text{Pr}_{1.2}\text{Sr}_{0.8}\text{CuO}_4$	12	7.176
$\text{PrSrCuO}_4$	14	7.254

### 3.3.3.7 The Surface Morphology of $\text{La}_2\text{CuO}_4$

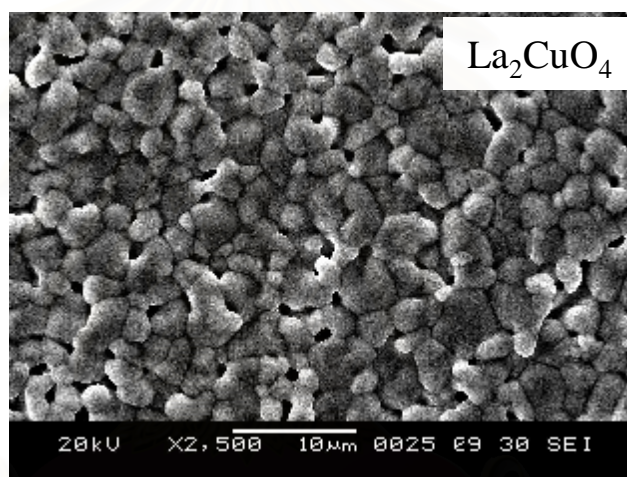


**Figure 3.19** SEM picture of  $\text{La}_2\text{CuO}_4$  disc sintered at  $1150^\circ\text{C}$  for 6 hours.

The SEM micrograph of  $\text{La}_2\text{CuO}_4$  disc sintered at  $1150^\circ\text{C}$  for 6 hours was shown in Figure 3.19. The small grain size ( $4 \mu\text{m}$ ) and some pores were observed with density around  $6.944 \text{ g}\cdot\text{cm}^3$ .

### 3.3.3.8 The Surface Morphology of $\text{La}_{2-x}\text{Sr}_x\text{CuO}_4$ ( $x = 0.4, 0.6, 0.8$ and $1.0$ )

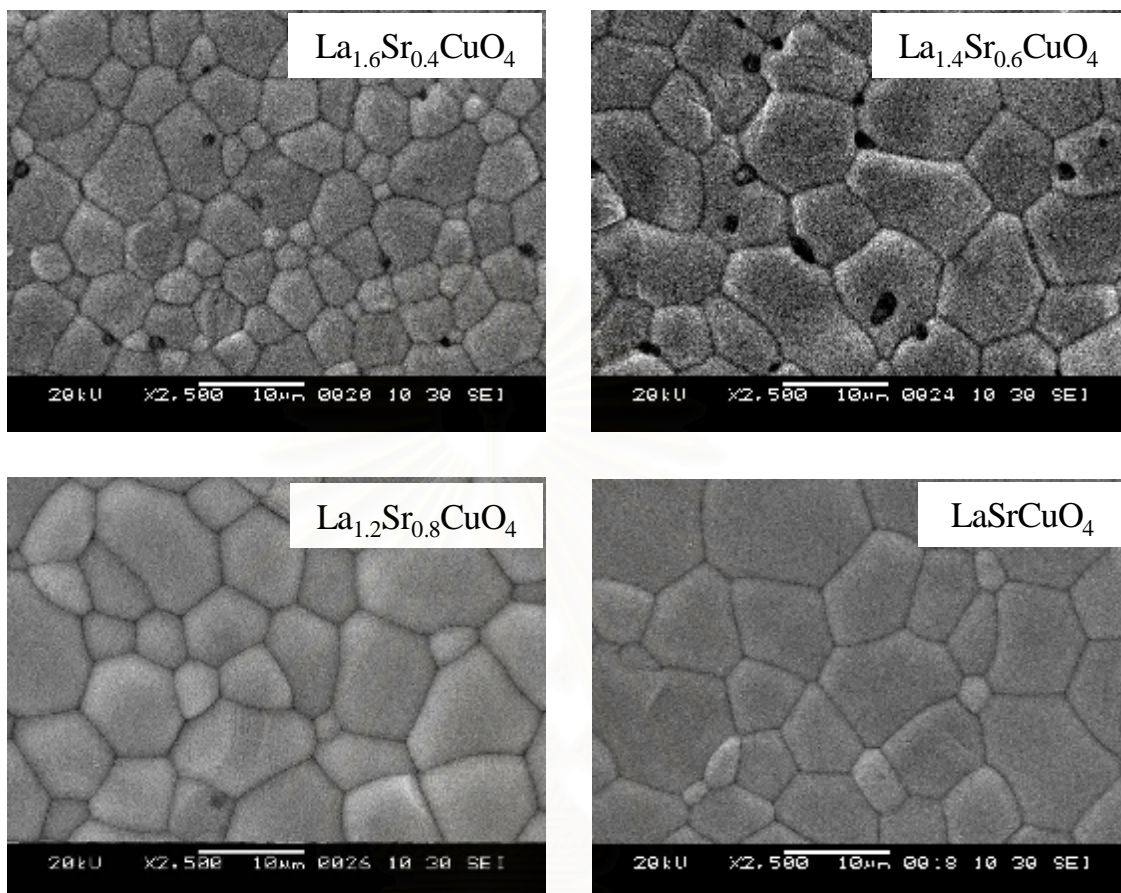


**Figure 3.20** SEM pictures of  $\text{La}_{2-x}\text{Sr}_x\text{CuO}_4$  ( $x = 0.4, 0.6, 0.8$  and  $1.0$ ) discs sintered at  $1150\text{ }^\circ\text{C}$  for 6 hours.

Figure 3.20 shows the SEM micrographs of high densification of the  $\text{La}_{2-x}\text{Sr}_x\text{CuO}_4$  ( $x = 0.4, 0.6, 0.8$  and  $1.0$ ) disc sintered at  $1150\text{ }^\circ\text{C}$  for 6 hours. The microstructural feature of the  $\text{La}_{2-x}\text{Sr}_x\text{CuO}_4$  is generally similar to that of  $\text{Pr}_{2-x}\text{Sr}_x\text{CuO}_4$ . Moreover, it was found that the  $\text{La}_{1.6}\text{Sr}_{0.4}\text{CuO}_4$  and  $\text{La}_{1.4}\text{Sr}_{0.6}\text{CuO}_4$  exhibit some black point as impurities and it was disappeared when increasing Sr content. The grain sizes in the sintered samples have grown to  $10\text{ }\mu\text{m}$  and the densities were presented in Table 3.7.

**Table 3.7** Grain Sizes and Densities of  $\text{La}_{2-x}\text{Sr}_x\text{CuO}_4$  ( $x = 0, 0.4, 0.6, 0.8$  and  $1.0$ ) Discs

Composition	Grain size ( $\mu\text{m}$ )	Density ( $\text{g}\cdot\text{cm}^3$ )
$\text{La}_2\text{CuO}_4$	4	6.944
$\text{La}_{1.6}\text{Sr}_{0.4}\text{CuO}_4$	7	7.228
$\text{La}_{1.4}\text{Sr}_{0.6}\text{CuO}_4$	9	7.245
$\text{La}_{1.2}\text{Sr}_{0.8}\text{CuO}_4$	9	7.276
$\text{LaSrCuO}_4$	10	7.284

From the SEM result, it can be concluded that the grain size of perovskite disc increased with the increasing amount of Sr. The particle of cuprates was fused into large grain at lower temperature than that of nickelates. Because of the appearance of Cu in the structure, resulting in a reduced melting point of materials.

### 3.3.4 Temperature–Program Desorption of Oxygen ( $\text{O}_2$ –TPD)

In the oxygen temperature program desorption ( $\text{O}_2$ –TPD) process, oxygen was exchanged by chemisorption mechanism. The ion participated not only on surface but also inside the perovskite.

Generally, the  $\text{O}_2$ –TPD profiles plotted from the perovskite-like mixed oxides contain three kinds of oxygen species. The desorption peak appeared at  $T < 500$  °C is ascribed to the oxygen chemically adsorbed on the surface (denoted as:  $\alpha$  oxygen); the desorption peak appeared at  $500 < T < 800$  °C is ascribed to the oxygen chemically adsorbed on the oxygen vacancy (denoted as:  $\beta$  oxygen); and the desorption peak appeared at  $T > 800$  °C is ascribed to the oxygen escaped from the lattice (denoted as:  $\gamma$  oxygen) [36].

The crystal structure of  $\text{Ln}_2\text{MO}_4$  is built of alternating rock–salt and perovskite layers and can accommodate a significant oxygen excess. The extra  $\text{O}^{2-}$  anions, charge compensated by electron holes localized on  $\text{M}^{2+}$  cations, occupy interstitial position in the LnO layers. The oxide ion transport occurs via a complex mechanism involving diffusion of interstitial ions in the rock–salt layers and oxygen vacancies in the perovskite planes. Doping with  $\text{Sr}^{2+}$  decreases oxygen excess and ionic conduction. Generally, when the A ion is partially substituted with an ion of lower oxidation state, a charge compensation is required to achieve

electroneutrality. This can either be achieved by formation of oxygen vacancies or by shift of the B metal toward higher valences (e.g.,  $\text{Ni}^{2+} \rightarrow \text{Ni}^{3+}$ ) [55].

### 3.3.4.1 The Oxygen Desorption of $\text{Pr}_{2-x}\text{Sr}_x\text{NiO}_4$ ( $x = 0.4, 0.6, 0.8$ and $1.0$ )

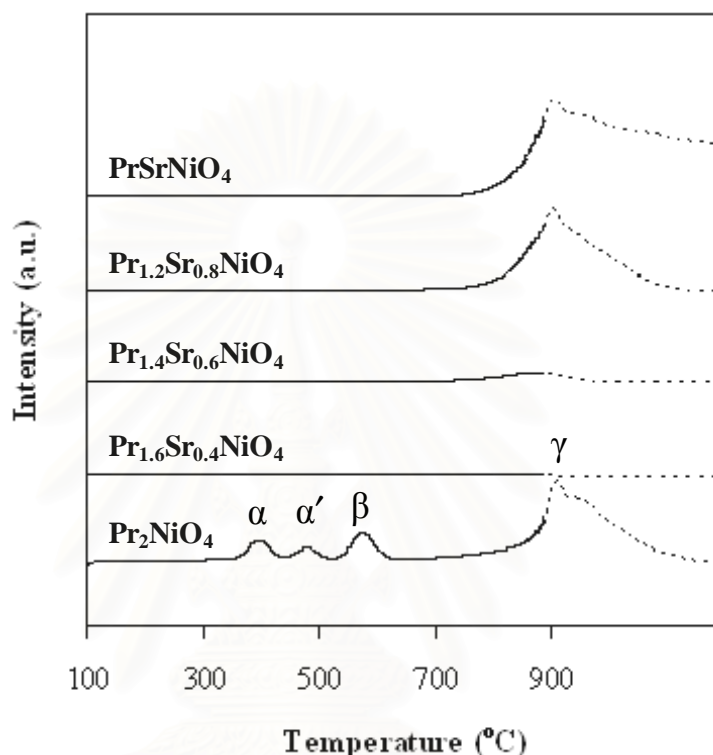


**Figure 3.21**  $\text{O}_2$ -TPD profiles of  $\text{Pr}_{2-x}\text{Sr}_x\text{NiO}_4$  ( $x = 0, 0.4, 0.6, 0.8$  and  $1.0$ )

The  $\text{O}_2$ -TPD profiles were obtained over  $\text{Pr}_{2-x}\text{Sr}_x\text{NiO}_4$  ( $x = 0, 0.4, 0.6, 0.8$  and  $1.0$ ), as presented in Figure 3.21. For  $\text{Pr}_2\text{NiO}_4$ , there exists four desorption peaks of oxygen ( $\alpha$ ,  $\alpha'$ ,  $\beta$ , and  $\gamma$ ), respectively. For  $\alpha$  and  $\alpha'$  peaks (at  $\sim 400$  and  $480$  °C), it is difficult for these oxygen peaks to distinguish. The results could be explained as that there are different states of oxygen ( $\text{O}^-$  or  $\text{O}^{2-}$ ) on the oxide surface [56]. The  $\beta$  peak ( $\sim 580$  °C) corresponds to the desorption of the oxygen chemically adsorbed on oxygen vacancies ( $\text{V}_\text{o}$ ), namely, the oxygen that is released by reduction of  $\text{Ni}^{3+}$  according to the following reaction, as shown in equation 3.3 [57], and  $\gamma$  peak appeared at  $T \sim 900$  °C is ascribed to the oxygen escaped from the lattice.



When  $\text{Pr}^{3+}$  are substituted with  $\text{Sr}^{2+}$  cations. For  $x = 0.4$ , no any desorption peak appeared. It is suggest that doping with 0.4 mole of  $\text{Sr}^{2+}$  cause a large decrease of oxygen excess and ionic conduction. However, for  $x \geq 0.6$ , the  $\gamma$  peak area was observed and increased with increasing of  $x$ , implied that mobile lattice oxygen also increased. It is mentioned elsewhere [58] that perovskite-like structure  $\text{Ln}_2\text{MO}_4$  tend to accommodate excess oxygen, while those with high strontium contents are slightly oxygen deficient. The greater value of  $x$ , the greater the proportion of  $\text{Ni}^{2+}$  which must be oxidized to  $\text{Ni}^{3+}$  in order to preserve overall charge neutrality. The oxygen desorption will increased when the amount of  $\text{Sr}^{2+}$  increased which is consistent with the obtained result.

The amount of oxygen desorption determined from the peak area was illustrated in Table 3.8.

**Table 3.8** Amount of oxygen desorbed for  $\text{Pr}_{2-x}\text{Sr}_x\text{NiO}_4$  ( $x = 0, 0.4, 0.6, 0.8, 1.0$ )

Compositions	Oxygen desorption (mmol/g)				Total oxygen desorption
	$\alpha$	$\alpha'$	$\beta$	$\gamma$	
$\text{Pr}_2\text{NiO}_4$	0.0334	0.0196	0.0542	0.5073	0.6145
$\text{Pr}_{1.6}\text{Sr}_{0.4}\text{NiO}_4$	–	–	–	–	–
$\text{Pr}_{1.4}\text{Sr}_{0.6}\text{NiO}_4$	–	–	–	0.0355	0.0355
$\text{Pr}_{1.2}\text{Sr}_{0.8}\text{NiO}_4$	–	–	–	0.3793	0.3793
$\text{PrSrNiO}_4$	–	–	–	0.6508	0.6508

The order of the mobility of lattice oxygen in various  $\text{Sr}^{2+}$  content decreased in the following order:  $\text{PrSrNiO}_4 > \text{Pr}_2\text{NiO}_4 > \text{Pr}_{1.2}\text{Sr}_{0.8}\text{NiO}_4 \gg \text{Pr}_{1.4}\text{Sr}_{0.6}\text{NiO}_4 > \text{Pr}_{1.6}\text{Sr}_{0.4}\text{NiO}_4$ .

### 3.3.4.2 The Oxygen Desorption of $\text{La}_{2-x}\text{Sr}_x\text{NiO}_4$ ( $x = 0.4, 0.6, 0.8$ and $1.0$ )

The  $\text{O}_2$ -TPD profiles of the  $\text{La}_{2-x}\text{Sr}_x\text{NiO}_4$  ( $x = 0, 0.4, 0.6, 0.8$  and  $1.0$ ) were shown in Figure 3.22. The oxygen desorption peak described to oxygen adsorb on the surface of  $\text{La}_2\text{NiO}_4$  was observed around  $400^\circ\text{C}$ . It was found that  $\alpha$  peak disappeared when replaced  $\text{La}^{3+}$  with  $\text{Sr}^{2+}$  at  $x = 0.4$  and  $0.6$ . On the contrary,  $\gamma$  peak appeared in the thermogram and increased with increasing of  $\text{Sr}^{2+}$ . Actually, the desorption peak of  $\gamma$  oxygen depended on many factors. In addition to the structure and the oxygen deficiency, the oxidability of B-site cation also has large effect on the desorption of  $\gamma$  oxygen.

The amount of total oxygen desorbed of  $\text{La}_{2-x}\text{Sr}_x\text{NiO}_4$  ( $x = 0, 0.4, 0.6, 0.8$  and  $1.0$ ) compounds were shown in Table 3.9.

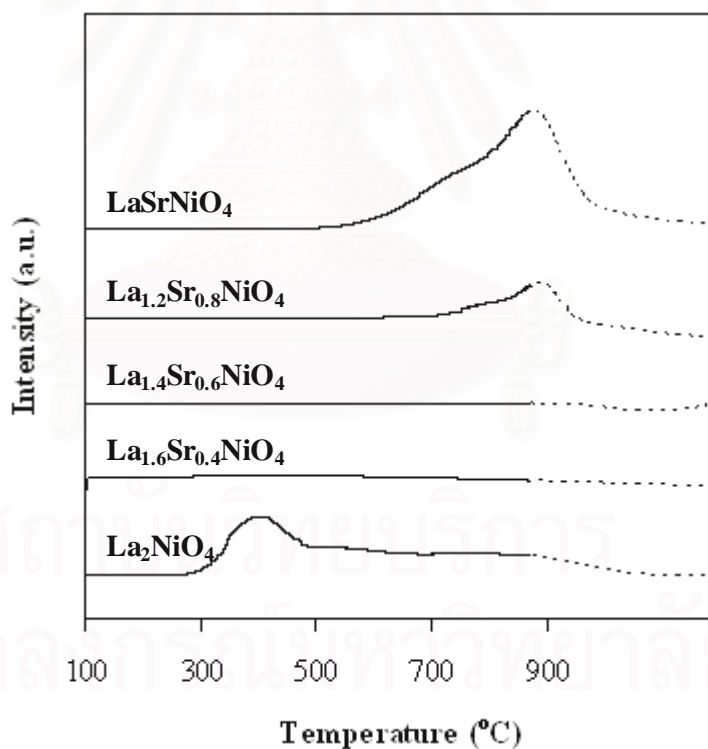


**Figure 3.22**  $\text{O}_2$ -TPD profiles of  $\text{La}_{2-x}\text{Sr}_x\text{NiO}_4$  ( $x = 0, 0.4, 0.6, 0.8$  and  $1.0$ )

**Table 3.9** Amount of oxygen desorbed for  $\text{La}_{2-x}\text{Sr}_x\text{NiO}_4$  ( $x = 0, 0.4, 0.6, 0.8, 1.0$ )

Compositions	Total oxygen desorption (mmol/g)
$\text{La}_2\text{NiO}_4$	0.1342
$\text{La}_{1.6}\text{Sr}_{0.4}\text{NiO}_4$	–
$\text{La}_{1.4}\text{Sr}_{0.6}\text{NiO}_4$	–
$\text{La}_{1.2}\text{Sr}_{0.8}\text{NiO}_4$	0.0145
$\text{LaSrNiO}_4$	0.1242

Comparing the desorption temperature corresponding to the largest desorption amounts of  $\text{O}_2$  could be  $\text{La}_2\text{NiO}_4 > \text{LaSrNiO}_4 > \text{La}_{1.2}\text{Sr}_{0.8}\text{NiO}_4$ .

### 3.3.4.3 The Oxygen Desorption of $\text{Pr}_{2-x}\text{Sr}_x\text{CuO}_4$ ( $x = 0.4, 0.6, 0.8$ and $1.0$ )

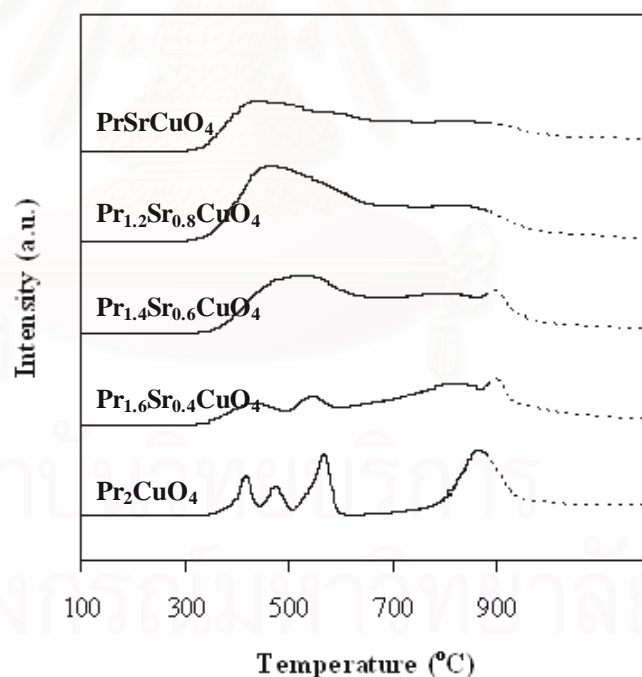
**Figure 3.23**  $\text{O}_2$ -TPD profiles of  $\text{Pr}_{2-x}\text{Sr}_x\text{CuO}_4$  ( $x = 0, 0.4, 0.6, 0.8$  and  $1.0$ )

Figure 3.23 shows the  $\text{O}_2$ -TPD profiles of the  $\text{Pr}_{2-x}\text{Sr}_x\text{CuO}_4$ . For  $\text{Pr}_2\text{CuO}_4$ , the attributions of desorption peaks are the same as that for  $\text{Pr}_2\text{NiO}_4$ . With increasing Sr content, the spectra presented two or three desorption peak within the 300–900 °C temperature range. The amount of total oxygen desorbed of



$\text{Pr}_{2-x}\text{Sr}_x\text{CuO}_4$  ( $x = 0, 0.4, 0.6, 0.8$  and  $1.0$ ) compounds are shown in Table 3.10. It is observed that the amount of an oxygen mobility in the samples decreased in the order of  $\text{Pr}_{1.2}\text{Sr}_{0.8}\text{CuO}_4 > \text{Pr}_{1.4}\text{Sr}_{0.6}\text{CuO}_4 > \text{PrSrCuO}_4 > \text{Pr}_{1.6}\text{Sr}_{0.4}\text{CuO}_4 > \text{Pr}_2\text{CuO}_4$ . It may be suggested that the type of oxygen vacancy in  $\text{Pr}_2\text{CuO}_4$  is different from that in  $\text{Pr}_{2-x}\text{Sr}_x\text{CuO}_4$  ( $x = 0.4, 0.6, 0.8$  and  $1.0$ ). The oxygen vacancies produced by the substitution of Pr with Sr in  $\text{PrSrCuO}_4$  seem to be disordered.

**Table 3.10** Amount of oxygen desorbed for  $\text{Pr}_{2-x}\text{Sr}_x\text{CuO}_4$  ( $x = 0, 0.4, 0.6, 0.8, 1.0$ )

Compositions	Oxygen desorption (mmol/g)				Total oxygen desorption
	$\alpha$	$\alpha'$	$\beta$	$\gamma$	
$\text{Pr}_2\text{CuO}_4$	0.02093	0.01563	0.03774	0.13177	0.2061
$\text{Pr}_{1.6}\text{Sr}_{0.4}\text{CuO}_4$	0.2199				0.2199
$\text{Pr}_{1.4}\text{Sr}_{0.6}\text{CuO}_4$	0.3209				0.3209
$\text{Pr}_{1.2}\text{Sr}_{0.8}\text{CuO}_4$	0.3744				0.3744
$\text{PrSrCuO}_4$	0.3116				0.3116

#### 3.3.4.4 The Oxygen Desorption of $\text{La}_{2-x}\text{Sr}_x\text{CuO}_4$ ( $x = 0.4, 0.6, 0.8$ and $1.0$ )

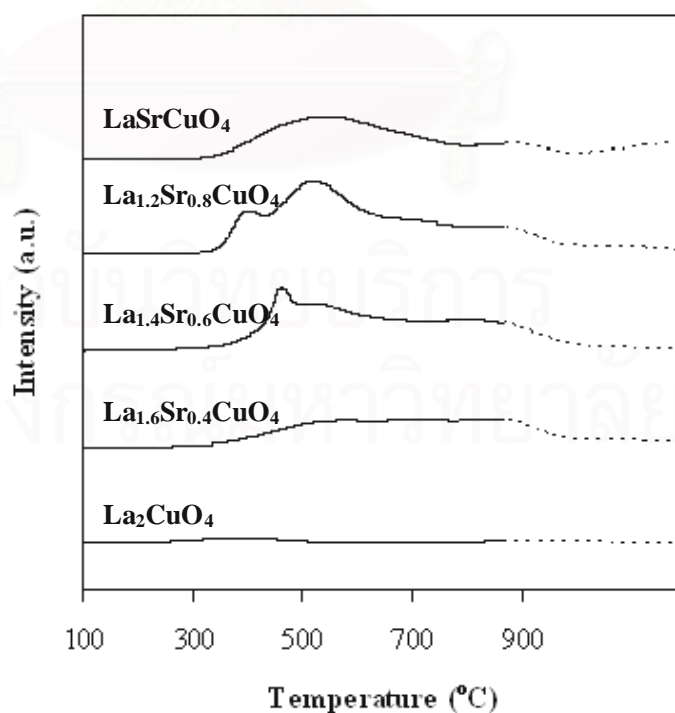


**Figure 3.24**  $\text{O}_2$ -TPD profiles of  $\text{La}_{2-x}\text{Sr}_x\text{CuO}_4$  ( $x = 0, 0.4, 0.6, 0.8$  and  $1.0$ )

O<sub>2</sub>-TPD results indicated that the introduction of Sr at A-site had great influence on the oxygen desorption. In Figure 3.24, with the increase of x (x = 0.0–0.8), the desorption peak area increases, except LaSrCuO<sub>4</sub>, implied that oxygen vacancies and mobile lattice oxygen also increases.

**Table 3.11** Amount of oxygen desorbed for La<sub>2-x</sub>Sr<sub>x</sub>CuO<sub>4</sub> (x = 0, 0.4, 0.6, 0.8, 1.0)

Compositions	Total oxygen desorption (mmol/g)
La <sub>2</sub> CuO <sub>4</sub>	0.0150
La <sub>1.6</sub> Sr <sub>0.4</sub> CuO <sub>4</sub>	0.1738
La <sub>1.4</sub> Sr <sub>0.6</sub> CuO <sub>4</sub>	0.2616
La <sub>1.2</sub> Sr <sub>0.8</sub> CuO <sub>4</sub>	0.2956
LaSrCuO <sub>4</sub>	0.2146

Table 3.11 lists amount of oxygen desorption for La<sub>2-x</sub>Sr<sub>x</sub>CuO<sub>4</sub> (x = 0, 0.4, 0.6, 0.8, 1.0) with various Sr content. Amount of oxygen desorption produced by increasing Sr, seem to be disordered. The oxygen mobility corresponding to the oxygen desorption amount was in order of La<sub>1.2</sub>Sr<sub>0.8</sub>CuO<sub>4</sub> > La<sub>1.4</sub>Sr<sub>0.6</sub>CuO<sub>4</sub> > LaSrCuO<sub>4</sub> > La<sub>1.6</sub>Sr<sub>0.4</sub>CuO<sub>4</sub> > La<sub>2</sub>CuO<sub>4</sub>.

For Sr-doped Pr<sub>2</sub>CuO<sub>4</sub> and La<sub>2</sub>CuO<sub>4</sub>, the highest oxygen desorption was obtained when amount of Sr content is 0.8.

### 3.3.5 Electrical Conductivity Measurement

The total electrical conductivity of the obtained oxides as a function of temperature was measured by the DC 4-probes method. The measured value of total conductivity includes electronic and ionic contributions due to the presence of charge carriers and oxygen vacancies, respectively. However, ionic conductivity in the type of perovskite oxides is known to be small in comparison with the overall conductivity [59]. Therefore, the experimental values of the electrical conductivity are assumed to correspond to the electronic conductivity alone.

The electrical conductivity is strongly dependent on temperature. For metals, electrical conductivity decreases with increasing temperature, whereas in semiconductors, electrical conductivity increases with increasing temperature.

In this section, the effects of Sr amount in A-site on electrical conductivity of  $\text{Ln}_{2-x}\text{Sr}_x\text{MO}_4$  were studied. The electrical conductivity ( $\sigma$ ) of sintered ceramics was examined in air and the temperature in the range of room temperature to 800 °C.

### 3.3.5.1 The Electrical Conductivity of $\text{Pr}_{2-x}\text{Sr}_x\text{NiO}_4$ ( $x = 0, 0.4, 0.6, 0.8$ and $1.0$ )

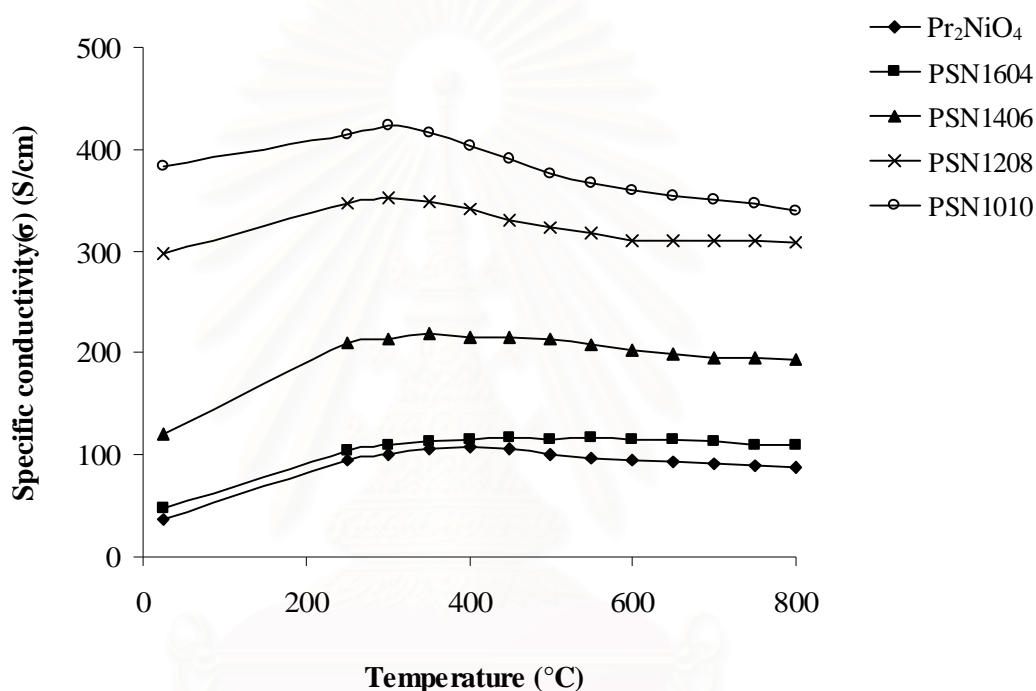


**Figure 3.25** Electrical conductivity ( $\sigma$ ) of  $\text{Pr}_{2-x}\text{Sr}_x\text{NiO}_4$  ( $x = 0, 0.4, 0.6, 0.8$  and  $1.0$ ) as a function of measuring temperature.

**Table 3.12** The specific conductivity of  $\text{Pr}_{2-x}\text{Sr}_x\text{NiO}_4$  ( $x = 0, 0.4, 0.6, 0.8$  and  $1.0$ )

Sample	Specific conductivity, $\sigma$ (S/cm)						$\sigma_{\max}$ (T, °C)
	300 °C	400 °C	500 °C	600 °C	700 °C	800 °C	
$\text{Pr}_2\text{NiO}_4$	100.8	107.4	100.8	95.0	92.1	87.8	107.4 (400)
$\text{Pr}_{1.6}\text{Sr}_{0.4}\text{NiO}_4$	110.4	115.5	115.8	115.8	113.2	109.5	117.5 (550)
$\text{Pr}_{1.4}\text{Sr}_{0.6}\text{NiO}_4$	214.1	216.1	214.0	203.2	195.2	193.6	218.9 (350)
$\text{Pr}_{1.2}\text{Sr}_{0.8}\text{NiO}_4$	352.8	340.8	323.2	310.4	309.3	309.0	352.8 (300)
$\text{PrSrNiO}_4$	423.5	403.1	375.1	359.9	351.1	340.0	423.5 (300)

From Figure 3.25, the electrical conductivity of  $\text{Pr}_2\text{NiO}_4$  and Sr-doped  $\text{Pr}_2\text{NiO}_4$  exhibit a change in the conduction region from semiconductor-like below  $400\text{ }^\circ\text{C}$ , followed by metal-like behavior at high temperature. However, the conductivity strongly depended on the Sr content when Sr content increase, the conductivity increase. It is evident that conductivity of  $\text{PrSrNiO}_4$  had maximum value of  $423.5\text{ S/cm}$  at  $300\text{ }^\circ\text{C}$  which was about 4 times higher than that of undoped  $\text{Pr}_2\text{NiO}_4$  ( $107.4\text{ S/cm}$  at  $400^\circ\text{C}$ ), as summarized in Table 3.12. Then the obtained data were presented as Arrhenius plots (see Figure 3.26), from the conductivity relation:

$$\sigma = \sigma_0 \exp(-E_a/RT) \quad (3.3)$$

where  $\sigma_0$  = material constant

$E_a$  = activation energy

$R$  = gas constant

$T$  = absolute temperature

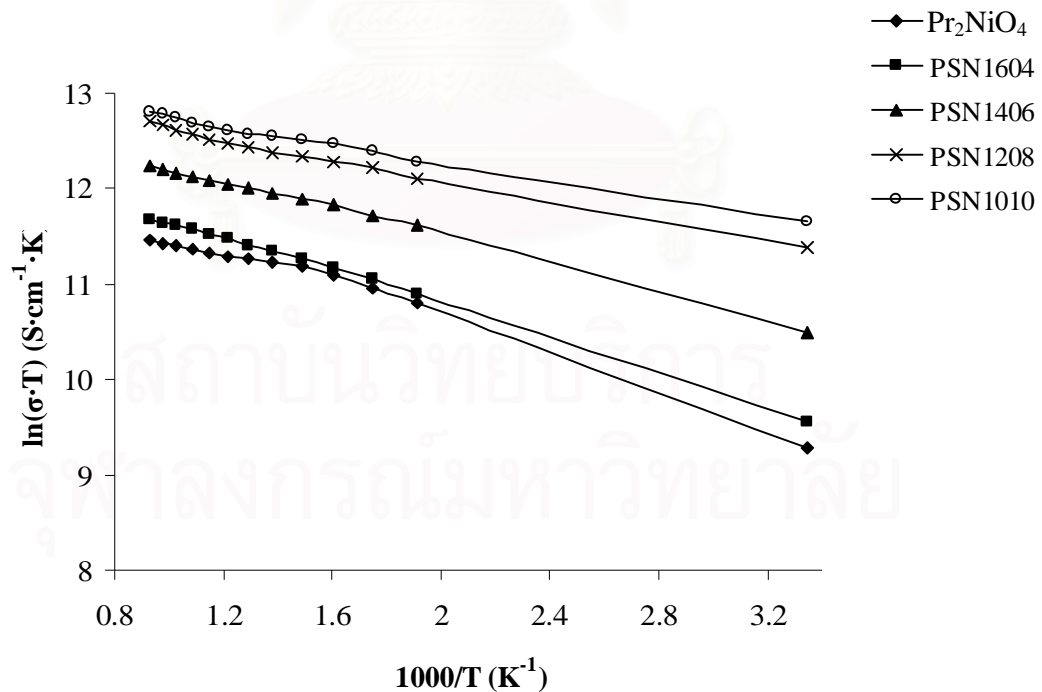


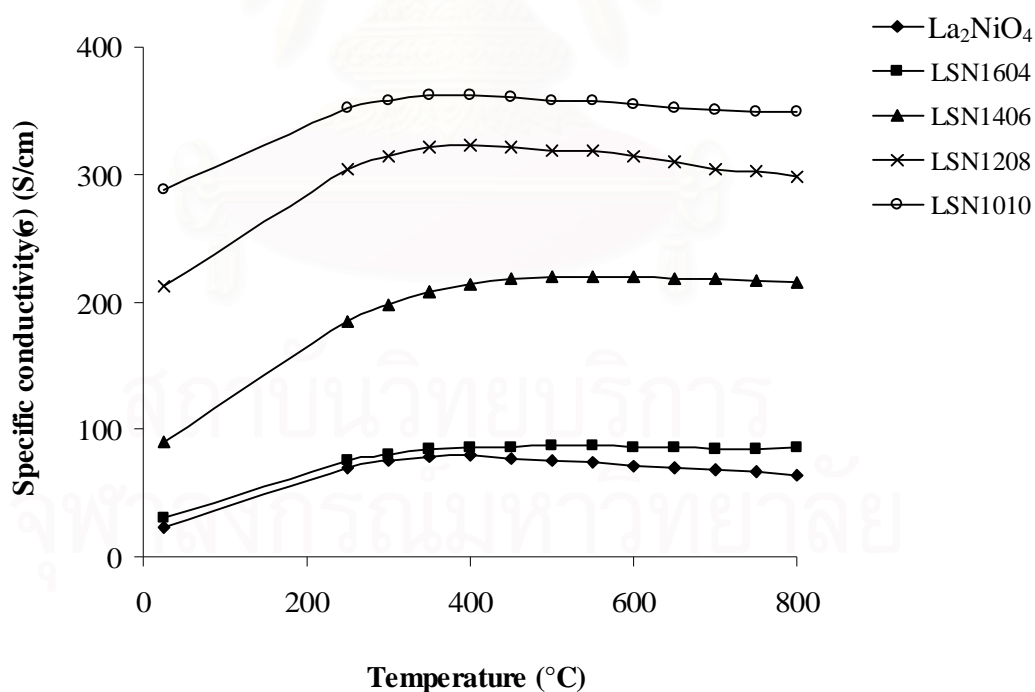
**Figure 3.26** Arrhenius plots of  $\text{Pr}_{2-x}\text{Sr}_x\text{NiO}_4$  ( $x = 0, 0.4, 0.6, 0.8$  and  $1.0$ )

The activation energy ( $E_a$ ) was calculated from the slope of  $\log(\sigma \cdot T)$  versus  $1000/T$  plots were shown in Table 3.13. The activation energies of  $\text{Pr}_{2-x}\text{Sr}_x\text{NiO}_4$  ( $x = 0, 0.4, 0.6, 0.8$  and  $1.0$ ) specimens were decreased with the increasing of Sr.

**Table 3.13** Activation energy of  $\text{Pr}_{2-x}\text{Sr}_x\text{NiO}_4$  ( $x = 0, 0.4, 0.6, 0.8$  and  $1.0$ )

Composition	$E_a$ (kJ/mol)
$\text{Pr}_2\text{NiO}_4$	8.10
$\text{Pr}_{1.6}\text{Sr}_{0.4}\text{NiO}_4$	7.26
$\text{Pr}_{1.4}\text{Sr}_{0.6}\text{NiO}_4$	5.94
$\text{Pr}_{1.2}\text{Sr}_{0.8}\text{NiO}_4$	3.44
$\text{PrSrNiO}_4$	3.13

### 3.3.5.2 The Electrical Conductivity of $\text{La}_{2-x}\text{Sr}_x\text{NiO}_4$ ( $x = 0, 0.4, 0.6, 0.8$ and $1.0$ )



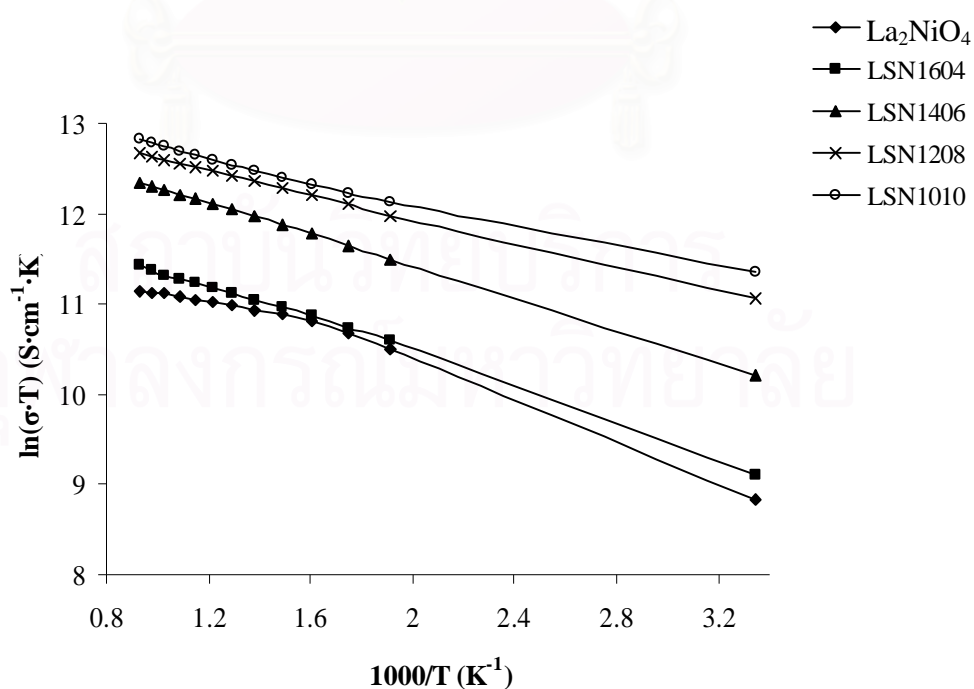
**Figure 3.27** Electrical conductivity ( $\sigma$ ) of  $\text{La}_{2-x}\text{Sr}_x\text{NiO}_4$  ( $x = 0, 0.4, 0.6, 0.8$  and  $1.0$ ) as a function of measuring temperature.

Figure 3.27 shows the electrical conductivity of undoped and doped  $\text{La}_2\text{NiO}_4$  which is similar to the behavior of  $\text{Pr}_2\text{NiO}_4$ . The electrical conductivity of all compounds shows semi-conductor type in air in the temperature from room temperature to 400 °C and metallic-type at high temperature. The Sr substitution concentration affects the electrical conductivity. The conductivity was enhanced with the increase in substitution concentration  $x$ . In this series,  $\text{LaSrNiO}_4$  shows maximum value of 361.6 S/cm which was about 4.5 times higher than that of  $\text{La}_2\text{NiO}_4$  (80.1 S/cm at 400°C), as presented in Table 3.14.

**Table 3.14** The specific conductivity of  $\text{La}_{2-x}\text{Sr}_x\text{NiO}_4$  ( $x = 0, 0.4, 0.6, 0.8$  and  $1.0$ )

Sample	Specific conductivity, $\sigma$ (S/cm)						$\sigma_{\text{max}}$ (T, °C)
	300 °C	400 °C	500 °C	600 °C	700 °C	800 °C	
$\text{La}_2\text{NiO}_4$	75.5	80.1	76.0	71.9	68.9	64.7	80.1 (400)
$\text{La}_{1.6}\text{Sr}_{0.4}\text{NiO}_4$	80.5	85.6	86.8	86.4	84.9	85.3	86.8 (500)
$\text{La}_{1.4}\text{Sr}_{0.6}\text{NiO}_4$	198.4	214.0	219.6	219.9	217.7	214.6	220.0 (550)
$\text{La}_{1.2}\text{Sr}_{0.8}\text{NiO}_4$	314.0	322.6	318.2	314.7	304.3	298.6	322.6 (400)
$\text{LaSrNiO}_4$	357.7	316.6	358.1	355.1	351.0	349.1	361.6 (400)

The logarithm of electrical conductivity versus reciprocal temperature in air is shown in Figure 3.28



**Figure 3.28** Arrhenius plots of  $\text{La}_{2-x}\text{Sr}_x\text{NiO}_4$  ( $x = 0, 0.4, 0.6, 0.8$  and  $1.0$ )

In Figure 3.28, the activation energies of  $\text{La}_{2-x}\text{Sr}_x\text{NiO}_4$  ( $x = 0, 0.4, 0.6, 0.8$  and  $1.0$ ) were calculated from linear part of Arrhenius plots in Table 3.15. Similar to  $\text{Pr}_{2-x}\text{Sr}_x\text{NiO}_4$  specimens, the activation energy decreased with increasing the amount of Sr.

When trivalent  $\text{Pr}^{3+}$  and  $\text{La}^{3+}$  cations are partially substituted with  $\text{Sr}^{2+}$  cation,  $\text{Ni}^{2+}$  change to  $\text{Ni}^{3+}$  to compensate charge neutrality and stabilize the structure. The more  $\text{Sr}^{2+}$  content, the higher electrical conductivity will be obtained.

**Table 3.15** Activation energy of  $\text{La}_{2-x}\text{Sr}_x\text{NiO}_4$  ( $x = 0, 0.4, 0.6, 0.8$  and  $1.0$ )

Composition	$E_a$ (kJ/mol)
$\text{La}_2\text{NiO}_4$	9.17
$\text{La}_{1.6}\text{Sr}_{0.4}\text{NiO}_4$	7.84
$\text{La}_{1.4}\text{Sr}_{0.6}\text{NiO}_4$	7.39
$\text{La}_{1.2}\text{Sr}_{0.8}\text{NiO}_4$	5.59
$\text{LaSrNiO}_4$	5.05

### 3.3.5.3 The Electrical Conductivity of $\text{Pr}_{2-x}\text{Sr}_x\text{CuO}_4$ ( $x = 0, 0.4, 0.6, 0.8$ and $1.0$ )

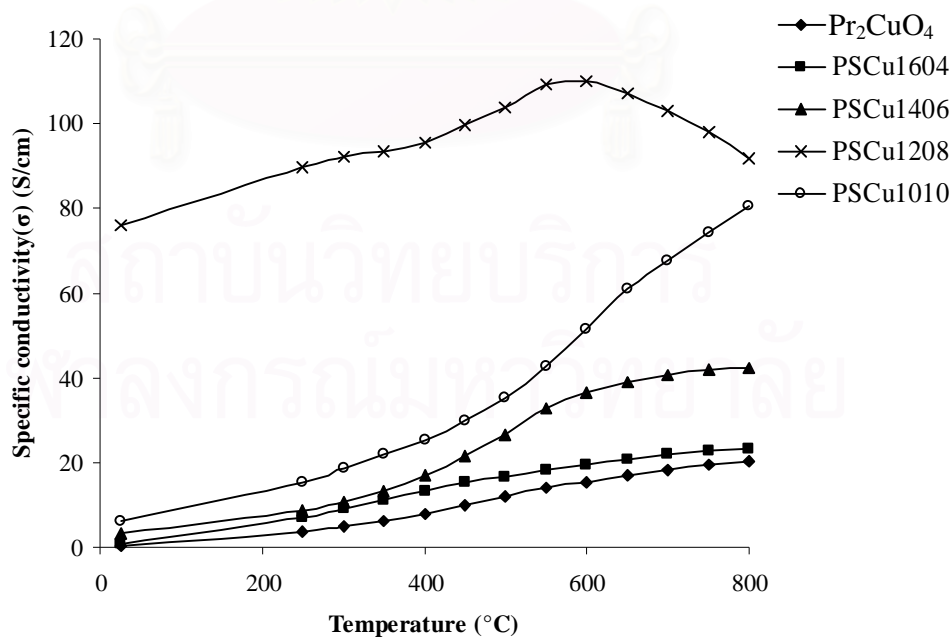


**Figure 3.29** Electrical conductivity ( $\sigma$ ) of  $\text{Pr}_{2-x}\text{Sr}_x\text{CuO}_4$  ( $x = 0, 0.4, 0.6, 0.8$  and  $1.0$ ) as a function of measuring temperature.

Figure 3.29 shows the electrical conductivity of the  $\text{Pr}_{2-x}\text{Sr}_x\text{CuO}_4$  ( $x = 0, 0.4, 0.6, \text{ and } 1.0$ ) as a function of measuring temperature. It is revealed that the conductivity of  $\text{Pr}_{2-x}\text{Sr}_x\text{CuO}_4$  ( $x = 0, 0.4, 0.6, 0.8$  and  $1.0$ ) increased with increasing temperature. These oxides behaved as semi-conductor. For  $\text{Pr}_{1.2}\text{Sr}_{0.8}\text{CuO}_4$  exhibited the semi-conductor type from room temperature to  $600\text{ }^\circ\text{C}$ . At high temperature the conductivity started to decrease. The optimum amount for Sr addition seems to be  $x = 0.8$  for maximizing electrical conductivity. The conductivity of  $\text{Pr}_{1.2}\text{Sr}_{0.8}\text{CuO}_4$  reached maximum value of  $110.2\text{ S/cm}$  at  $600\text{ }^\circ\text{C}$  which was about 5 times higher than that of undoped  $\text{Pr}_2\text{CuO}_4$  ( $20.3\text{ S/cm}$  at  $800\text{ }^\circ\text{C}$ ).

**Table 3.16** The specific conductivity of  $\text{Pr}_{2-x}\text{Sr}_x\text{CuO}_4$  ( $x = 0, 0.4, 0.6, 0.8$  and  $1.0$ )

Sample	Specific conductivity, $\sigma$ (S/cm)						
	300 °C	400 °C	500 °C	600 °C	700 °C	800 °C	$\sigma_{\text{max}}$ (T, °C)
$\text{Pr}_2\text{CuO}_4$	5.0	8.0	11.9	15.3	18.4	20.3	20.3 (800)
$\text{Pr}_{1.6}\text{Sr}_{0.4}\text{CuO}_4$	9.3	13.4	16.8	19.6	21.9	23.3	23.3 (800)
$\text{Pr}_{1.4}\text{Sr}_{0.6}\text{CuO}_4$	10.6	17.2	26.5	36.4	40.6	42.4	42.4 (800)
$\text{Pr}_{1.2}\text{Sr}_{0.8}\text{CuO}_4$	92.1	95.5	104.0	110.2	103.1	91.6	110.2 (600)
$\text{PrSrCuO}_4$	18.7	25.3	35.5	51.3	67.6	80.5	80.5 (800)

The plot of logarithm of the electrical conductivity as a function of inverse absolute temperature for  $\text{Pr}_{2-x}\text{Sr}_x\text{CuO}_4$  ( $x = 0, 0.4, 0.6, 0.8$  and  $1.0$ ) was shown in Figure 3.30.



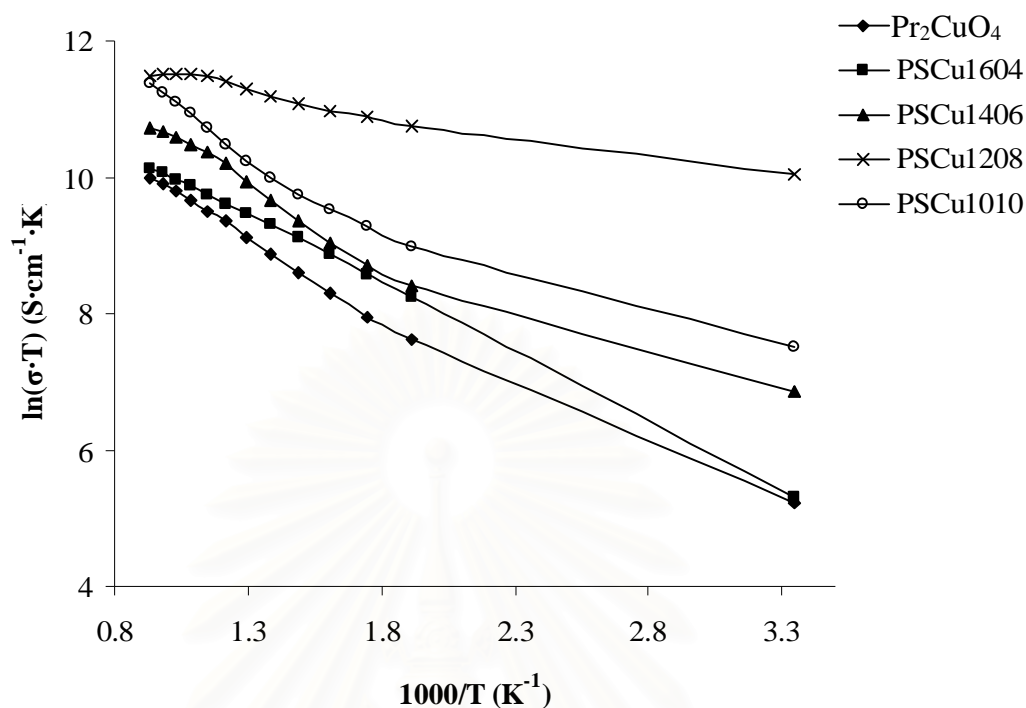


**Figure 3.30** Arrhenius plots of  $\text{Pr}_{2-x}\text{Sr}_x\text{CuO}_4$  ( $x = 0, 0.4, 0.6, 0.8$  and  $1.0$ )

The activation energy of specimens calculated from the linear part of Arrhenius plot were shown in Figure 3.30. The  $E_a$  values in air for all the specimens are listed in Table 3.17. The activation energy of  $\text{Pr}_{2-x}\text{Sr}_x\text{CuO}_4$  were higher than that of  $\text{Pr}_{2-x}\text{Sr}_x\text{NiO}_4$ .

**Table 3.17** Activation energy of  $\text{Pr}_{2-x}\text{Sr}_x\text{CuO}_4$  ( $x = 0, 0.4, 0.6, 0.8$  and  $1.0$ )

Composition	$E_a$ (kJ/mol)
$\text{Pr}_2\text{CuO}_4$	20.84
$\text{Pr}_{1.6}\text{Sr}_{0.4}\text{CuO}_4$	16.66
$\text{Pr}_{1.4}\text{Sr}_{0.6}\text{CuO}_4$	21.10
$\text{Pr}_{1.2}\text{Sr}_{0.8}\text{CuO}_4$	5.51
$\text{PrSrCuO}_4$	20.88

### 3.3.5.4 The Electrical Conductivity of $\text{La}_{2-x}\text{Sr}_x\text{CuO}_4$ ( $x = 0, 0.4, 0.6, 0.8$ and $1.0$ )

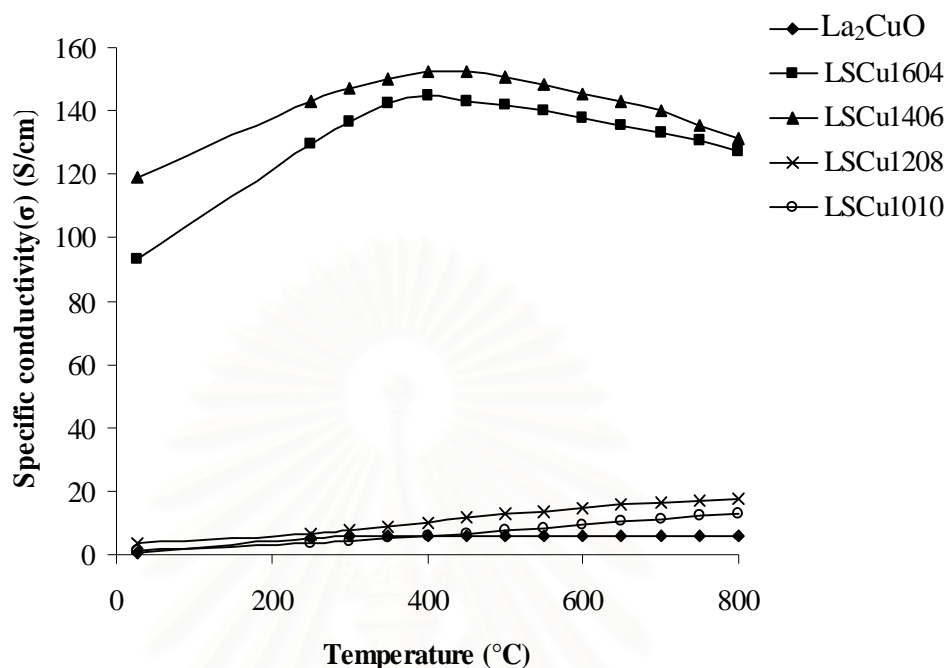


**Figure 3.31** Electrical conductivity ( $\sigma$ ) of  $\text{La}_{2-x}\text{Sr}_x\text{CuO}_4$  ( $x = 0, 0.4, 0.6, 0.8$  and  $1.0$ ) as a function of measuring temperature.

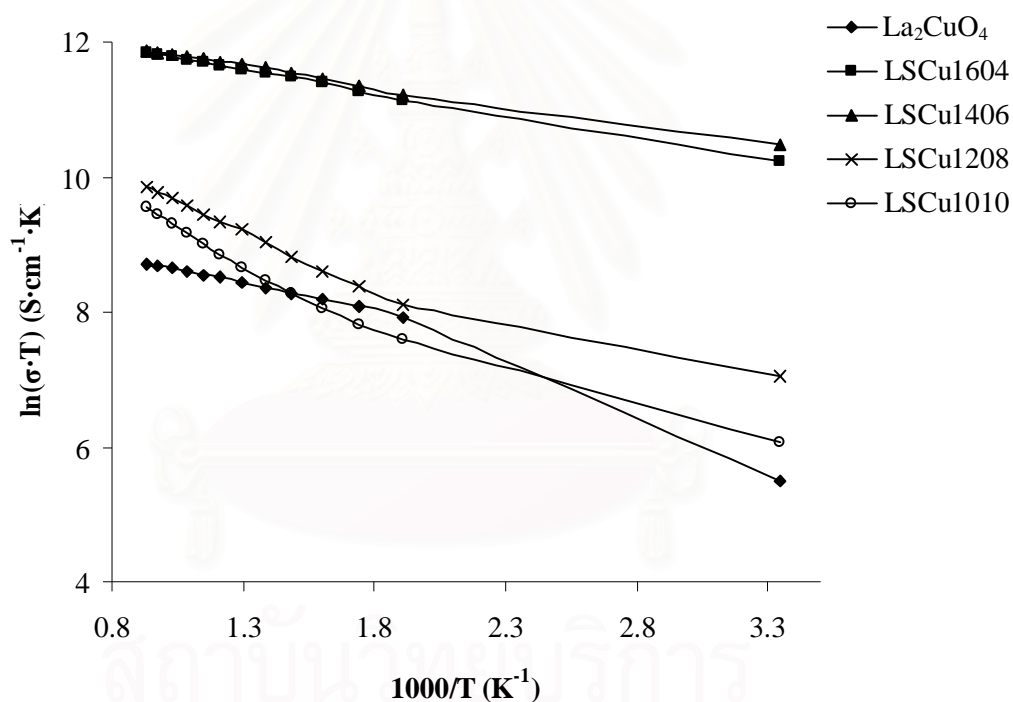
The temperature dependence of the electrical conductivity of  $\text{La}_{2-x}\text{Sr}_x\text{CuO}_4$  ( $x = 0.4, 0.6, 0.8$  and  $1.0$ ) compounds at temperature in range 25–800 °C was shown in Figure 3.31.

For  $\text{La}_{2-x}\text{Sr}_x\text{CuO}_4$  ( $x = 0, 0.8$  and  $1.0$ ), the increase of electrical conductivity was lower than those for comparable oxides  $\text{Pr}_{2-x}\text{Sr}_x\text{CuO}_4$  as temperature increased. Both  $\text{La}_{1.6}\text{Sr}_{0.4}\text{CuO}_4$  and  $\text{La}_{1.4}\text{Sr}_{0.6}\text{CuO}_4$  have similar conductivity properties. They show a maximum conductivity at lower temperature. The electrical conductivity result of  $\text{La}_{1.6}\text{Sr}_{0.4}\text{CuO}_4$  (144.5 S/cm) was closed to that of  $\text{La}_{1.4}\text{Sr}_{0.6}\text{CuO}_4$  (152.4 S/cm) at 400 °C which was about 25 times higher than that of undoped  $\text{La}_2\text{CuO}_4$  (6.0 S/cm at 550°C), as summarized in Table 3.18.

**Table 3.18** The specific conductivity of  $\text{La}_{2-x}\text{Sr}_x\text{CuO}_4$  ( $x = 0, 0.4, 0.6, 0.8$  and  $1.0$ )

Sample	Specific conductivity, $\sigma$ (S/cm)						$\sigma_{\text{max}}$ (T, °C)
	300 °C	400 °C	500 °C	600 °C	700 °C	800 °C	
$\text{La}_2\text{CuO}_4$	5.6	5.9	6.0	5.9	5.8	5.6	6.0 (550)
$\text{La}_{1.6}\text{Sr}_{0.4}\text{CuO}_4$	136.6	144.5	141.8	137.8	133.3	127.3	144.5 (400)
$\text{La}_{1.4}\text{Sr}_{0.6}\text{CuO}_4$	147.2	152.4	150.5	145.4	139.8	131.1	152.4 (400)
$\text{La}_{1.2}\text{Sr}_{0.8}\text{CuO}_4$	7.6	10.1	13.1	14.4	16.5	17.6	17.6 (800)
$\text{LaSrCuO}_4$	4.3	5.8	7.4	9.3	11.2	13.2	13.2 (800)

The Arrhenius plot of  $\text{La}_{2-x}\text{Sr}_x\text{CuO}_4$  oxides and the calculated activation energy of these oxides were shown in Figure 3.32 and Table 3.19.

**Figure 3.32** Arrhenius plots of  $\text{La}_{2-x}\text{Sr}_x\text{CuO}_4$  ( $x = 0, 0.4, 0.6, 0.8$  and  $1.0$ )

**Table 3.19** Activation energy of  $\text{La}_{2-x}\text{Sr}_x\text{CuO}_4$  ( $x = 0, 0.4, 0.6, 0.8$  and  $1.0$ )

Composition	$E_a$ (kJ/mol)
$\text{La}_2\text{CuO}_4$	6.71
$\text{La}_{1.6}\text{Sr}_{0.4}\text{CuO}_4$	5.58
$\text{La}_{1.4}\text{Sr}_{0.6}\text{CuO}_4$	4.89
$\text{La}_{1.2}\text{Sr}_{0.8}\text{CuO}_4$	14.98
$\text{LaSrCuO}_4$	17.00

From the conductivity investigation of  $\text{Ln}(\text{Pr}, \text{La})_2\text{MO}_4$  ( $M = \text{Ni}$  and  $\text{Cu}$ ), the results revealed that Sr-doped  $\text{Ln}(\text{Pr}, \text{La})_2\text{NiO}_4$  had a simple behavior with respect to the conductivity as a function of temperature. The conductivity in nickelates oxides clearly increase with increasing Sr content. Doping Sr at A-site of the cuprate oxides also affected the conductivity of  $\text{Ln}(\text{Pr}, \text{La})_2\text{CuO}_4$  but in a different manner. To achieve maximum electrical conductivity, Sr substitution in Pr-site of  $\text{Pr}_2\text{CuO}_4$  should be 0.8.

For  $\text{La}_{1.6}\text{Sr}_{0.4}\text{CuO}_4$  and  $\text{La}_{1.4}\text{Sr}_{0.6}\text{CuO}_4$  showed the high electrical conductivity at  $400\text{ }^\circ\text{C}$ . It is concluded that the conductivity of  $\text{Ln}(\text{Pr}, \text{La})_2\text{MO}_4$  can be enhanced greatly by doping Sr at A-site.

The conductivity of nickelates is much larger than the cuprates over one order of magnitude.  $\text{PrSrNiO}_4$  shows the highest conductivity at  $300\text{ }^\circ\text{C}$  ( $423.5\text{ S/cm}$ ) and is in the order of  $10^2\text{ S cm}^{-1}$  which is acceptable for the cathode materials of SOFCs.

สถาบันวิทยบริการ  
จุฬาลงกรณ์มหาวิทยาลัย

## CHAPTER IV

### CONCLUSIONS

The perovskite-like oxides in the system  $\text{Ln}(\text{Pr}, \text{La})_{2-x}\text{Sr}_x\text{MO}_4$  ( $\text{M} = \text{Co}, \text{Ni}, \text{Cu}$ ) ( $x = 0.4, 0.6, 0.8, 1$ ) were prepared by the modified citrate method and their structures as well as properties were also investigated.

From XRD results, the substitution of  $\text{Sr}^{2+}$  (larger radius) for  $\text{Pr}^{3+}$  or  $\text{La}^{3+}$  (smaller radius), caused in the transformation of structure from orthorhombic to tetragonal. The trace amount of impurity phase was presented in  $\text{La}_2\text{CoO}_4$ ,  $\text{Pr}_2\text{NiO}_4$ ,  $\text{La}_2\text{CuO}_4$  and  $\text{La}_{1.6}\text{Sr}_{0.4}\text{CuO}_4$ . All of the perovskite oxide can be prepared except the synthesized  $\text{Pr}_{2-x}\text{Sr}_x\text{CoO}_4$  and  $\text{La}_{2-x}\text{Sr}_x\text{CoO}_4$  series had physical instability after sintering. IR results confirmed the structure analysis by XRD. All sample had the vibrational absorption band at around  $520\text{--}500\text{ cm}^{-1}$ , which is the characteristic band of compounds with  $\text{K}_2\text{NiF}_4$  structure. In addition, absorption band at  $680\text{ cm}^{-1}$ , indicated that it was in orthorhombic structure that confirmed the transformation of structure from orthorhombic to tetragonal.

The morphologies of the perovskite discs were characterized by SEM. The Sr content affected on the grain size of the  $\text{Ln}(\text{Pr}, \text{La})_{2-x}\text{Sr}_x\text{MO}_4$ . Doping with strontium decreases melting points of the materials, resulting in a liquid phase-assisted sintering and an enhanced grain growth according to the density. Moreover, Cu can affect the decreasing of the melting point of  $\text{Ln}(\text{Pr}, \text{La})_{2-x}\text{Sr}_x\text{CuO}_4$ , so the fusion of grain of cuprates more easily occurred than that of nickelates.

Experimental results of  $\text{O}_2$ -TPD revealed that  $\text{PrSrNiO}_4$  showed the highest oxygen desorption ( $0.6508\text{ mmol/g}$ ). The electrical conductivity can be improved by addition Sr at A-site. The conductivities of the nickelate were higher than that of cuprate.  $\text{PrSrNiO}_4$  showed the highest electrical conductivity ( $423.5\text{ S/cm}$  at  $300^\circ\text{C}$ ) which was about 4 times higher than that of undoped  $\text{Pr}_2\text{NiO}_4$  ( $107.4\text{ S/cm}$  at  $400^\circ\text{C}$ ) and  $\text{LaSrNiO}_4$  showed the electrical conductivity of  $361.6\text{ S/cm}$  at  $400^\circ\text{C}$  which was about 4.5 times higher than that of  $\text{La}_2\text{NiO}_4$  ( $80.1\text{ S/cm}$  at  $400^\circ\text{C}$ ).

In conclusion, Sr-doped  $\text{Ln}_2(\text{Pr}, \text{La})\text{NiO}_4$  exhibited a higher potential to be used as cathode for SOFC.

### Suggestions

From experiment results, future work should be focused on the following:

1. To test thermal expansion coefficient (TEC) of prepared perovskites for fuel cell application.
2. To focus on the study of the performance of Sr-doped  $\text{Ln}_2(\text{Pr, La})\text{NiO}_4$  specimens used as cathode for SOFC.



สถาบันวิทยบริการ  
จุฬาลงกรณ์มหาวิทยาลัย

## REFERENCES

- [1] Viswanathan, B. Solid Oxide Fuel Cells [Online]. 2007. Available from: [http://www.che.iitm.ac.in/~arunkt/fuelcells/talkfiles/bv\\_sofc.pdf](http://www.che.iitm.ac.in/~arunkt/fuelcells/talkfiles/bv_sofc.pdf) [2008, January 6].
- [2] Eileen, J. Solid Oxide Fuel Cells [Online]. 2003. Available from: <http://www.csa.com/discoveryguides/fuecel/overview.php> [2008, February 21].
- [3] Netscape Navigator Gold. Fuel Cell Background Information [Online]. (n.d.). Available from: <http://www.gmi.edu/~altfuel/fcbac.htm> [2008, February 21].
- [4] Weissbart, J.; and Ruka, R. A Solid Electrolyte Fuel Cell. *Journal of the Electrochemical Society* 109 (1962): 723–726.
- [5] Park, S.; John, M. V.; and Raymond, J. G. Direct Oxidation of Hydrocarbons in a Solid-Oxide Fuel Cell. *Nature* 404 (2000): 265–267.
- [6] Singhal, S. C. Science and Technology of Solid–Oxide Fuel Cells. *Materials Research Society Bulletin* 25 (2000): 6–21.
- [7] Liou, J. H.; Liou, P. J.; and Sheu, T. S. Physical Properties and Crystal Chemistry of Bismuth Oxide Solid Solution. *Ceramic Transactions* 109 (1999): 3–10.
- [8] Chou, Y. S.; and Armstrong, T. R. Lattice Expansion Induced Stresses in Calcium–doped Yttrium Chromite Interconnect Materials under Reducing Environment. *Ceramic Transactions* 109 (1999): 95–104.
- [9] Matsuzaki, Y.; and Yasuda, I. Dependence of SOFC Cathode
- [10] Degradation by Chromium–containing Alloy on Compositions of Electrodes. *Journal of the Electrochemical Society (USA)* 148 (2001): A126–A131.
- [11] Ralph, J. M.; Kilner, J. A.; and Steele, B. C. H. Improving Gd–doped Ceria Electrolytes for Low Temperature Solid Oxide Fuel Cells. *New Materials for Batteries and Fuel Cells* (1999): 309–314.
- [12] De Souza, R. A.; and Kilner, J. A. Oxygen transport in  $\text{La}_{1-x}\text{Sr}_x\text{Mn}_{1-y}\text{Co}_y\text{O}_{3\pm\delta}$  perovskites Part I. Oxygen tracer diffusion. *Solid State Ionics* 106 (1998): 175–187.

- [13] Akin, F. T.; and Lin, J. Y. S. Oxygen permeation through oxygen ionic or mixed-conducting ceramic membranes with chemical reactions. *Journal of Membrane Science* 231 (2004): 133–146.
- [14] Dyer, P. N.; Richards, R. E.; Russek, S. L.; and Taylor, D. M. Ion transport membrane technology for oxygen separation and syngas production. *Solid State Ionics* 134 (2000): 21–33.
- [15] Kharton, V.V.; Yaremchenko, A. A.; Tsipis, E. V.; Valente, A. A.; Patrakeevev, M. V.; Shaula, A. L.; Frade, J. R.; and Rocha J. Characterization of mixed-conducting  $\text{La}_2\text{Ni}_{0.9}\text{Co}_{0.1}\text{O}_{4+\delta}$  membranes for dry methane oxidation. *Applied Catalysis A: General* 261 (2004): 25–35.
- [16] Al Daroukh, M.; Vashook, V. V.; Ullmann, H.; Raj, I. A.; and Tietz F. Oxides of the  $\text{AMO}_3$  and  $\text{A}_2\text{MO}_4$ -type: structural stability, electrical conductivity and thermal expansion. *Solid State Ionics* 158 (2003): 141–150.
- [17] Kharton, V. V.; Yaremchenko, A. A.; Shaula, A. L.; Patrakeevev, M. V.; Naumovich, E. N.; Logvinovich, D. I.; Frade, J. R.; and Marques F. M. B. Transport properties and stability of Ni-containing mixed conductors with perovskite- and  $\text{K}_2\text{NiF}_4$ -type structure. *Journal of Solid State Chemistry* 177 (2004): 26–37.
- [18] Kilner, J. A.; and Shaw, C. K. M. Mass transport in  $\text{La}_2\text{Ni}_{1-x}\text{Co}_x\text{O}_{4+\delta}$  oxides with the  $\text{K}_2\text{NiF}_4$  structure. *Solid State Ionics* 154–155 (2002): 523–527.
- [19] Kharton, V. V.; Tsipis, E. V.; Yaremchenko, A. A.; and Frade, J. R. Surface-limited oxygen transport and electrode properties of  $\text{La}_2\text{Ni}_{0.8}\text{Cu}_{0.2}\text{O}_{4+\delta}$ . *Solid State Ionics* 166 (2004): 327–337.
- [20] Bochkov, D. M.; Kharton, V. V.; Kovalevsky, A. V.; Viskup, A. P.; and Naumovich, E. N. Oxygen permeability of  $\text{La}_2\text{Cu}(\text{Co})\text{O}_{4+\delta}$  solid solutions. *Solid State Ionics* 120 (1999): 281–288.
- [21] Kharton, V. V.; Alexandre, P. V.; Naumovich, E. N.; and Marques F. M. B. Ionic transport in oxygen-hyperstoichiometric phases with  $\text{K}_2\text{NiF}_4$ -type structure. *Solid State Ionics* 143 (2001): 337–353.
- [22] Naumovich, E. N.; Patrakeevev, M. V.; Kharton, V. V.; Yaremchenko, A. A.; Logvinovich, D. I. ; and Marques F. M. B. Oxygen nonstoichiometry



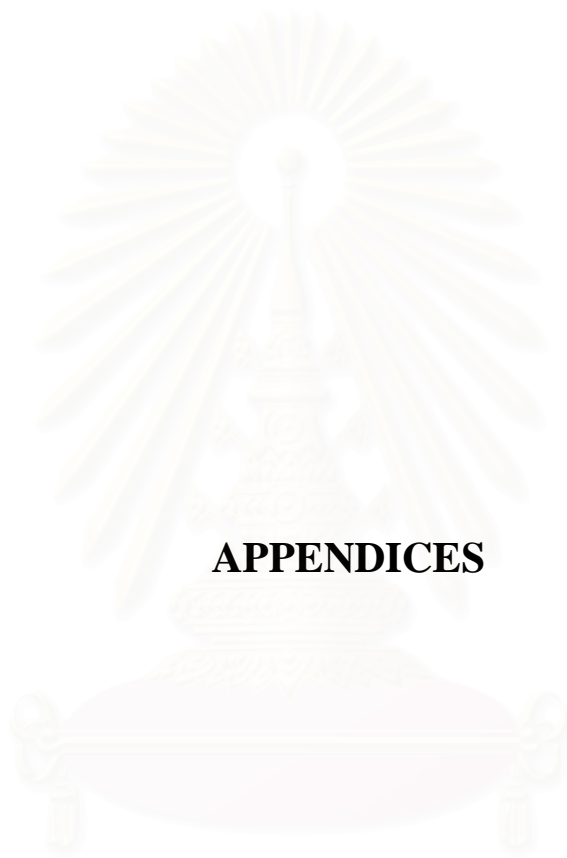
- in  $\text{La}_2\text{Ni}(\text{M})\text{O}_{4+\delta}$  (M = Cu, Co) under oxidizing conditions. *Solid State Sciences* 7 (2005): 1353–1362.
- [23] Davidson, M. W. The Perovskite Collection [Online]. 2004. Available from: <http://micro.magnet.fsu.edu/micro/gallery/perovskite/perovskite.html> [2008, March 10].
- [24] Ramanujachary, K. V.; Sunstrom, J. E.; Fawcett, I.; Shuk, P.; Greenblatt, M.; Croft, M.; Nowik, I.; Herber, R. H.; and Khalid S. Magnetic and Electrical Properties of  $\text{Eu}_2\text{VO}_4$ . *Materials Research Bulletin* 34 (1999): 803–816.
- [25] Zhu, J.; Zhao, Z.; Xiao, D.; Li, J.; Yang, X.; and Wu, Y. Characterization and catalytic activity in NO decomposition of  $\text{La}_{2-x}\text{Sr}_x\text{CuO}_4$  ( $0 \leq x \leq 1$ ) compounds with  $T^*$  phase structure. *Materials Chemistry and Physics* 94 (2005): 257–260.
- [26] Ganguly, P.; and Rao, C. N. R. Crystal chemistry and magnetic properties of layered metal oxides possessing the  $\text{K}_2\text{NiF}_4$  or related structures. *Journal of Solid State Chemistry* 53 (1984): 193–216.
- [27] Patel, R.; Simon, C.; and Weller, M. T.  $\text{LnSrScO}_4$  (Ln = La, Ce, Pr, Nd and Sm) systems and structure correlations for  $\text{A}_2\text{BO}_4$  ( $\text{K}_2\text{NiF}_4$ ) structure types. *Journal of Solid State Chemistry* 180 (2007): 349–359.
- [28] Peña, M. A.; and Fierro, J. L. G. Chemical Structures and Performance of Perovskite Oxides. *Chemical Reviews* 101 (2001): 1981–2017.
- [29] Gschneider, K. A. Jr.; and Eyring, L. Handbook of the Physics and Chemistry of Rare Earths, Amsterdam, p553. North-Holland Publishers, 1979.
- [30] Rao, C. N. R.; Gopalakrishnan, J.; and Vidyasagar, K. Superstructure, ordered defects and nonstoichiometry in metal oxides of perovskite and related structure. *Indian Journal of Chemistry* 23A (1984): 265–284.
- [31] Teraoka, Y.; Nobunaga, T.; and Yamazoe, N. Effect of cation substitution on the oxygen semipermeability of perovskite-type oxide. *Chemistry Letters* (1988): 503–506.
- [32] Goodenough, J. B.; and Longo J. M. Crystallographic and Magnetic Properties of Perovskite and Perovskite-related Compounds, Landholt-Bornstein Numerical Data and Functional Relationships in

Science and Technology Berlin–Heidelberg, New Series Group III/vol. 4a, Springer-Verlag, 1970.

- [33] Alcock, C. B.; Carberry, J. J.; Doshi, R.; and Gunasekaran, N. Methane Coupling Reaction on Oxide Solid Solution Catalysts. *Journal of Catalysis* 143 (1993): 533–538.
- [34] Teraoka, Y.; Zhang, H.-M.; and Yamazoe, N. Oxygen sorption and catalytic properties of  $\text{La}_{1-x}\text{Sr}_x\text{Co}_{1-y}\text{Fe}_y\text{O}_3$  Perovskite-type oxides. *Journal of Catalysis* 121 (1990): 432–440.
- [35] Yamazoe, N.; Teraoka, Y.; and Seiyama, T. TPD and XPS Study on Thermal Behavior of Adsorbed Oxygen in  $\text{La}_{1-x}\text{Sr}_x\text{CoO}_3$ . *Chemistry Letters* (1981): 1767.
- [36] Zhu, J.; Zhao, Z.; Xiao, D.; Li, J.; Yangand, X.; and Wu, Y. Study of  $\text{La}_{2-x}\text{Sr}_x\text{CuO}_4$  ( $x = 0.0, 0.5, 1.0$ ) catalysts for NO+CO reaction from the measurements of  $\text{O}_2$ -TPD,  $\text{H}_2$ -TPR and cyclic voltammetry. *Journal of Molecular Catalysis A: Chemical* 238 (2005): 35–40.
- [37] Cui, X.; and Liu, Y. New methods to prepare ultrafine particles of some perovskite-type oxides. *Chemical Engineering Journal* 78 (2000): 205–209.
- [38] Zeng, Y.; and Lin, Y. S. A Transient TGA Study on Oxygen Permeation Properties of Perovskite-Type Ceramic Membrane. *Solid State Ionics* 110 (1998): 209–221.
- [39] Richerson, D. W. Modern Ceramic Engineering, Properties, Processing, and Use in Design, pp.378–381, 1992.
- [40] Al Daroukh, M.; Vashook, V. V.; Ullmann, H.; Tietz, F.; and Raj, I. A. Oxides of the  $\text{AMO}_3$  and  $\text{A}_2\text{MO}_4$ -type: structural stability, electrical conductivity and thermal expansion. *Solid State Ionics* 158 (2003): 141–150.
- [41] Riza, F.; and Ftikos, Ch. Influence of A- and B-site doping on the properties of the system  $\text{La}_2\text{CoO}_{4\pm\delta}$ . *Journal of the European Ceramic Society* 27 (2007): 571–573.
- [42] Munnings, C. N.; Skinner, S. J.; Amow, G.; Whitfield, P. S.; and Davidson I. J. Structure, stability and electrical properties of the  $\text{La}_{(2-x)}\text{Sr}_x\text{MnO}_{4\pm\delta}$  solid solution series. *Solid State Ionics* 177 (2006): 1849–1853.

- [43] Yu, H.-C.; and Fung K.-Z. Role of strontium addition on the phase transition of lanthanum copper oxide from  $K_2NiF_4$  to perovskite structure. *Journal of Alloys and Compounds* 440 (2007): 62–68.
- [44] Yang, X.; Luo, L.; and Zhong, H. Structure of  $La_{2-x}Sr_xCoO_{4+\lambda}$  ( $x = 0.0-1.0$ ) and their catalytic properties in the oxidation of CO and  $C_3H_8$ . *Applied Catalysis A: General* 272 (2004): 299–303.
- [45] Jennings, A. J.; and Skinner, S. J. Thermal stability and conduction properties of the  $La_xSr_{2-x}FeO_{4+\delta}$  system. *Solid State Ionics* 152–153 (2002): 663–667.
- [46] Vashook, V.; Zosel, J.; Wen, T.-L.; and Guth, U. Transport properties of the  $Pr_{2-x}Sr_xNiO_{4\pm\delta}$  ceramics with  $x = 0.3$  and  $0.6$ . *Solid State Ionics* 177 (2006): 1827–1830.
- [47] Wang, Y.; Nie, H.-W.; Wang, S.; Wen, T.-L.; Guth, U.; and Vashook, V.  $A_{2-\alpha}A'_\alpha BO_4$ -type oxides as cathode materials for IT-SOFCs ( $A = Pr, Sm; A' = Sr; B = Fe, Co$ ). *Materials Letters* 60 (2006): 1174–1178.
- [48] Nie, H. W.; Wen, T.-L.; Wang, S. R.; Wang, Y. S.; Guth, U.; and Vashook, V. Preparation, thermal expansion, chemical compatibility, electrical conductivity and polarization of  $A_{2-\alpha}A'_\alpha MO_4$  ( $A = Pr, Sm; A' = Sr; M = Mn, Ni; \alpha = 0.3, 0.6$ ) as a new cathode for SOFC. *Solid State Ionics* 177 (2006): 1929–1932.
- [49] Mulders, J. J. L. An in-situ four-point probe method for the electrical characterization of beam induced depositions [Online]. (n.d.). Available from: [http://www.nanotechnik.com/fileadmin/public/publications/in-situ\\_four-point-probe.pdf](http://www.nanotechnik.com/fileadmin/public/publications/in-situ_four-point-probe.pdf) [2008, January 24].
- [50] Weller, M. T. Inorganic Materials Chemistry, New York, p38. Oxford University Press Inc, 1994.
- [51] Zhu, J.; Zhao, Z.; Xiao, D.; Li, J.; Yang, X.; and Wu Y. Characterization and catalytic activity in NO decomposition of  $La_{2-x}Sr_xCuO_4$  ( $0 \leq x \leq 1$ ) compounds with  $T^*$  phase structure. *Materials Chemistry and Physics* 94 (2005): 257–260.
- [52] Wen, T.-L.; Tu, H.; Xu, Z.; and Yamamoto, O. A study of  $(Pr, Nd, Sm)_{1-x}Sr_xMnO_3$  cathode materials for solid oxide fuel cell. *Solid State Ionics* 121 (1999): 25–30.

- [53] Lavat, A. E.; and Baran, E. J. IR-spectroscopic behaviour of  $AA'BO_4$  oxides belonging to the  $K_2NiF_4$  structural type. *Journal of Alloys and Compounds* 368 (2004): 130–134.
- [54] Liu, J.; Zhao, Z.; Xu, C.-M.; and Duan, A.-J. Simultaneous removal of  $NO_x$  and diesel soot over nanometer  $Ln-Na-Cu-O$  perovskite-like complex oxide catalysts. *Applied Catalysis B: Environmental* 78 (2008): 61–72.
- [55] Fino, D.; Russo, N.; Saracco, G.; and Specchia V. The role of suprafacial oxygen in some perovskites for the catalytic combustion of soot. *Journal of Catalysis* 217 (2003): 367–375.
- [56] Lee, M.-D.; Chen, Z.-B.; and Ling, T.-R. Catalytic behavior and electrical conductivity of  $LaNiO_3$  in ethanol oxidation. *Applied Catalysis A: General* 136 (1996): 191–203.
- [57] Wu, Y.; Zhao, Z.; and Yang, X. Comparative study of Nickel-based perovskite-like mixed oxide catalysts for direct decomposition of  $NO$ . *Applied Catalysis B: Environmental* 8 (1996): 281–297.
- [58] Millburn, J. E.; Green, M. A.; Neumann, D. A.; and Rosseinsky M. J. Evolution of the Structure of the  $K_2NiF_4$  Phases  $La_{2-x}Sr_x NiO_{4+\delta}$  with Oxidation State: Octahedral Distortion and Phase Separation ( $0.2 \leq x \leq 1.0$ ). *Journal of Solid State Chemistry* 145 (1999): 401–420.
- [59] Vidal, K.; Rodríguez-Martínez, L. M.; Ortega-San-Martín, L.; Díez-Linaza, E.; Nó, M. L.; Rojo, T.; Laresgoiti, A.; and Arriortua M. I. Isolating the effect of doping in the structure and conductivity of  $(Ln_{1-x}M_x)FeO_{3-\delta}$  perovskites. *Solid State Ionics* 178 (2007): 1310–1316.
- [60] Karita, R.; Kusaba, H.; Sasaki, K.; and Teraoka Y. Superiority of nitrate decomposition method for synthesis of  $K_2NiF_4$ -type  $La_xSr_{2-x}MnO_4$  catalysts. *Catalysis Today* 126 (2007): 471–475.
- [61] Atomistic Simulation Group. Database of Ionic Radii [online]. (n.d.). Available from: <http://abulafia.mt.ic.ac.uk/shannon/ptable.php> [2008, February 16].



**APPENDICES**

สถาบันวิทยบริการ  
จุฬาลงกรณ์มหาวิทยาลัย

## APPENDICES

### APPENDICE A

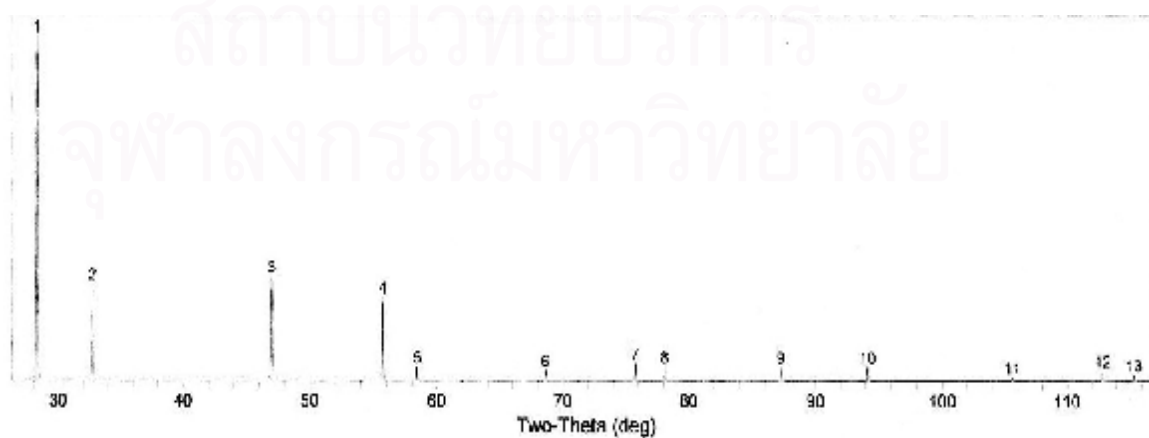
#### XRD data

#### Praseodymium Oxide, Pr<sub>6</sub>O<sub>11</sub>

PDF#42-1121

Cubic-powder diffraction

	2-Theta	d (Å)	h k l
<b>Pr<sub>6</sub>O<sub>11</sub></b>	28.249	3.1565	1 1 1
	32.739	2.7331	2 0 0
	46.993	1.9320	2 2 0
	55.706	1.6487	3 1 1
	58.424	1.5783	2 2 2
	68.588	1.3671	4 0 0
	75.732	1.2549	3 3 1
	78.082	1.2229	4 2 0
	87.265	1.1163	4 2 2
	94.120	1.0522	5 1 1
	105.623	0.9669	4 4 0
	112.892	0.9243	5 3 1
	115.418	0.9112	6 0 0

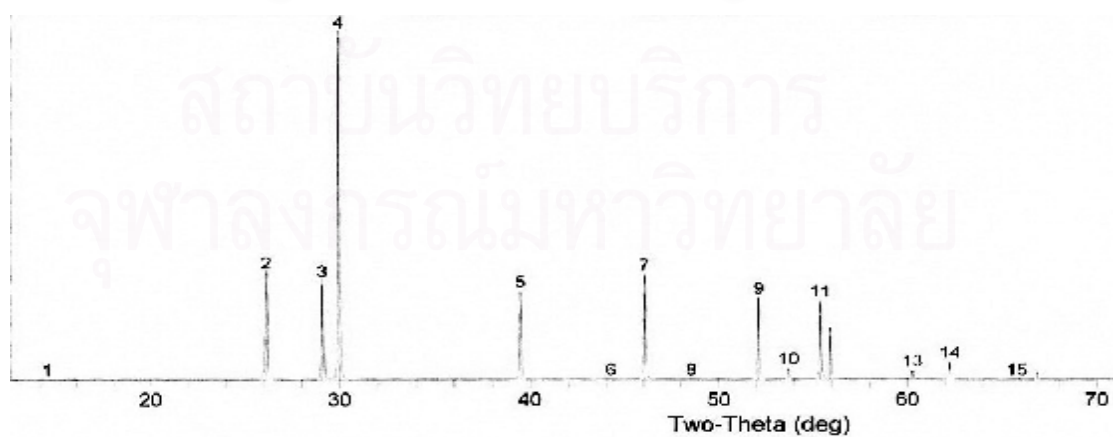


**Lanthanum Oxide, La<sub>2</sub>O<sub>3</sub>**

PDF#83-1344

Hexagonal-powder diffraction

	<b>2-Theta</b>	<b>d (Å)</b>	<b>h k l</b>
<b>La<sub>2</sub>O<sub>3</sub></b>	14.423	6.1361	0 0 1
	26.106	3.4105	1 0 0
	29.081	3.0680	0 0 2
	29.950	2.9810	0 1 1
	39.474	2.2809	0 1 2
	44.246	2.0454	0 0 3
	46.058	1.9691	1 1 0
	48.516	1.8749	1 1 1
	52.097	1.7541	1 0 3
	53.707	1.7053	2 0 0
	55.399	1.6571	1 1 2
	55.917	1.6430	2 0 1
	60.282	1.5340	0 0 4
	62.235	1.4905	2 0 2
	65.777	1.4185	1 1 3
	66.814	1.3990	0 1 4



## APPENDICE B

### Tolerance Number

Goldschmidt (1926) defined the tolerance limits of the size of ions through a tolerance factor,  $t$  as Equation (A.1)

$$t = \frac{(r_A + r_O)}{\sqrt{2}(r_B + r_O)} \quad (\text{B.1})$$

where  $r_A$ ,  $r_B$ , and  $r_O$  are the radii of respective ions. Tolerance factors of  $\text{Ln}(\text{Pr}, \text{La})_{2-x}\text{Sr}_x\text{MO}_4$  were calculated by using Shannon's ionic radii [60]. Apparent  $t$  values were calculated based on the following chemical formulae without the formation of oxide ion vacancy and equations for the calculation of average ionic radius were shown in Table B-1 [61].

Therefore, as Equation B.1 the tolerance number of perovskite compounds such as  $\text{Pr}_{1.6}\text{Sr}_{0.4}\text{NiO}_4$  was calculated as below.

$$\text{Tolerance number of } \text{Pr}_{1.6}\text{Sr}_{0.4}\text{NiO}_4 = \frac{(((1.319 \times 1.6) + (1.45 \times 0.4)) / 2) + 1.26}{\sqrt{2}(0.83 + 1.26)} = 0.8814$$

**Table B-1** Ionic charge, coordination number and ionic radius of concerned metals.

Element	Ionic charge	Coordination No.	Ionic radius(Å)
Pr	3+	9	1.319
La	3+	9	1.356
Sr	2+	9	1.45
Co	2+	6	0.89
Co	3+	6	0.75
Co	4+	6	0.67
Ni	2+	6	0.83
Ni	3+	6	0.7
Ni	4+	6	0.62
Cu	1+	6	0.91
Cu	2+	6	0.87
Cu	3+	6	0.68
O	2-	6	1.26



## APPENDICE C

### Activation Energy ( $E_a$ )

Arrhenius plot of  $\text{Pr}_{1.6}\text{Sr}_{0.4}\text{NiO}_4$  is given in Figure C–1. The linear part can be described by the small polaron conduction mechanism, following the formula:

$$\sigma = (A/T) \exp(-E_a/kT) \quad (\text{C.1})$$

Therefore, 
$$\sigma T = A \exp(-E_a/kT) \quad (\text{C.2})$$

$$\ln \sigma T = -E_a/kT + \ln A \quad (\text{C.3})$$

$A$  is material constant including the carrier concentration term,

$E_a$  is the activation energy

$k$  is the Boltzmann's constant

$T$  is the absolute temperature.

From Equation C.3, Arrhenius plot of  $\ln \sigma T$  versus  $1000/T$  gives a straight line, whose slope and intercept can be used to determine  $E_a$  and  $A$  respectively.

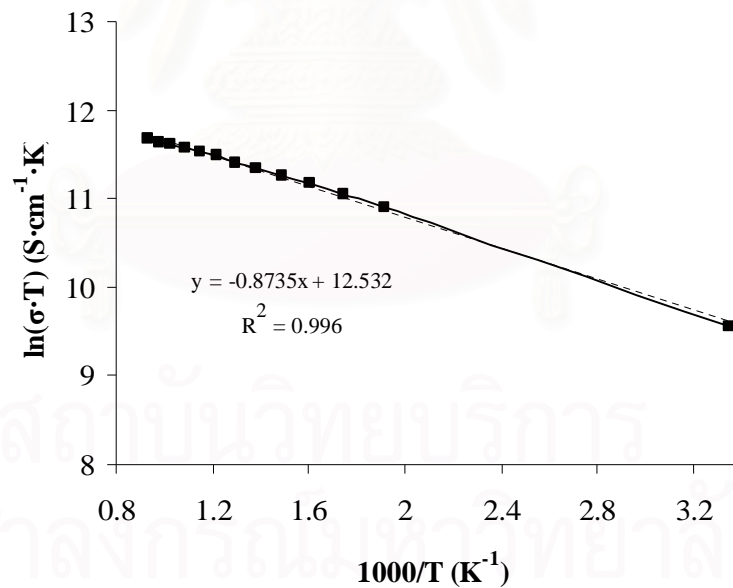


**Figure C–1** Arrhenius plot of the electrical conductivity of  $\text{Pr}_{1.6}\text{Sr}_{0.4}\text{NiO}_4$ .

The activation energy calculated from the slope of the straight line of figure B.1 For example, the activation energy ( $E_a$ ) of  $\text{Pr}_2\text{Ni}_{10.7}\text{Cu}_{0.3}\text{O}_4$ , was calculated as:

$$\text{Slope} = -E_a/k$$

$$\text{Slope} = -E_a/8.314472$$

$$E_a = -\text{slope} \times 8.314472$$

$$E_a = -(-0.8735) \times 8.314472$$

$$E_a = 7.26 \text{ kJ/mol}$$



สถาบันวิทยบริการ  
จุฬาลงกรณ์มหาวิทยาลัย

## VITAE

Miss Nuengruetai Supanwanich was born on October 1, 1983 in Bangkok, Thailand. She graduated with Bachelor's Degree in Chemistry from Faculty of Science, Mahidol University in 2005. She continued her study in Petrochemistry and Polymer Science Program, Faculty of Science, Chulalongkorn University in 2005 and completed in 2008.

Her present address in 130/73 Rewadee Rd., Taladkwan, Muang, Nonthaburi, Thailand 11000, Tel. 0814381528.



สถาบันวิทยบริการ  
จุฬาลงกรณ์มหาวิทยาลัย